Studies on the critical current density in several pure and hybrid cuprate superconductors

Thesis Submitted for the Degree of
Doctor of Philosophy (Science) in Physics

of

Jadavpur University

by

Probhu Mandal

Under the supervision of

Prof. Ajay Kumar Ghosh

Department of Physics
Jadavpur University
Kolkata 700032, India, 2024

যাদবপুর বিশ্ববিদ্যালয়
কলকাতা-৭০০০৩২, ভারত

* JADAVPUR UNIVERSITY
KOLKATA-700 032, INDIA

FACULTY OF SCIENCE: DEPARTMENT OF PHYSICS

Certificate from the Supervisor

This is to certify that the thesis entitled "**Studies on the critical current density in several pure and hybrid cuprate superconductors**" submitted by Mr. **Probhu Mandal** who got his name registered on **13.11.2019** for the award of Ph.D. (Science) degree of Jadavpur University, is absolutely based upon his own work under the supervision of **Prof. Ajay Kumar Ghosh** and that neither this thesis nor any part of it has been submitted for either any degree/diploma or any other academic award anywhere before.

Professor (Dr.) Ajay Kumar Ghosh
Department of Physics
Jadavpur University
Kolkata - 700032

Ajay Kumar Ghosh
(Prof. Ajay Kumar Ghosh)
16.08.2024
Signature of Supervisor
with Date and Official Seal

*Established on and from 24th December, 1955 vide Notification No. 10986-Edn/IU-42/55 dated 6th December, 1955 under Jadavpur University Act, 1955
(West Bengal Act XXXIII of 1955) followed by Jadavpur University Act, 1981 (West Bengal Act XXIV of 1981)

ফোন: ০৩৩-২৪১৪-৬৬৬৬ Ext. ২৭৬১ Website: www.jadavpuruniversity.in
মো: +৯১-৯৮৩০৮৪৮৯২০

Phone: 033-2414-6666 Ext. 2761
M: +91-9830848920
Email: ajayk.ghosh@jadavpuruniversity.in

Acknowledgments

First of all, I would like to express my sincere gratitude and respectful regards to my supervisor Prof. Ajay Kumar Ghosh, Department of Physics, Jadavpur University, who gave me the golden opportunity to study the topic "Studies on the critical current density in several pure and hybrid cuprate superconductors". His constant support and encouragement were invaluable throughout my research and thesis writing process. I am truly grateful for his guidance.

I sincerely admire the contributions of all my lab mates of AKGPHY Group: Dr. S. Mollah, Dr. I. Mukherjee, Dr. B. Biswas, Dr. S. Halder, Dr. S. Roy, Dr. P. Das, Dr. T. Sk, D. Rakshit, I. Mukherjee, R. K. Saha and F. Molla for their excellent cooperation during experiments in the laboratory and for all the fun we have had in the last few years.

I would like to give special thanks to my parents and brothers, family members and friends for encouraging me in all of my pursuits, inspiring me to follow my dreams and for their enormous support and motivation in every situation of my life.

I am also thankful to the University Grants Commission, Govt. of India for awarding me the UGC-NET-JRF fellowship (Beneficiary Code/Flag: BININ01386700 A).

List of Publications and Presentations

Journals

1. **P. Mandal**, D. Rakshit, T. Sk, Ajay Kumar Ghosh, Microparticle-controlled superfluid density and critical current density in $YBa_2Cu_3O_{7-\delta}$, J. Supercond. Nov. Magn. **35** (2022) 1079.

2. **P. Mandal**, D. Rakshit, I. Mukherjee, T. Sk, Ajay Kumar Ghosh, Critical current density in granular $REBa_2Cu_3O_{7-\delta}$ superconductors with different interlayer magnetic coupling, Phys. Lett. A **436** (2022) 128072.

3. **P. Mandal**, D. Rakshit, T. Sk, Ajay Kumar Ghosh, Insulating nanoparticle induced pinning in YBCO superconductor: crossover from collective to strong pinning regimes, Appl. Phys. A **129** (2023) 650.

4. **P. Mandal**, Ajay Kumar Ghosh, Criteria sensitive analysis of transport critical current density in BZO mixed YBCO, Mod. Phys. Lett. B **38** (2024) 2450050.

5. **P. Mandal**, Ajay Kumar Ghosh, Transport critical current density in composite system of $NdBa_2Cu_3O_{7-\delta}$ and Sn nanoparticles, 2024 (Submitted).

6. **P. Mandal**, S. Mollah, D. Rakshit, I. Mukherjee, T. Sk., Ajay Kumar Ghosh, Vortex pinning, equilibrium magnetization and pairing symmetry in BPBO superconductor, 2024 (Submitted).

7. **P. Mandal**, Ajay Kumar Ghosh, An increasing transport critical current density and a peak in superfluid density with lowering in temperature, 2024 (Submitted).

8. T. Sk, **P. Mandal**, D. Rakshit, Ajay Kumar Ghosh, Drastic enhancement of magnetic critical current density in Zn doped Bi-2212, Physica C **603** (2022) 1354152.

9. T. Sk, **P. Mandal**, S. Haldar, Ajay Kumar Ghosh, Effectiveness of two pinning profiles in controlling magnetic critical current density in YBCO + YCMO composites, J. Supercond. Nov. Magn. **36** (2023) 863.

10. D. Rakshit, **P. Mandal**, T. Sk, Ajay Kumar Ghosh, Variation of junction resistance near phase transition of $NdBa_2Cu_3O_{7-\delta}$ superconductor in Ambegaokar–Baratoff and de Gennes theories, J. Supercond. Nov. Magn. **35** (2022) 1421.

11. I. Mukherjee, D. Rakshit, **P. Mandal**, Ajay Kumar Ghosh, Suppression of critical temperature and superfluid phase stiffness by magnetic Ni and nonmagnetic Zn in $Y_3Ba_5Cu_8O_{18-\delta}$ superconductors, Appl. Phys. A **129** (2023) 763.

12. I. Mukherjee, **P. Mandal**, Ajay Kumar Ghosh, Effect of insulating dense pinning centers on pinning potential and transport critical current density of YBCO superconductors, Physica C **616** (2024) 1354410.

13. S. Mollah, **P. Mandal**, T. Sk, S. Haldar, Ajay Kumar Ghosh, On the low temperature conduction mechanism of $Ba_{1-x}K_xBiO_3$, AIP Conference

Proceedings 2220 (2020) 110044.

14. T. Sk, **P. Mandal**, D. Rakshit, I. Mukherjee, R. K. Saha, Ajay Kumar Ghosh, Effects of inter-granular Sn on transport and magnetic properties of polycrystalline GdBCO superconductors, Appl. Phys. A **130** (2024) 544.

15. D. Rakshit, **P. Mandal**, A. K. Ghosh, Magnetically coupled line vortex pinning in EBCO by Sn nanoparticles, 2024 (Submitted).

Conferences

1. **P. Mandal**, D. Rakshit, I. Mukherjee, T. Sk, Ajay Kumar Ghosh, Voltage nonlinearity and its dependence on the current sweeping rate in NBCO superconductor, 28^{th} National Symposium on Cryogenics and Superconductivity, Cryogenics Engineering center, Indian Institute of Technology Kharagpur, Kharagpur, 721302, India; October 18-21, 2022.

2. **P. Mandal**, Ajay Kumar Ghosh, Unusual high pinning exponent in Ni doped YBCO superconductor, 4^{th} International Conference on Condensed Matter and Applied Physics (ICC2023), Government Engineering College, Bikaner 334001, Rajasthan, India; October 09-10, 2023.

3. S. Mollah, **P. Mandal**, T. Sk, S. Haldar, Ajay Kumar Ghosh, On the low temperature conduction mechanism of $Ba_{1-x}K_xBiO_3$, 3^{rd} International Conference on Condensed Matter and Applied Physics (ICC2019),

Government Engineering College, Bikaner 334001, Rajasthan, India; October 14-15, 2019.

4. D. Rakshit, **P. Mandal**, Ajay Kumar Ghosh, A study of the transport critical current density in Ce doped EBCO superconductors, International Conference on Condensed Matter (ICCM-21), The Academy of Sciences, Chennai, India; October 28-30, 2021, in Virtual mode.

5. D. Rakshit, **P. Mandal**, T. Sk, Ajay Kumar Ghosh, Junction resistance for different energy gaps in EBCO in de Gennes and Ambegaokar-Baratoff theories, 28^{th} National Symposium on Cryogenics and Superconductivity (NSCS28); Cryogenics Engineering center, Indian Institute of Technology Kharagpur, Kharagpur 721302, India; October 18-21, 2022.

6. I. Mukherjee, **P. Mandal**, Ajay Kumar Ghosh, Transport critical current density in superconducting Y-358, 28^{th} National Symposium on Cryogenics and Superconductivity (NSCS28); Cryogenics Engineering center, Indian Institute of Technology Kharagpur, Kharagpur 721302, India; October 18-21, 2022.

Contents

Chapter 1

Introduction

1.1 Critical current density

Since the discovery of cuprate high-temperature superconductors (HTS), several studies have been carried out on the critical current density (J_c) in the last three decades. In general, J_c is a measure of the current carrying capability of a superconductor. It is defined as the maximum current density that a superconductor can carry, beyond which the superconducting state of the material enters a normal resistive state. Though the HTS superconductors exhibit promisingly higher current density, the maximum current density is limited to $\sim 5.0\times10^{12}$ A/m^2 [1, 2]. In single crystals of YBaCuO superconductor films, a peak J_c of approximately 2-3 MA/cm^2 has been recorded at a temperature of 77.0 K [3]. In a recent investigation of $YBa_2Cu_3O_{7-\delta}$ (YBCO) thin films, researchers observed a remarkable J_c of 90 MA/cm^2 at 5.0 K in self-field condition [1]. Bulk superconductors, however, typically exhibit J_c of a few orders of magnitude lower compared to that of the single

crystal and film. One of the major reasons for such a high critical current is the presence of a large number and variety of defects that may act as pinning centers. Impurities, oxygen vacancies, dislocations and stacking faults are a few examples of intrinsic defects. In addition to the intrinsic defects, grain boundaries also act as pinning centers in bulk HTS [4]. These defects resist dissipation in the systems by controlling the motion of the vortices. However, adding artificial pinning centers to the intergranular regions may affect the pinning mechanism, resulting change in the J_c. The nature of the pinning depends on the size, shape, orientation, dimension, conductivity, density and magnetic nature of the added pinning centers [5 - 7]. Dimension of a pinning center is important in controlling J_c. Different types of nanostructures have been used as pinning centers such as zero-dimensional nanoparticles [8, 9], one-dimensional nanorods [10, 11], two-dimensional nano planes [12] and three-dimensional nanorods [13]. The optimization of the size of the artificial pinning centers is crucial to ensure high performance for the superconductors. In general, vortices are strongly pinned when the size of a pinning center matches with the core of the vortices.

The impact of particle size on the flux pinning and J_c of YBCO single grain has been investigated by adding Al_2O_3 particles of two different sizes. Nanoparticles of an average diameter of 20 nm and microparticles of an average diameter of 2.27 μm have been added to YBCO. The study shows that flux pinning is closely dependent on the size of the added pinning centers. It is found that Al_2O_3 nano particle is more effective for enhancing J_c [14]. The role of the addition of the nanorod in the RBCO superconductors has been discussed [15 - 17]. Size matching of nanorods with the core of the vor-

tices is very effective in pinning vortices and results in an improvement in J_c. A study on the YBCO-BZO composite shows the highest J_c of 4.1 MA/cm^2 at 77.0 K and 12.2 MA/cm^2 at 65.0 K for the 1.0 vol % BZO-doped sample. Further increase in the density of BZO results in lowering the J_c **[18]**. Therefore up to a certain concentration of additional pinning centers at a given temperature and applied magnetic field, improved pinning mechanism and J_c may be observed.

It is known that J_c depends on the temperature (T), applied magnetic field (H) and density of the pinning centers (n_p) **[8, 10]**. Two types of J_c are generally measured, one is the transport critical current density (J_{ct}) and the other is the magnetic critical current density (J_{cm}). However, in HTS, the analysis and interpretation of J_{ct} and J_{cm} extracted from experimental data is in general complex. Due to its granular nature, both intergranular and intragranular transport currents coexist. J_c obtained from the transport measurement in zero field is far less than the J_c obtained from magnetic measurement. A few possible reasons for obtaining low J_c in transport measurement are (i) anisotropy in conductivity, (ii) redistribution of supercurrents at high-angle grain boundaries, (iii) the presence of impurities formed during sample synthesis and (iv) the presence of porosity, microcracks and other variations of crystal structure **[19]**.

In the present thesis, we have considered the two levels of disorders in the cuprate superconductors to study the impact of the pinning centers on the J_c and other superconducting properties. Several concentrations of microparticles and nanoparticles have been used to introduce additional pinning centers in the intergranular region of pure cuprate superconductors. Current-voltage

(IV) characteristics and irreversible magnetization (ΔM) have been used to extract the critical current densities. Temperature and magnetic field dependence of transport and magnetic critical current density has been studied and analyzed in pure and hybrid cuprate superconductors with different pinning center densities. The role of artificial pinning centers on critical current densities has been studied.

1.2 H-T phase diagram

The vortex systems in unconventional superconductors have been studied for several decades. A typical magnetic field versus temperature (H-T) phase diagram of RBCO has been shown in **Figure 1.2.1** **[20- 23]**. In type II superconductors, the vortex phase mostly depends on the temperature (T), external magnetic field (H), current density (J) and the pinning mechanism. In the absence of an external magnetic field and at low temperatures, the phase of the superconducting order parameter exhibits a quasi-long range ordered state. In the case of the low magnetic field $H < H_{c1}$ which is the lower critical field, total flux exclusion takes place. A type II superconductor exhibits perfect diamagnetism below H_{c1} shown in the H-T diagram. As the applied magnetic field increases above H_{c1}, quantized magnetic flux (Φ_0 = hc/2e $\approx 2\times10^{-7}$ G.cm^2) form Abrikosov-Gorkov (AG) vortex state. The magnetic flux penetrates the superconductors in the form of Abrikosov vortices **[24]**. Abrikosov vortices tend to arrange themselves in the form of a triangular lattice **[21, 22]**. An increase in the applied field enhances the density of vortices and starts to overlap. An overlap of the magnetic fields from neighbouring vortices results

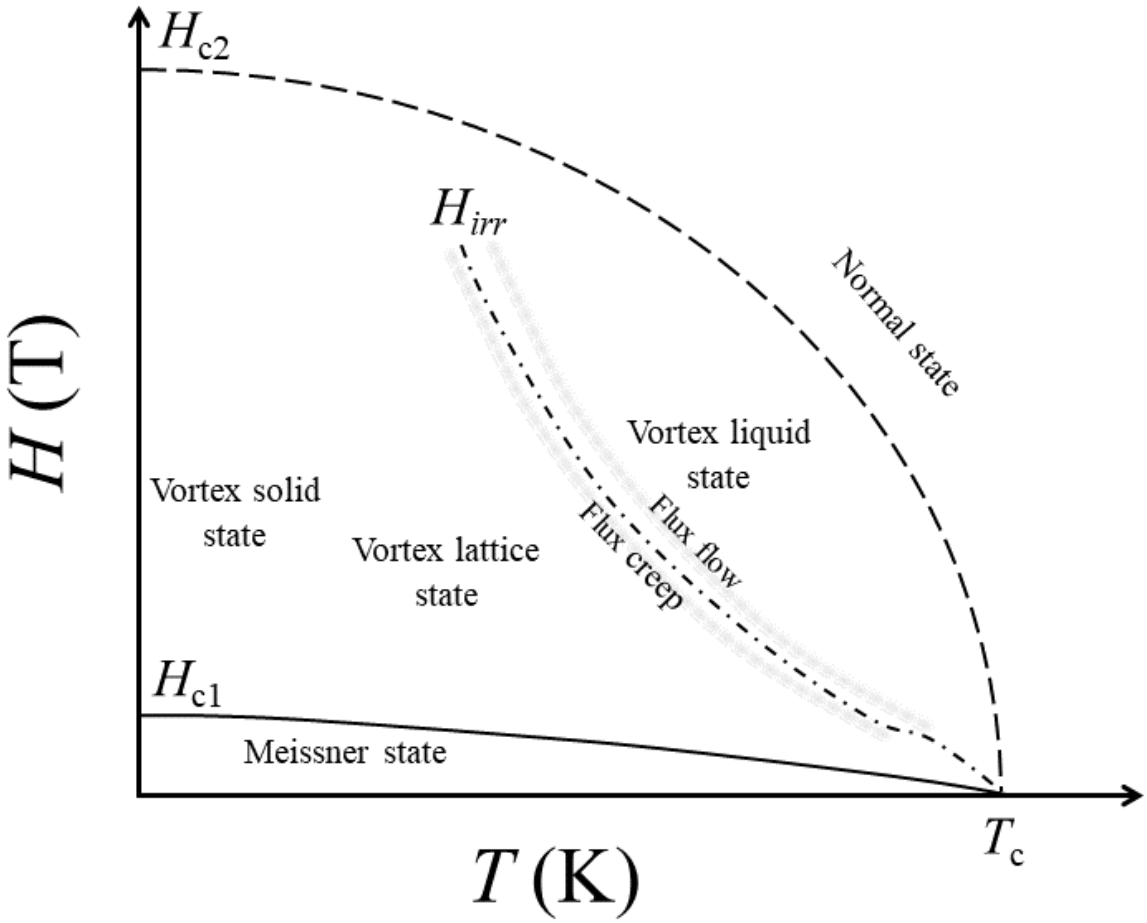

Figure 1.2.1: Magnetic field (H) - Temperature (T) phase diagram of RBCO.

in an array of vortices constituting a continuum of Abrikosov vortices. Above the H_{c2}, the sample loses its superconducting properties and the normal state is observed.

It is known that vortices interact with the pinning centers and other vortices. Different vortex phases are observed in the mixed state due to (i) the interplay of vortex-vortex interactions, (ii) thermal fluctuations, (iii) different kinds of disorder and (iv) the anisotropy [23]. As a result, J_c can vary by orders of magnitude and show different dependencies on temperature (T) and magnetic field (H). At lower T and higher H, the number of vortices increases, forming a solid phase near absolute zero temperature and a liquid

phase at a relatively high temperature and intermediate H. In the solid phase, vortices are fixed at a particular position following a regular pattern so that there exists long-range order and hence the J_c is comparatively high. In the presence of random pinning centers, the long-range order is affected. Though long-range order is lost there exists a short-range order of vortices and this phase is called the vortex glass phase. As the current density, J, is applied to the vortex system, pinned vortices may unpin under the action of the Lorentz force. Therefore pinning force and Lorentz force act in reverse manners. As the pinning force dominates over the Lorentz force, a very slow movement of vortices takes place, called flux creep. On the other hand, the domination of Lorentz forces faster the flux motion, called flux flow. Sufficiently high current density unpin the vortices and they start to move making the system dissipative and reducing J_c. These free vortices act like vortex fluid and the phase is called vortex liquid phase or flux liquid phase **[25]**. The domination of the thermal fluctuations is higher in vortex liquid phases. The vortex solid phase and vortex liquid phase are separated by a line called irreversible line or melting line **[26, 27]**. Along the melting line, the depinning of vortices takes place and flux creep becomes flux flow. The melting process can begin at temperatures considerably lower than H_{c2} in cuprate superconductors. The vortex fluid phase is completely disordered and does not undergo a real phase transition to the normal phase. Instead, they are in the same phase and are connected by a continuous crossover. Above H_{c2} and/or T_c superconducting nature no longer exists and the sample enters the normal state.

1.3 Problems of modern era in (i) H-T and (ii) J_c

Although high-temperature superconductors provide high J_c, the current carrying capacities of HTS are still far from theoretical limits. One of the major motivations of researchers is to achieve the maximum J_c at a reasonably high temperature and magnetic field. The maximum current density beyond which the superconductivity is lost in the HTS can be controlled in several ways. By enhancing the pinning one can maximize J_c in extreme conditions. It is known that YBCO and other high-temperature superconductors exhibit anisotropic properties. The current density can also vary depending on the orientation of the applied current and magnetic field. It is very important to mention that the presence of material defects, impurities, micro-cracks and grain boundaries can locally alter the effective J_c in HTS. At a particular combination of H and T in H-T phase diagram, the arrangement of vortices is very crucial in maximising the J_c. A sample having (i) a specific H-T phase diagram with a higher and almost constant H_{c2} with T and (ii) high J_c is known to be potential for different technological applications. This scenario can be achieved by lowering the dissipation of moving vortices. The motion of the vortices reduces the J_c differently depending on conditions. In H-T phase diagram, the irreversible line, the possibly melted vortex liquid above that line, nearly logarithmic time relaxation of magnetic properties below it and collective behaviour of vortices in the presence of disorder in several HTS-based systems are a few examples of areas in which research on J_c will be necessary. Moreover, variations of J_c within vortex-liquid and vortex-solid states are not well understood in several HTS and related sys-

tems. Several phenomena in vortex pinning on the basis of the H-T phase diagram are currently unsettled and people are looking for explanations both theoretically and experimentally to enrich the knowledge of how to enhance J_c in HTS.

1.4 Temperature (T) and magnetic field (H) dependence of critical current density

Transport critical current density can be successfully extracted from the current-voltage (IV) characteristics. A suitable electric-field (E) criterion is chosen to find out the corresponding critical current (I_c) [28]. However, the selection of suitable electric-field criteria is one of the challenging tasks for the determination of the J_c because it strongly influences the nature of $J_c(T)$, particularly in the low-temperature region. Both the intergrain (J_c) and intragrain (J_{cG}) critical current density show similar kinds of temperature dependencies in several HTS [29]. Different types of dependencies of J_c on the T and H are found depending on the various parameters such as pinning density and nature.

An important aspect is the temperature variation of transport critical current density in the flux pinning scenario. In granular superconductors, several types of vortex pinning have been observed [6]. In the case of single vortex pinning in type-II superconductors, the temperature dependence of J_c is described by the relation, $J_c(T) = J_c(0)[1-\varepsilon^2]^n$, where n is an exponent revealing the nature of the pinning and $\varepsilon = T/T_c$ is the reduced temperature. The nature of the pinning is described by the variation of the Ginzburg-Landau

order parameter ($|\psi|$). $n = 7/6 \sim 1.2$ holds for δT_c pinning caused by the spatial variation of $|\psi|$ in the T_c and $n = 5/2$ holds for δl pinning caused by the spatial variation in the charge carrier mean free path (l) near lattice defects [30].

In the case of hybrid superconductors, where additionally incorporated particles act as pinning centers, the temperature dependence of $J_c(T)$ can also be explained in the weak and strong pinning framework. The presence of weak pinning in the superconductors results in a rapid reduction of critical current density described by the expression $J_c^{wk}(T) = J_c^{wk}(0)exp(-\frac{T}{T_0})$, where $J_c^{wk}(0)$ is the weak pinning contribution at 0.0 K and T_0 is associated to the characteristic vortex pinning energy of weak defects [30, 31]. As the density of the weak pinning centers increases, collective pinning comes into play. The effect of a large collection of weak pinning centers has been discussed in the weak collective pinning theory developed by Larkin and Ovchinnikov [32]. On the other hand, strongly correlated pinning centers hold the vortices strongly and result in slower and smooth decay of J_c with T following the expression $J_c^{str}(T) = J_c^{str}(0)exp[-3(\frac{T}{T^*})^2]$, where $J_c^{str}(0)$ is the strong pinning contribution at 0.0 K and T^* is the corresponding characteristic vortex pinning energy of strong pinning centers [30, 31].

The temperature variation of J_c close to T_c in the vortex liquid state has been explained by an exponential function, $J_c(T) = J_c(0)exp(-T/T_{0J})$, where $J_c(0)$ is the critical current density at 0 K and T_{0J} is the characteristic temperature. The change in the concentration of pinning centers (x) in the intergranular regions affects T_{0J}. Therefore T_{0J} is very sensitive to the density (n_p) or concentration of pinning centers.

Temperature dependence of transport J_c for granular superconductors is interpreted in the framework of Ambegaokar- Baratoff (AB) and Ginzburg-Landau (GL) description. The general expression for the temperature dependence is given as $J_c(T) = J_c(0)[1 - \frac{T}{T_c}]^{\alpha}$, where α = 1.5 is related to GL and α = 0.5 is related to AB description. The curvature is concave type in the GL variation and convex type in the AB variation. An important analysis of both $J_c(T)$ and $J_{cG}(T)$ shows the crossover from Ambegaokar-Baratoff-like (AB) to Ginzburg-Landau (GL) temperature dependence. It has been found that this crossover is independent of the defects present, the direction of current is flowing, ceramic or granular nature [29, 33].

Magnetic critical current density (J_{cm}) is extracted from the hysteresis loop using critical state and extended Bean's model [34]. According to Bean's model, the critical current density is proportional to the irreversible magnetization (ΔM). For a rectangular slab of finite dimension the exact equation for J_{cm} is given as, $J_{cm} = \frac{40 \times \Delta M}{b(1-\frac{b}{3a})}$, Where a and b ($a > b$) are length and width of the rectangular bar-shaped sample used for VSM measurement. In the measurement, the magnetic field is set to be directed along the perpendicular to the $a - b$ plane of the sample. The irreversibility field (H_{irr}) has been extracted using a criterion $\Delta M \sim 0$ emu/cm^3.

The variation of $J_{cm}(H)$ shows different behaviour in different field regions. At the low field region, J_{cm} is observed as almost independent of H due to the low density of flux lines. At low H, J_{cm} of YBCO thin film exhibits a plateau [35] type variation. In this field region, vortices are pinned individually and plateau-like dependence suggests that vortices are strongly pinned by defects and pinning centers [36]. In the polycrystalline sample,

J_{cm} varies weakly with H at the low field region, indicating the possibility of single vortex pinning. In the intermediate field range J_{cm} experience a power law dependence, $J_{cm} \propto H^{-\alpha}$ [37, 38]. A low value of α indicates soft field dependence of J_c and presence of collective pinning and strong pinning mechanism. The power-law behaviour persists over a wide range of fields and temperatures in the intermediate region for YBCO with $\alpha = 0.6$. As the field strength increases, a rapid decline in J_{cm} is observed with a higher value of α.

Variation of α as a function T suggests that the dominant pinning mechanism is also T dependent. The variation reveals the possibility of crossover from collective pinning to a strong pinning regime. In the intermediate field range, variation of $J_{cm}(H^{-1/2})$ indicates how inter-vortex separation is crucial in vortex pinning. The addition of nanoparticles affects the pinning mechanism and hence the variation of $J_{cm}(H^{-1/2})$.

An important analysis of the dependence of J_{cm} on the H and the density of pinning centers (n_p) has been carried out in the framework of the collective pinning due to large numbers of weak pinning centers [21, 32]. According to the theory of collective pinning, the dependence of J_{cm} is described by following an exponential equation, $J_{cm} = A.exp[-(m/n_p)H^{1.5}]$, where m and A are constant and n_p is the density of pinning centers [23].

1.5 Controlling J_c in Layered structure of HTS

In **Figure 1.5.1**, we have shown a typical structure of a unit cell of orthorhombic $RBa_2Cu_3O_{7-\delta}$ (R = Rare Earth), δ is the oxygen content. RBCOs are

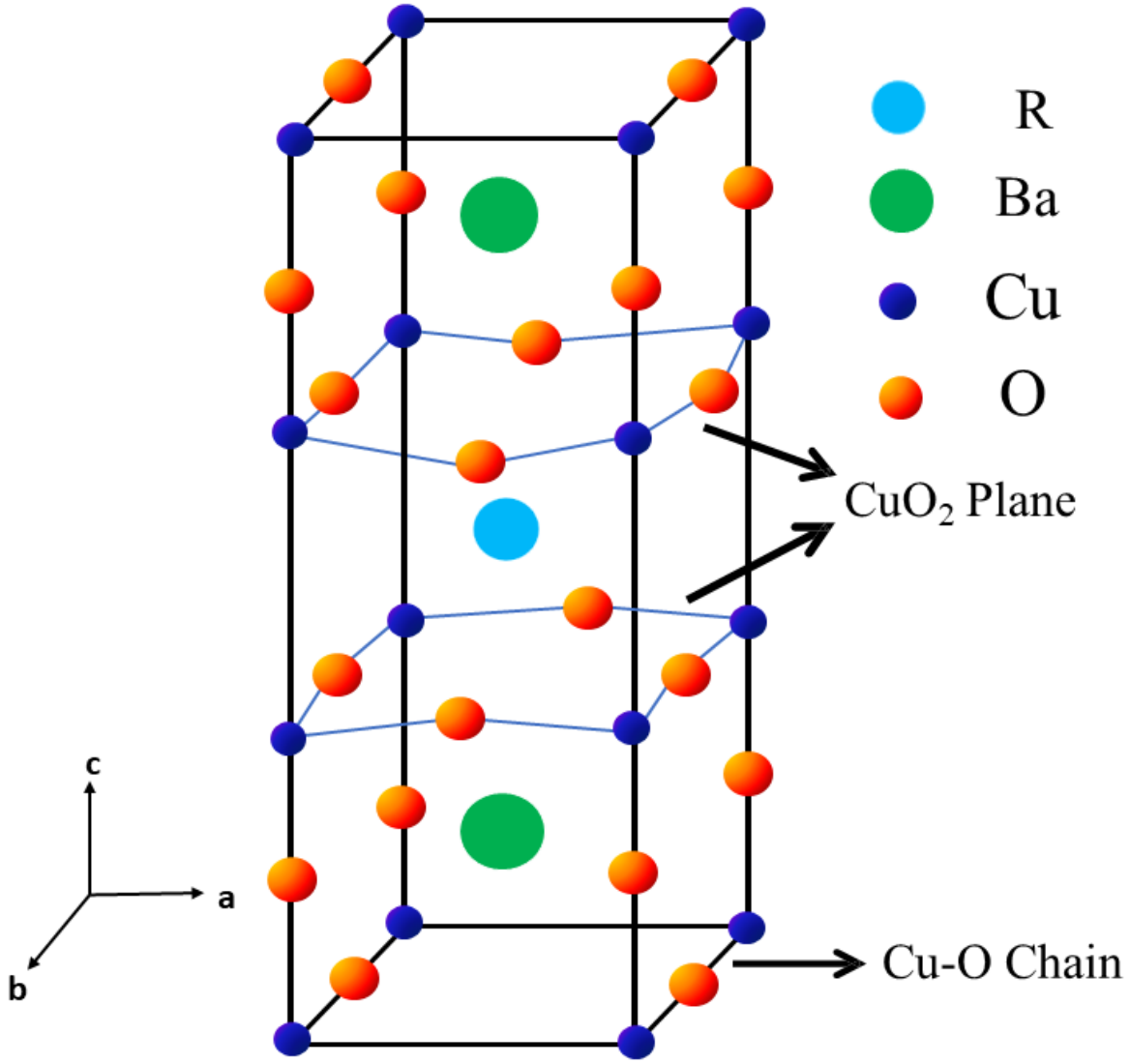

Figure 1.5.1: Unit cell structure of oxygen-deficient $RBa_2Cu_3O_{7-\delta}$ (R = Rare Earth)

layered superconductors. A unit cell consists of two CuO_2 planes in and CuO chains (b-direction). Typical lattice parameters of the RBCO are a = 3.82 Å, b = 3.89 Å and c = 11.68 Å. Separation between two CuO_2 is $\sim$ 3.2 Å. Whereas the distance between the CuO_2 plane and CuO is $\sim$ 4.25 Å. Variations in the lattice parameter can introduce defects or strain in the crystal structure. These defects can act as pinning centers, which can change the J_c. δ plays a crucial role in determining whether RBCO is in the orthorhombic or tetragonal phase. The orthorhombic phase is superconducting while the

tetragonal phase is non-superconducting. Depending on the value of δ and temperature RBCO may become orthorhombic ($0.0 < \delta < 0.5$) or tetragonal ($0.5 < \delta < 1.0$) [39]. The oxygen deficiency acts as intrinsic pinning centers and enhances J_c in orthorhombic RBCO. However, optimization of δ is very important in controlling J_c. In granular superconductors, angles between grain boundaries affect the J_c. Higher misorientation angles lower the J_c because they introduce a weak-link network into the superconducting path. In orthorhombic RBCO, CuO_2 planes play the key role in the origin of superconductivity. Therefore, charge carriers remain in CuO_2 planes whereas CuO chains act as charge reservoirs and supply carriers to CuO_2 planes. Charge carrier density in CuO_2 planes and their tunnelling between planes influences the onset critical temperature T_c of superconducting cuprates. The interlayer coupling between the CuO_2 is affected due to changes in the rare earth atoms and consequently J_c is affected. J_c can also be controlled from outside the grain by introducing artificial pinning centers in the intergranular regions. Additional pinning centers in the form of non-superconducting particles are introduced in the grain boundaries. BZO microparticles and BTO nano particles are used as pinning centers. These particles participate in the flux pinning mechanism and hence modify J_c. However, optimization of the size and density of pinning centers is important to achieve improved J_c.

1.6 Sample selection

Although the RBCO system has strong intrinsic pinning and high critical current density, several attempts have been made to study the critical current

density by including additional pinning sites in the intergranular regions. We have selected four RBCO (R = Y, Gd, Nd, Eu)(**S1**, **S2**, **S3**, **S4**) systems to study the effect of intrinsic magnetic moment of R on J_c due to the interlayer coupling of CuO_2 planes. Also, changes in T_c of YBCO have been studied while Y is replaced by Gd, Nd, and Eu. We have selected a composite sample of YBCO and 5.0 wt% $BaZrO_3$ (**S5**) to study current density using different electric field criteria for the extraction of J_c [28]. Several studies have shown that $BaZrO_3$ act as excellent pinning centers and enhances the J_c. The enhancement of the J_c is possible by optimizing the concentration, size, shape and other properties of added particles [6]. We have used BZO particles of size $\sim$ 10 μm as additional pinning centers and introduced them in the intergranular region of YBCO. Pure YBCO (**S6**) and four composite samples (**S7** - **S10**) with different wt% BZO have been chosen to understand the role of BZO on granularity, Superfluid phase stiffness (SPS), current density and the nature of pinning. The inclusion of $BaTiO_3$ (BTO) nanoparticles is also another important way of changing the nature and strength of pinning centers. In the composite sample of YBCO-BTO, J_c is enhanced by $\sim$ 250 % compared to that of the pure YBCO, throughout the applied magnetic field range [40]. In the presence of a magnetic field, the nature pinning in YBCO by $BaTiO_3$ (BTO) nanoparticles of size $\sim$ 100 nm has been studied. We have selected the pure YBCO (**S11**) and four composite samples (**S12** - **S15**) of YBCO and BTO with different BTO percentages to explore several aspects of vortex pinning and possibility of enhancing J_c. The addition of nanoparticles in NBCO has also shown an improvement of J_c. Composite samples of NBCO-BZO have shown improvement in the J_c [41]. We have used Sn

nanoparticle in NBCO to study the role of Sn on the J_c and other transport properties. We have chosen the pure NBCO (**S16**) and four such composite samples (**S17** - **S20**) of NBCO and Sn nanoparticles of size $\sim$ 150 nm with different Sn concentrations for the present research works.

1.7 Outline of the thesis

The structure of the present thesis is summarized in several chapters. Details of the sample synthesis method called solid state reaction method have been discussed in **Chapter 2**. Also, the characterization and measurement process and their working principle have been illustrated in the same chapter. In **Chapter 3**, we have studied the role of rare earth elements in critical current density in some pure R-123 (R = Y, Gd, Nd, Eu) systems [42]. The determination process of J_c using a suitable electric field criterion as well as the sensitiveness of the J_c on criteria selection have been studied in **Chapter 4** [43]. How SPS and J_c are affected due to the inclusion of the micro-size particle in the inter-granular regions of YBCO have been studied in **Chapter 5** [44]. In **Chapter 6**, we have analyzed magnetic data to study the crossover from collective pinning to strong pinning due to the addition of BTO nanoparticles in the inter-granular regions of YBCO [45]. Composite systems of NBCO and Sn nanoparticle have been studied and possible weak pinning scenarios have been discussed in **Chapter 7** [46].

1.8 References

1. A. Stangl, A. Palau, G. Deutscher, X. Obradors, T. Puig, Scientific Reports **11** (2021) 8176.

2. L. Civale, Proc. Natl. Acad. Sci. **116** (2019) 10201.

3. V. M. Pan, E. A. Pashitskii, S. M. Ryabchenko, V. A. Komashko, A. V. Pan, S. X. Dou, A. V. Semenov, C. G. Tretiatchenko, Y. V. Fedotov, IEEE Trans. Appl. Supercond **13** (2003) 3714.

4. A. A. Polyanskii, A. Gurevich, A. E. Pashitski, N. F. Heinig, R. D. Redwing, J. E. Nordman, D. C. Larbalestier, Phys. Rev. B **53** (1996) 8687.

5. T. J. Haugan, T. Puig, K. Matsumoto, J. Wu, Supercond. Sci. Technol. **33** (2020) 040301.

6. M. Miura, B. Maiorov, M. Sato, M. Kanai, T. Kato, T. Kato, T. Izumi, S. Awaji, P. Mele, M. Kiuchi, T. Matsushita, NPG Asia Mater. **9** (2017) e447.

7. A. E. Koshelev, A.B. Kolton, Phys. Rev. B **84** (2011) 104528.

8. A. Palau, E. Bartolome, A. Llordes, T. Puig, X. Obradors, Supercond. Sci. Technol. **24** (2011) 125010.

9. T. Haugan, P. N. Barnes, R. Wheeler, F. Meisenkothen, M. Sumption, Nature **430** (2004) 867.

10. P. Mele, K. Matsumoto, A. Ichinose, M. Mukaida, Y. Yoshida, S. Horii, R. Kita, Supercond. Sci. Technol. **21** (2008) 125017.

11. A. Ichinose, K. Naoe, T. Horide, K. Matsumoto, R. Kita, M. Mukaida, Y. Yoshida and S. Horii, Supercond. Sci. Technol. **20** (2007) 1144.

12. C. F. Tsai, J. Huang, J. Lee, F. Khatkhatay, L. Chen, A. Chen, Q. Su, H. Wang, Physica C **510** (2015) 13.

13. T. Horide, K. Matsumoto, A. Ichinose, M. Mukaida, Y. Yoshida, S. Horii, Supercond. Sci. Technol. **20** (2007) 303.

14. N. Moutalbi, J. G. Noudem, A. M'chirgui, Physica C **503** (2014) 105.

15. J. Z. Wu., Jack J. Shi, J. F. Baca, R. Emergo, T. J. Haugan, B. Maiorov, T. Holesinger, Supercond. Sci. Technol. **27** (2014) 044010.

16. V. Selvamanickam, M. H. Gharahcheshmeh, A. Xu, E. Galstyan, L. Delgado, C. Cantoni, Appl. Phys. Lett. **106** (2015) 032601.

17. A. Goyal, S. Kang, K. J. Leonard, P. M. Martin, A. A. Gapud, M. Varela, M. Paranthaman, A. O. Ijaduola, E. D. Specht, J. R. Thompson, D. K. Christen, S. J. Pennycook, F. A. List, Supercond. Sci. Technol. **18** (2005) 1533.

18. S. H. Wee, Y. L. Zuev, C. Cantoni, A. Goyal, Scientific Reports **3** (2013) 2310.

19. S. Jin, T. H. Tiefel, R. C. Sherwood, M. E. Davis, R. B. van Dover, G. W. Kammlott, R. A. Fastnacht, H. D. Keith, Appl. Phys. Lett. **52** (1988) 2074.

20. N. C. Yeh, Phys. Rev. B **43** (1991) 523.

21. G. Blatter, M. V. Feigel'man, V. B. Geshkenbein, A. I. Larkin, V. M. Vinokur, Rev. Mod. Phys. **66** (1994) 1125.

22. E. H. Brandt, Rep. Prog. Phys. **58** (1995) 1465.

23. W. K. Kwok, U. Welp, A. Glatz, A. E. Koshelev, K. J. Kihlstrom, G. W. Crabtree, Rep. Prog. Phys. **79** (2016) 116501.

24. A. A. Abrikosov, Zh. Eksp. Teor. Fiz. **32** (1957) 1442 [Sov. Phys.-JETP **5** (1957) 1174.]

25. F. Bouquet, C. Marcenat, E. Steep, R. Calemczuk, W. K. Kwok, U. Welp, G. W. Crabtree, R. A. Fisher, N. E. Phillips, A. Schilling, Nature **411** (2001) 448.

26. M. P. A. Fisher, Phys. Rev. Lett. **62** (1989) 1415.

27. D. S. Fisher, M. P. A. Fisher, D. A. Huse, Phys. Rev. B **43** (1991) 130.

28. A. V. Pan, I. A. Golovchanskiy, S. A. Fedoseev, Euro. Phys. Lett. **103** (2013) 17006.

29. H. Darhmaoui, J. Jung, Phys. Rev. B **53** (1996) 14621.

30. Q. Wang, P. Jiang, M. Li, Y. Zhao, S. Zhang, X. Zhang, Y. Chen, Supercond. Sci. Technol. **37** (2024) 015006.

31. J. Gutiérrez, A. Llordés, J. Gázquez, M. Gibert, N. Romà, S. Ricart, A. Pomar, F. Sandiumenge, N. Mestres, T. Puig, X. Obradors, Nat. Mater. **6** (2007) 367.

32. A. I. Larkin, Yu. N. Ovchinnikov, J. Low Temp. Phys. **34** (1979) 409.

33. J. L. Cardoso, P. Pereyra, Phys. Rev. B **61** (2000) 6360.

34. G. Shams, M. Ranjbar, Bull. Mater. Sci. **45** (2022) 206.

35. B. Dam, J. M. Huijbregtse, F. C. Klaassen, R. C. F. van der Geest, G. Doornbos, J. H. Rector, A. M. Testa, S. Freisem, J. C. Martinez, B. Stäuble-Pümpin, R. Griessen, Nature **399** (1999) 439.

36. F. C. Klaassen, G. Doornbos, J. M. Huijbregtse, R. C. F. van der Geest, B. Dam, R. Griessen, Phys. Rev. B **64** (2001) 184523.

37. S. H. Wee, A. Goyal, P. M. Martin, J. Li, M. Paranthaman, L. Heatherly, Supercond. Sci. Technol. **19** (2006) L42.

38. Yu.N. Ovchinnikov, B.I. Ivlev, Phys. Rev. B **43** (1991) 8024.

39. J. D. Jorgensen, M. A. Beno, D. G. Hinks, L. Soderholm, K. J. Volin, R. L. Hitterman, J. D. Grace, I. V. Schuller, C. U. Segre, K. Zhang, M. S. Kleefisch, Phys. Rev. B **36** (1987) 3608.

40. P. P. Rejith, S. Vidya, J. K. Thomas, IOP Conf. Series: Materials Science and Engineering **73** (2015) 012146

41. A. O. Ijaduola, S. H. Wee, A. Goyal, P. M. Martin, J. Li, J. R. Thompson, D. K. Christen, Supercond. Sci. Technol. **25** (2012) 045013.

42. P. Mandal, D. Rakshit, I. Mukherjee, T. Sk., A. K. Ghosh, Phys. Lett. A **436** (2022) 128072.

43. P. Mandal, Ajay Kumar Ghosh, Mod. Phys. Lett. B **38** (2024) 2450050.

44. P. Mandal, D. Rakshit, T. Sk, Ajay Kumar Ghosh, J. Supercond. Nov. Magn. **35** (2022) 1079.

45. P. Mandal, D. Rakshit, T. Sk, Ajay Kumar Ghosh, Appl. Phys. A **129** (2023) 650.

46. P. Mandal, Ajay Kumar Ghosh, Transport critical current density in composite system of $NdBa_2Cu_3O_{7-\delta}$ and Sn nanoparticles, 2024 (Submitted).

Chapter 2

Experimental techniques

2.1 Introduction

Several high T_c pure and composite bulk polycrystalline superconductors have been synthesized and characterized. Using a standard solid state reaction method, we have prepared all the superconducting samples. Prepared samples have been characterized by scanning electron microscopy (SEM) using FEI-Inspect F50 SEM and X-ray diffraction (XRD) using Bruker D8 advance XRD. A standard four-probe method has been adopted for the transport measurements like $\rho(T)$ and IV. Magnetic measurements have been carried out using a 7.0 Tesla vibrating sample magnetometer, VSM (Cryogenics, UK). In this chapter, we have discussed in brief the equipment used and their working principle.

2.2 Solid state synthesis method

One of the major challenges is to prepare high-quality polycrystalline superconducting samples. Several methods, such as solid-state reaction method [1], the sol-gel method [2], coprecipitation method [3], have successfully produced good quality samples. We have used the solid state reaction method for the preparation of our samples. Phase formation, growth of grains, grain connectivity, porosity, compactness, the randomness of the angle between adjacent grains depend on the synthesis route and applied synthesis condition.

In the present thesis, we have synthesized five series of samples in the conventional solid-state reaction method [4]. The details of the series have been shown in **Table 2.1**. High pure commercially available powder of R_2O_3 (R = Y, Gd, Nd, Eu), $BaCO_3$, and CuO have been taken with proper stoichiometry. Mixing and grinding have been performed using agate mortar and pestle for $\sim$ 3 hours to achieve homogeneity throughout the sample. The mixed powder was then pressed into pellets (typical diameter 8.0 mm and thickness $\sim$ 0.5 - 0.7 mm) using a pelletizer die and a high-pressure hydraulic press. Calcination of sample pellets has been carried out around the temperature of 840 °C for 24 hours in a high-temperature tube furnace. During the calcination stage, the carbonates are decomposed into oxides and release the produced CO_2. Calcined pellets are again ground and mixed, the mixture is again pressed into pellets. The samples have been sintered around the temperature of 925 - 930 °C for 24 hours. The required R123 (R = Rare Earth) phase has formed during this sintering stage. Several sintering processes with intermediate grinding have been performed to get the final prepared sample.

Table 2.1: Prepared sample series in the present study

Serial number of series	Details of the series
Series I	$RBa_2Cu_3O_{7-\delta}$ with R = Y, Gd, Nd and Eu (**S1**, **S2**, **S3**, **S4**)
Series II	$YBa_2Cu_3O_{7-\delta}$ + 5.0 wt% $BaZrO_3$ (**S5**)
Series III	$YBa_2Cu_3O_{7-\delta}$ + x wt% $BaZrO_3$ with x = 0.0, 2.5, 5.0, 7.5, 10.0 (**S6**, **S7**, **S8**, **S9**, **S10**)
Series IV	$YBa_2Cu_3O_{7-\delta}$ + x wt% $BaTiO_3$ with x = 0.0, 2.0, 4.0, 8.0, 16.0 (**S11**, **S12**, **S13**, **S14**, **S15**)
Series V	$NdBa_2Cu_3O_{7-\delta}$ + x wt% Sn with x = 0.0, 0.5, 1.0, 1.5, 2.0 (**S16**, **S17**, **S18**, **S19**, **S20**)

Both the calcination and sintering have been done in the ambient pressure and normal air atmosphere. For the composite samples, additional elements have been mixed with pure R123 before the last sintering. The oxygen stoichiometry in the R123 unit cell can be controlled during the annealing. Annealing has been performed at a temperature around 450 °C for a longer time of 60 - 72 hours in an oxygen atmosphere and ambient pressure to minimize oxygen deficiency. In all stages, samples are cooled down slowly at a 2 °C/min rate to room temperature.

2.3 X-ray diffraction (XRD)

X-ray diffraction analysis (XRD) is a highly versatile technique that provides detailed information about the crystallographic structure, chemical composition, phase analysis, lattice parameters, and several other physical properties of a material **[5 - 10]**. The working principle of XRD is based on the constructive interference of monochromatic X-rays and a crystalline sample.

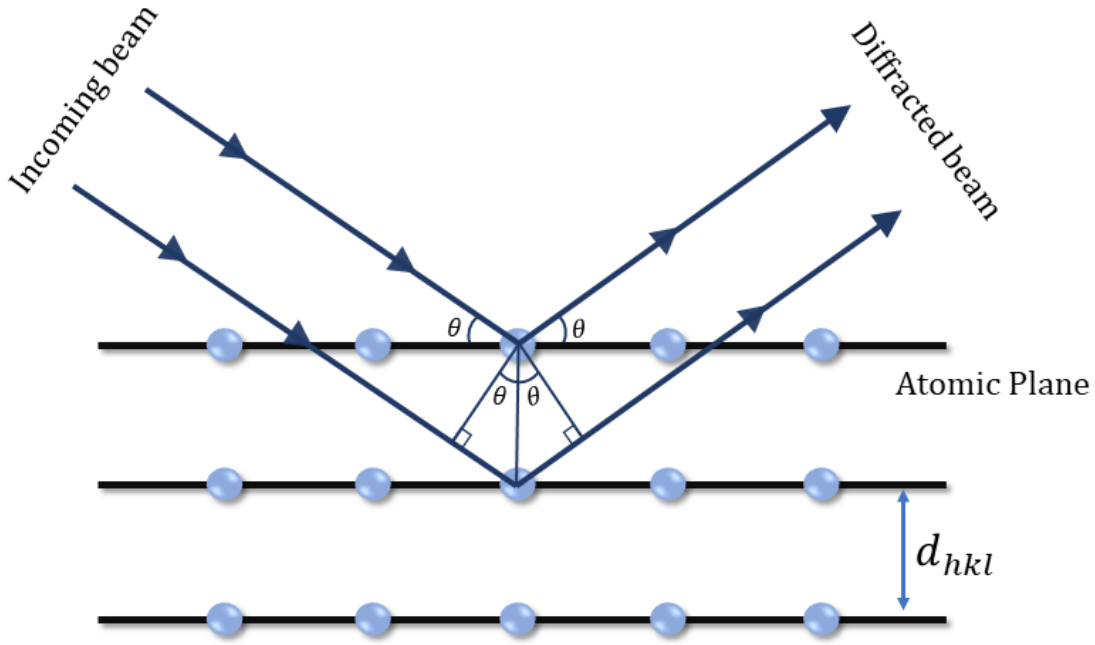

Figure 2.3.1: Schematic diagram of Bragg's diffraction of crystalline sample

When the incoming X-ray beam from a monochromatic X-ray source is incident onto a crystal surface, it interacts with the different atoms of crystal and diffracted. The interaction of incident rays with the sample produces constructive interference when path difference satisfies Bragg's Law; given as $2d_{hkl}\sin\theta = n\lambda$ where, n is an integer, λ is the wavelength of the X-rays. θ is the angle of the incident beams with the planes (hkl). d_{hkl} is the interplanar separation between the planes having Miller Indices (hkl). The scattering of X-rays from atoms produces a diffraction pattern, which contains information about the atomic arrangement within the crystal. A schematic diagram of Braggs diffraction of a crystalline sample has been shown in **Figure 2.3.1**.

Most of the powder diffractometers use Bragg-Bragmentano (BB) parafocusing geometry [11]. X-ray diffractometers are mainly made of three com-

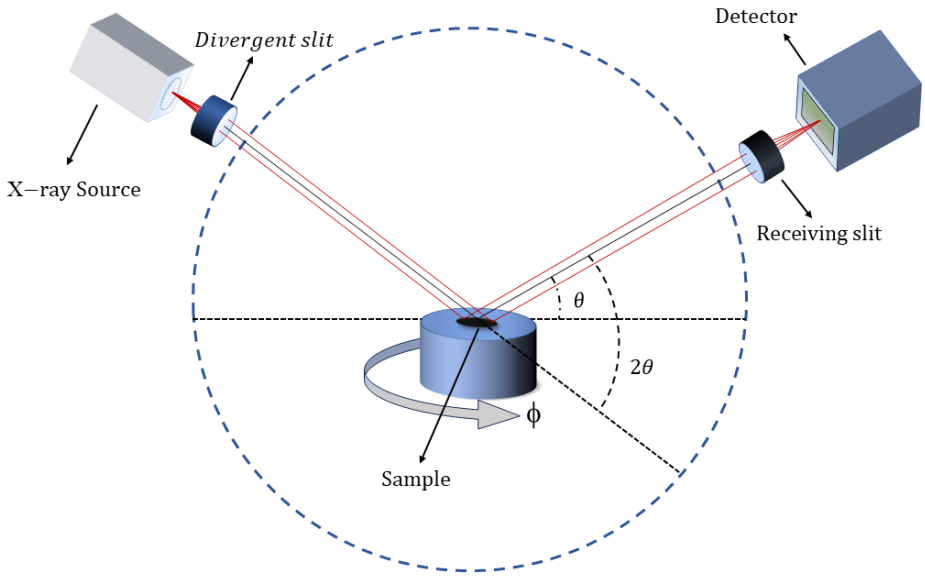

Figure 2.3.2: Schematic diagram of an X-ray diffractometer

ponents, (i) an X-ray tube, (ii) a sample holder, and (iii) an X-ray detector. Depending on the rotation of the component, BB geometry is classified into two categories. (i) θ:2θ: the X-ray tube fixed, the sample rotates at θ/min and the detector always at 2θ/min. (ii) θ:θ: the sample is fixed and both the X-ray tube and the detector rotate at the same rate at θ/min. In **Figure 2.3.2**, we have shown a schematic diagram of an X-ray Diffractometer. In a cathode ray tube, electrons are produced by heating a filament and accelerated toward the target by applying high voltage. Characteristics of X-ray spectra are produced due to the interaction of target materials with electrons. These X-rays are collimated and directed onto the sample. The reflected rays are collected in a detector and analyzed.

In our laboratory, we have used both XRD with θ:2θ and XRD with θ:θ geometry. Copper (Cu) is used as the target material. Produced characteristic X-ray spectra consist of several components like K_α and K_β. K_α consists

of $K_{\alpha 1}$ (λ_1 = 1.5406 Å) and $K_{\alpha 2}$ (λ_2 = 1.54439 Å) having comparable wave length. So we have used the average $\lambda = \frac{1}{2}(\lambda_1 + \lambda_2)$ = 1.5418 Å for analysis purpose. We have used the range of 2θ from 10° to 80°. We have taken the step size of 0.02° and scan time per step size is chosen to be 0.4 to 0.6 second depending on the requirement. The typical used voltage and current are 35.0 kV and 35.0 mA.

2.4 Field emission scanning electron microscope (FESEM)

Scanning Electron Microscopy (SEM) is a powerful high-resolution imaging technique used in various scientific fields to analyze the surface morphology and composition of specimens at a microscale and nanoscale level [12, 13]. A focused electron beam is incident over the surface of a specimen and interacts with the specimen. The interactions of these electrons with the specimen have been detected to create high-resolution images and gather information about its topography and composition. SEM generally consists of an electron source, condenser lenses, scanning coil, objective lens, sample chamber, stage, detector, and operating computers. A schematic diagram of SEM has been shown in **Figure 2.4.1**. In a standard electron microscope, electrons are produced using a crystal of lanthanum hexaboride (LaB_6) that is mounted on a tungsten filament. Field Emission Scanning Electron Microscope (FESEM), is an advanced variant of traditional scanning electron microscope (SEM). Where an extremely thin and sharp tungsten needle (tip diameter $\sim 10^{-7}$ to 10^{-8} m) is used as a cathode (electron source) in front

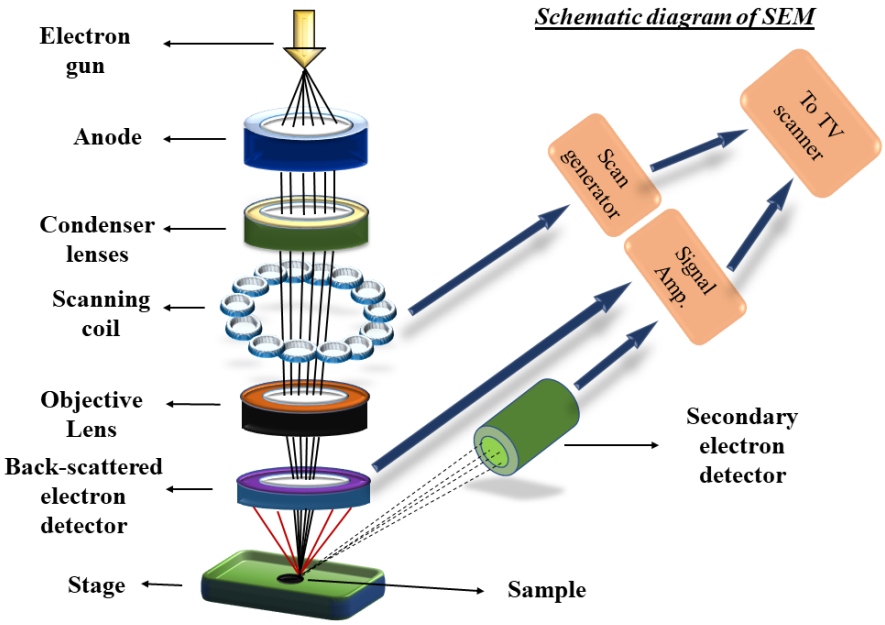

Figure 2.4.1: Schematic diagram of Scanning Electron Microscope (SEM)

of the primary and secondary anode, allowing for a highly focused and narrow electron beam. Emitted beams of high-energy electrons are focussed and controlled by magnetic lenses known as condenser lenses and objective lenses. These electron beams scan the specimen in a raster pattern, scanning the surface area in lines from side to side, top to bottom. The interaction of electrons with atoms on the surface of the sample creates signals in the form of secondary electrons, backscattered electrons, and rays that are characteristic of the specimen. Detectors in the microscope pick up these signals and create high-resolution images. During the full process a high vacuum of $\sim 10^{-7}$ Pa is maintained. Low-energy secondary electrons (SE) are emitted from the surface as a result of the primary electron beam impacting the specimen. A detector collects these secondary electrons to create a topographic image of the surface, that highlights surface features and topography. High-energy backscattered electrons (BSE) are deflected backward

when they interact with the specimen [14]. These BSE electrons are detected which provides information about the sample's atomic composition and density. When the primary electrons collide with the atoms in the specimen, they can cause the emission of characteristic X-rays. Energy-dispersive X-ray spectroscopy (EDS) or wavelength-dispersive X-ray spectroscopy (WDS) detectors are used to analyze these X-rays, providing information about the elemental composition of the sample.

SEM typically works on a voltage between 2.0 to 50.0 kV. The beam diameter is between 5.0 nm to 2.0 μm. For SEM imaging samples must be conducting, or have to be coated with gold prior to the SEM examination. We have used INSPECT F50 FESEM for analysis of our samples. As our samples are conducting at room temperature we have skipped the coating. So, we have attached the sample on the holder with the help of carbon tape and loaded the holders in the sample mounting stage. The electron beam is turned on when chamber pressure goes below 5×10^{-3} Pa. Typically working voltage range is set at 2.0 kV to 50.0 kV. We have set it to a suitable value of 20.0 kV and a spot size of 3.0 microns. Images have been taken at several magnifications ranging between 3000x and 10000x. However, the maximum achievable magnification is 160000x which can detect particles having size $\sim$ few nm. Information about the distribution of grains, grain size and porosity can be extracted from the SEM. Details analysis and study of individual SEM images have been shown in the respective chapters.

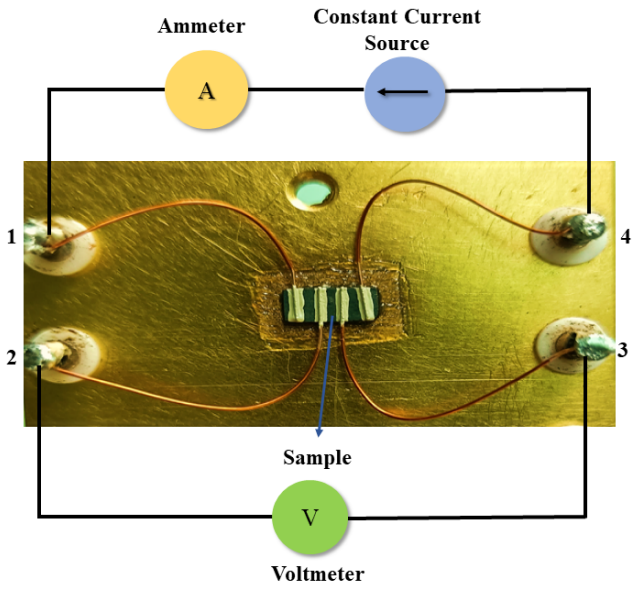

Figure 2.5.1: Representative four probe contact of a HTS sample piece mounted on a sample holder of cryogenerator

2.5 Four probe method

The four-probe method is a widely used electrical measurement technique for determining the resistivity, conductivity and sheet resistance of materials, particularly thin films, semiconductors and superconductors [15]. This method is used successfully to measure very low resistivity accurately and minimizes errors associated with probe contact resistances, making it a crucial tool for materials research and quality control [16]. A schematic diagram of four probe method has been shown in **Figure 2.5.1**. We have measured the electrical resistivity (ρ), as a function of T down to 10.0 K, and IV characteristics at several constant temperatures below T_c. A bar-shaped sample is cut from the sample pellet and attached to the sample holder with the help of Apiezon N Vacuum Grease, which allows the bar to be connected thermally but insulated electrically as shown in **Figure 2.5.1**. Using a rotary pump, the

sample has been kept in high vacuum. A Lakeshore temperature controller having a precision of 0.01 K is used to monitor and control the sample temperature. A Keithley's constant current source and nano voltmeter (precision $\sim$10 nV) have been used to apply current and to measure the voltage drop of the sample, respectively. A closed cycle refrigerator (CCR) (JANIS, USA), has been used for lowering the temperature of the sample down to 10 K. We have applied current through probes **1** and **4** known as current leads and measured the voltage drop between probe **2** and **3** known as voltage leads. Delta mode is used to measure $\rho(T)$ to eliminate any offset or noise voltage present in the system. The typical current used for measurement in delta mode is $\pm$ 1.0 mA. For the measurement of IV, we have used the current range from 100.0 nA to 5.0 mA in DC sweep mode. Transport measurements have been carried out in zero magnetic fields. All four probe contacts are made by Cu wire and pasted with silver conducting adhesive paste so that contact resistance is stable throughout the temperature range. Lets assume, sample dimension is $(l \times w \times t)$ and l_{vv} is the length between voltage leads where $l > l_{vv} > w > t$. The typical dimension of the bar-shaped sample used for transport measurement is 6.0 mm$\times$ 2.5 mm$\times$ 0.7 mm. Resistivity has been calculated using the formula $R = \frac{\rho \times l_{vv}}{w \times t}$.

2.6 Vibrating sample magnetometer (VSM)

A Vibrating sample magnetometer (VSM) is a sophisticated scientific instrument designed for the precise measurement of the magnetic properties of materials [17, 18]. The vibration of the sample in the magnetic field produced

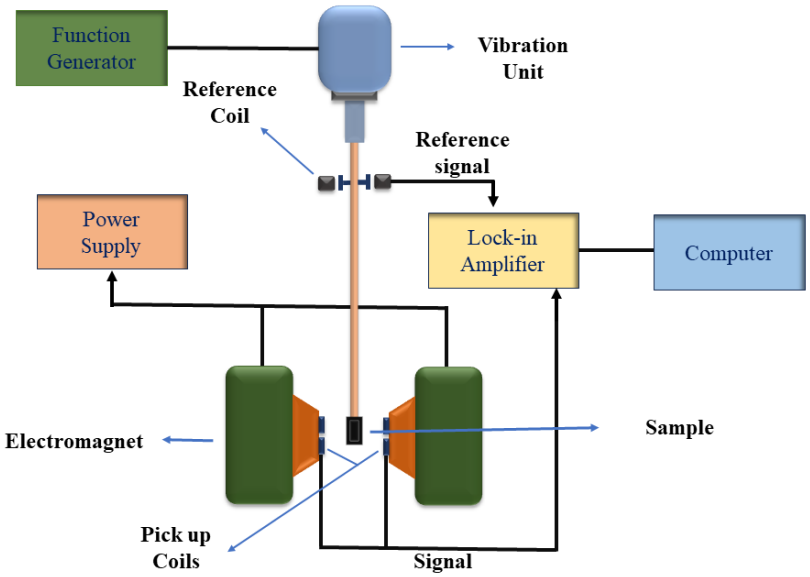

Figure 2.6.1: Schematic diagram of vibrating sample magnetometer (VSM)

an AC field. The magnetic moment is measured using an induction technique by detecting the AC field.

The main components of the VSM are (1) Vibrator and sample holder, (2) Lock-in amplifier, (3) Electromagnet and power supply, (4) a Pick up coil or detection coil, (5) Sensor coil, (6) Pulse Tube cryocooler (7) Helium compressor, (8) Temperature variation system, (9) Computer interface. The schematic diagram of a VSM is shown in **Figure 2.6.1**. A rigid rod is attached which oscillates vertically typically over 0.1 - 1.5 mm at a typical frequency of 21 Hz. At the lower of the rod, the sample is attached with the help of a straw and Kapton tape. Either magnetized sample or in response to an externally applied field, the oscillation induces an AC signal in a set of suitably placed pick-up or sense coils. Assuming that the moment is a magnetic dipole and the size of the sample is much smaller than the dimensions of the pick-up coils. The pick-up coils are connected in such a way that they are matched

and opposite senses. The voltage induced due to the vibration of the sample is proportional to the magnetic moment, m of the sample. The Vibrator creates the sinusoidal vertical motion of the sample within the pick-up coils with a 2 mm peak-to-peak amplitude. The lock-in amplifier (LIA) tuned with the reference signal from the vibrator control, detects the in-phase voltage from the pick-up coils. An optical sensor placed within the vibrator maintains the vibration amplitude at $\sim \pm$ 1 mm about the optical center. We have used the 7.0 T VSM for our measurement, which can achieve the lowest temperature of 1.6 K. Pulse Tube cryocooler has been used. It operates using a helium compressor. Cryogen-free magnet system enables to achieve low temperatures and high magnetic fields without the use of liquid helium or nitrogen. The accuracy of the VSM for magnetic moment measurement is $\sim 10^{-5}$ - 10^{-6} emu. For magnetization measurement, we have used the bar-shaped sample with typical dimensions 4.0 $\times$3.0 $\times$1.0 mm^3 and a mass of about 45 mg. The sample is attached to a straw of length 80 mm using Kapton tape in such a way that the plane of the sample becomes horizontal. The sample straw is then screwed to the vibrating rod with the help of the Perspex cone, which is shown in **Figure 2.6.2**. The vibrator is then connected to the vacuum sample chamber through a Gate valve. To ensure the sample position at the center of pick-up coils, we have searched for the extrema of the moment at a very low magnetic field ($< H_{c1}$) and temperature $\sim$ 2.0 K. $m(T)$ have been taken at several fields, H up to 7.0 T below T_c. Using Zero Field Cooling Cycle (ZFCC), Zero Field Cooling Warming (ZFCW), Field Cooled Cooling (FCC), and Field Cooled Warming (FCW), $m(T)$ measurements have been carried out. $m(H)$ have been measured at several constant T below T_c in the

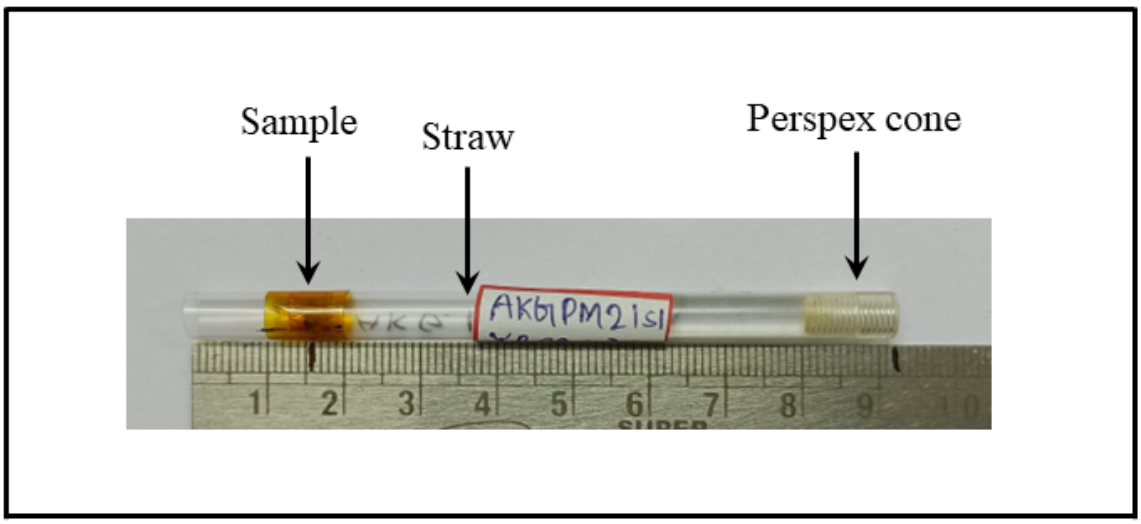

Figure 2.6.2: Schematic diagram of sample mounting straw used in VSM measurement

field range $\pm$7.0 T.

2.7 References

1. P. Pęczkowskia, P. Zachariaszb, M. Kowalikc, R. Zaleckic, C. Jastrzębski, Ceramics International **45** (2019) 18189.

2. M. Kakihana, L. Börjesson, S. Eriksson, P. Svedlindh, J. Appl. Phys. **69** (1991) 867.

3. K. Kellner, X. Z. Wang, G. Gritzner, D. Bgiuerle, Physica C **173** (1991) 208.

4. A. S. Sefat, Current Opinion in Solid State and Materials Science **17** (2013) 59.

5. W. L. Bragg, Nature **90** (1912) 410.

6. W. L. Bragg, Proc. R. Soc. Lond. **89** (1913) 248.

7. W. H. Bragg, W. L. Bragg, Proc. R. Soc. Lond. A **88** (1913) 428.

8. W. L. Bragg, Proc. R. Soc. Lond. **89** (1914) 468.

9. I. V. Zakharchenko, M. Muhammed, K. V. Rao, Materials Science Forum **166** (1994) 91.

10. A. Guinier, X-ray Crystallographic Technology, Hilger and Watts Ltd., London (1952) 271.

11. D. Kriegner, Z. Matej, R. Kuzel, V. Holy, J. Appl. Cryst. **48** (2015) 613.

12. K. C. A. Smith, C. W. Oatley, Br. J. Appl. Phys. **6** (1955) 391.

13. A. V. Crewe, M. Isaacson, D. Johnson, Rev. Sci. Instrum. **40** (1969) 241.

14. H Seiler, Journal of Applied Physics **54** (1983) R1.

15. D. W. F. James, R. G. Jones, J. Sci. Instrum. **42** (1965) 283.

16. L. B. Lugansky, V. I. Tsebro, Instruments and Experimental Techniques **58** (2015) 118.

17. A. Arsenault, B. Charpentier-Pépin, A. Forcier, N. Nassiri, J. Bellemare, C. Lacroix, D. Ménard, F. Sirois, F. Bernier, J.-M. Lamarre, Rev. Sci. Instrum. **94** (2023) 085116.

18. J. A. Gerber, W. L. Burmester, D. J. Sellmyer, Rev. Sci. Instrum. **53** (1982) 691.

Chapter 3

Critical current density in granular $REBa_2Cu_3O_{7-\delta}$ superconductors with different interlayer magnetic coupling

3.1 Introduction

Critical current density (J_c) in a high-temperature superconductor (HTS) is known to be very high because of the strong intrinsic pinning potential [1]. Current-voltage (IV) method is known to be very useful in the determination of J_c in HTS [2, 3]. Variation of J_c as a function of temperature (T) and magnetic field (H) in $YBa_2Cu_3O_{7-\delta}$ (YBCO) has been investigated by using several experimental methods [4]. Increasing J_c in bulk samples by intrinsic pinning is an important aspect in current HTS research. Pinning of vortices by point disorder and correlated disorder is a complex process and it depends on the size, nature, and location of the pinning sites [5]. In HTS the position of the rare earth (RE) atoms is very crucial because it is sandwiched between two superconducting planes and contributes to the charge reservoir. Even

though replacing Y in YBCO superconductor by Gd, Nd and Eu affects the superconducting transition temperature, T_c (R = 0) by $\sim$ 2.2 K and the mid-point transition temperature, T_{cm} by $\sim$ 1.9 K, other lanthanides change both transition temperatures (T_c (R = 0) and T_{cm}) differently [6]. Replacing Y by Ho changes in T_{cm} is observed to be $\sim$ 0.8 K whereas the change in the width of the phase transition is $\sim$ 0.5 K [7]. However, the phase transition regions which are generally defined as the difference between the onset transition temperature, T_c and T_c ($\rho \sim 0$) in different RE-based HTS are strongly affected. It is highly possible that any form of disorder and localized magnetic moment originating around the RE site may affect the overall transport properties such as the transport critical current density [8]. Even though there are several studies to understand the role of RE in the phase transitions in HTS, it is really challenging to understand how RE affects transport critical current density.

Four different rare earths (RE $\equiv$ R) have been used to change the magnetic coupling between two superconducting planes of $REBa_2Cu_3O_{7-\delta}$ (RBCO). We have studied granularity and transport properties of (i) $YBa_2Cu_3O_{7-\delta}$ (YBCO), (ii) $GdBa_2Cu_3O_{7-\delta}$ (GBCO), (iii) $NdBa_2Cu_3O_{7-\delta}$ (NBCO) and (iv) $EuBa_2Cu_3O_{7-\delta}$ (EBCO) superconductors. Linear IV characteristics below the onset critical temperature, T_c, have been used to extract (i) intra granular critical current density, J_{cG} and (ii) total critical current density, J_c. The possibility of the δl-pinning in the RBCO superconductor has been explored [9]. Roles of (i) magnetic moment and (ii) granularity in controlling critical current densities have been studied. Exponents revealing the nature of the pinning in two different ranges of T have been extracted for both

$J_{cG}(T)$ and $J_c(T)$. We have proposed that effective Bohr magneton (p_{RE}) and hence the intrinsic magnetic moment corresponding to the RE ions and exponents corresponding to vortex pinning are related even in the presence of the pinning by grain boundaries.

3.2 Experimental

Synthesis of $REBa_2Cu_3O_{7-\delta}$ (RBCO) with RE = Y, Gd, Nd, and Eu samples has been done by using the standard solid-state reaction method **[10 - 12]**. The repeated grinding followed by three sintering is carried out in the range between 925 °C - 930 °C. All four samples in the form of pellets are sintered together in three intermediate steps. Annealing of all samples had been carried out simultaneously at 450 °C for 72 hours using a uniform flow rate of oxygen. Scanning electron microscopy (SEM) is carried out for the determination of the granularity of all four samples. Bar-shaped samples have been cut from pellets and used for the transport measurements of all four HTS. Typical dimensions of the measured bars are $\sim$ 6.4 mm$\times$2.6 mm$\times$0.70 mm. Resistivity as a function of temperature is measured by using the standard four-probe method with the help of a cryogenerator (Janis, USA) **[13, 14]**. At several constant temperatures, IV measurements have been carried below T_c. The range of the current used for IV measurements is 100.0 nA through 5.0 mA **[15]**.

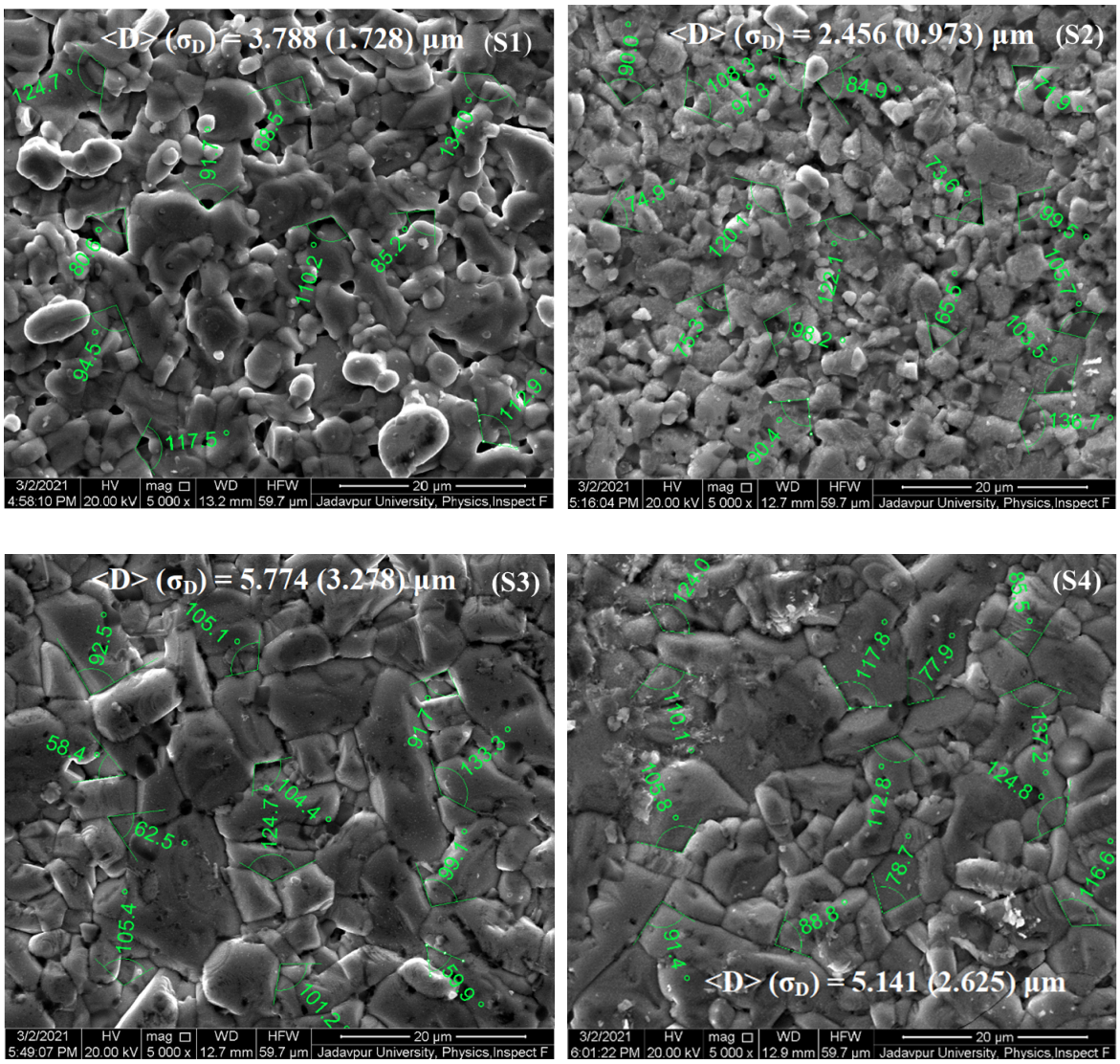

Figure 3.3.1: Scanning electron micrographs (SEM) of (i) $YBa_2Cu_3O_{7-\delta}$ (**S1**), (ii) $GdBa_2Cu_3O_{7-\delta}$ (**S2**), (iii) $NdBa_2Cu_3O_{7-\delta}$ (**S3**) and (iv) $EuBa_2Cu_3O_{7-\delta}$ (**S4**) superconductors.

3.3 Results and Discussions

Firstly, we have shown four representative scanning electron micrographs (SEM) of YBCO, GBCO, NBCO and EBCO in **Figure 3.3.1**. There are almost similar distributions of sizes of grains in all four samples with Y, Gd, Nd and Eu. The minimum and the maximum sizes of the grains are found to be 1.0 μm and 22.0 μm respectively **[16]**. Using ImageJ, we obtained

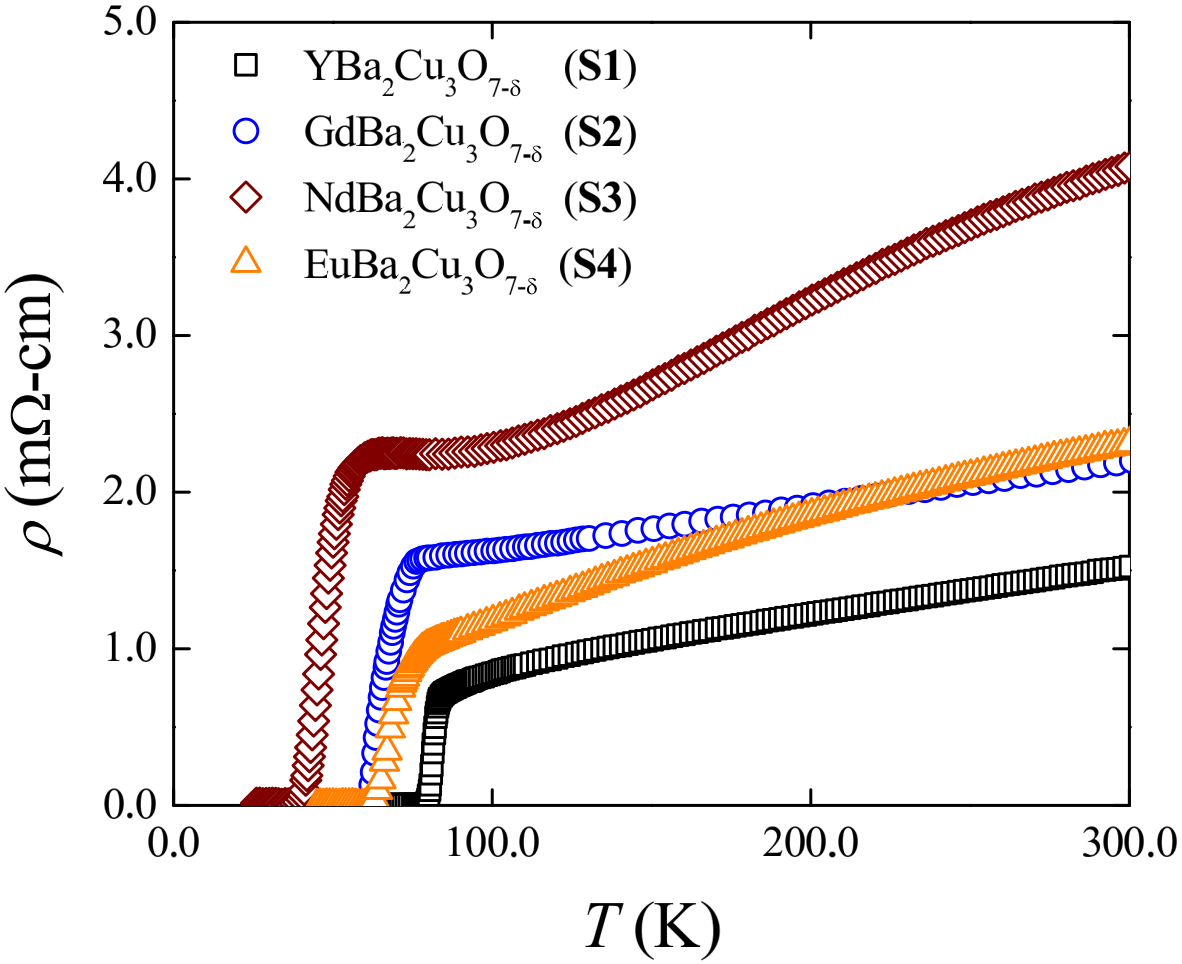

Figure 3.3.2: Resistivity as a function of T of (i) $YBa_2Cu_3O_{7-\delta}$ (**S1**), (ii) $GdBa_2Cu_3O_{7-\delta}$ (**S2**), (iii) $NdBa_2Cu_3O_{7-\delta}$ (**S3**) and (iv) $EuBa_2Cu_3O_{7-\delta}$ (**S4**) superconductors.

average grain sizes to be (i) 3.8 $\pm$ 1.73 μm, (ii) 2.5 $\pm$ 0.97 μm, (iii) 5.8 $\pm$ 3.28 μm and (iv) 5.1 $\pm$ 2.63 μm for YBCO, GBCO, NBCO and EBCO respectively. Clearly, even on changing the rare earth the nature of the granularity remains almost the same. The intergranular networks, randomness of the grain boundaries and the distribution of angles between grain boundaries also remain almost unchanged as revealed in the micrographs. Controlling total critical current density, J_c, by grain boundary in bulk HTS is known to be very effective in several superconductors [17].

We have shown resistivity (ρ) as a function of T in **Figure 3.3.2**. Clearly,

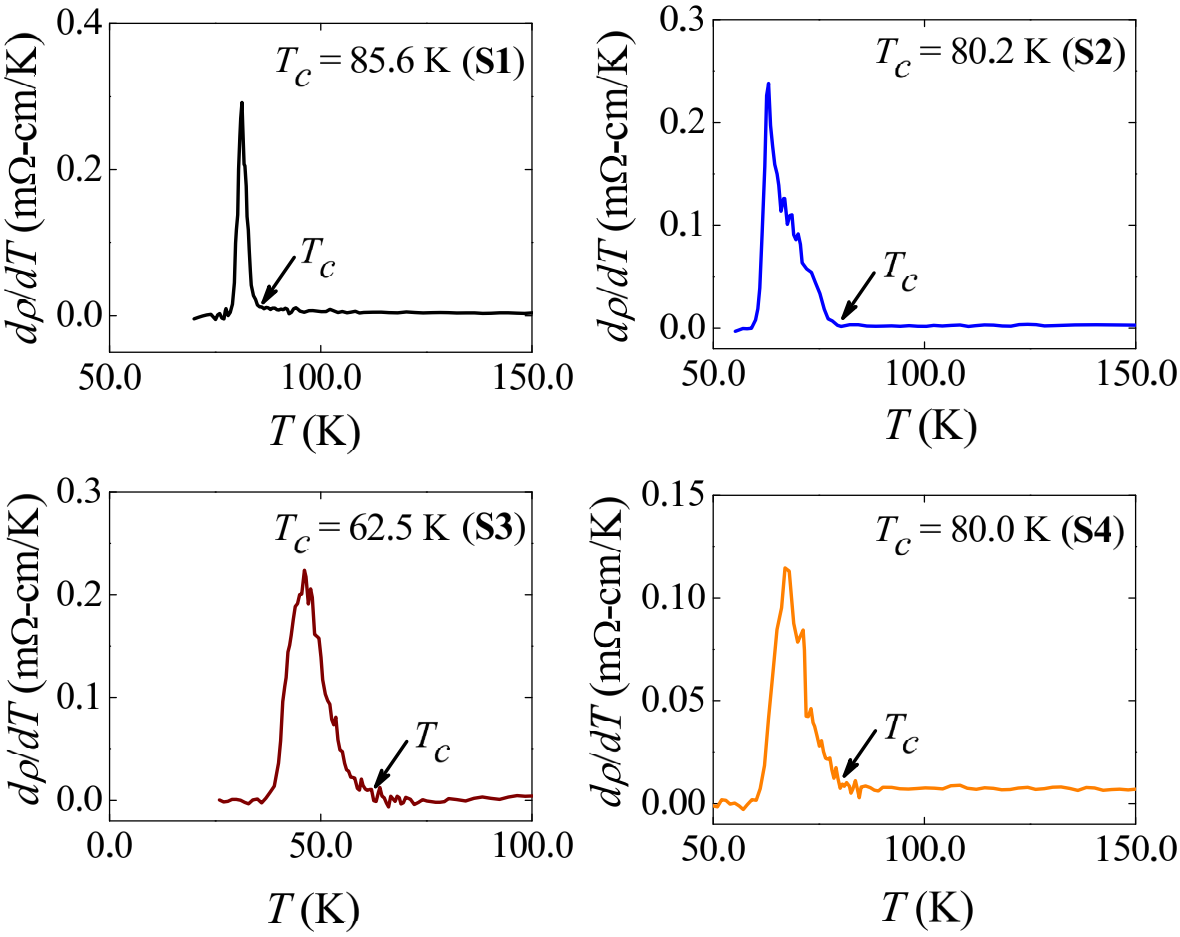

Figure 3.3.3: Variation of $d\rho/dT$ as a function of T of (i) $YBa_2Cu_3O_{7-\delta}$ (**S1**), (ii) $GdBa_2Cu_3O_{7-\delta}$ (**S2**), (iii) $NdBa_2Cu_3O_{7-\delta}$ (**S3**) and (iv) $EuBa_2Cu_3O_{7-\delta}$ (**S4**) superconductors. Critical temperatures are shown by an arrow

the normal state of the NBCO superconductor is found to be the most resistive sample whereas YBCO has the lowest resistivity at 300.0 K. YBCO and GBCO exhibit linear ρ (T) whereas the normal states of both NBCO and EBCO have a curvature in ρ (T). Therefore, depending on the RE, the normal state may have both (i) electron-phonon and (ii) weak electron-electron scattering [18].

In **Figure 3.3.3**, we have shown $d\rho/dT$ as a function of T. By using $d\rho/dT$ we have obtained the onset of the superconducting transition, T_c which is earmarked in **Figure 3.3.3**. Critical temperatures (T_c) are found to be

85.6 K, 80.2 K, 62.5 K and 80.0 K corresponding to YBCO, GBCO, NBCO and EBCO respectively. The change in the onset transition temperature with the rare earth is clearly visible. The lowest T_c is observed for superconductors with RE $\equiv$ Nd separating two superconducting CuO_2 layers. Other than the ionic radius of Y and Nd ions, the magnetic moments contributed by these ions are different which may be one of the major responsible factors for such differences in T_c. We have also extracted T_c ($\rho \sim 0$) which are found to be 78.0 K, 59.0 K, 36.4 K and 58.4 K corresponding to YBCO, GBCO, NBCO and EBCO respectively. Therefore, the phase transition widths [$T_c - T_c$ ($\rho \sim 0$)] are 7.6 K, 21.2 K, 26.1 K, 21.6 K for YBCO, GBCO, NBCO and EBCO respectively. We have used a similar sintering route, repeated mixing and grinding, and a longer duration of annealing process to optimize the effect of granularity and excess oxygen content to avoid non-optimal doping. It clearly reveals that the effects of rare earths, Y, Gd, Nd and Eu on the phase transition regions are strong but different.

It is important to understand how randomness of the granularity affects intergranular weak link resistivity (ρ_{wl}) in several R-123 superconductors. Following a model based on individual grains of the oblate ellipsoid shape, it has been suggested that the measured resistivity (ρ) of polycrystalline sample is related to ρ_{wl} by a structural prefactor involving α_n as follows, $\rho = \frac{1}{\alpha_n}(\rho_{ab} + \rho_{wl})$ **[19]**. An approximate determination of ρ_{wl} can be done by $\rho_{wl} = \alpha_n\, \rho$ (0) where ρ (0) is the zero temperature resistivity obtained by fitting the linear normal state ρ (T). $\alpha_n = (d\rho_{ab}/dT)/(d\rho/dT)$ is the ratio of two slopes corresponding to the single crystal and bulk superconductor in the normal state. A major problem of the rough determination of ρ_{wl} is that we need (i) $d\rho_{ab}/dT$

of the corresponding single crystal (individual grain) and (ii) linear normal state of the bulk sample. Even though we have a linear normal state $\rho(T)$ for YBCO and GBCO, the normal states of NBCO and EBCO are nonlinear over a wide range of T. Moreover, $d\rho_{ab}/dT$ of individual single crystal of present HTS samples with Y, Eu, Nd and Gd is unknown. Assuming (i) $d\rho_{ab}/dT$ $\sim 0.5\ \mu\Omega$-cmK^{-1} of YBCO single crystal [19] for all other samples and (ii) linear normal states we roughly obtain $\alpha_n \sim 0.1$ - 0.2 for YBCO, EBCO, NBCO and GBCO respectively. By this approximate method, ρ_{wl} is found to be $\sim 60 - 240\ \mu\Omega$-cm for all four samples. However, (i) an assumption of oblate ellipsoid grain shapes for our samples and (ii) the same $d\rho_{ab}/dT$ for all individual grains of four samples are not very realistic. Because of the difficulty and assumptions used in the extraction method of ρ_{wl} for our samples, we have focused on the randomness as revealed in the relative orientations of grains of all four samples as shown in **Figure 3.3.1** are almost similar and is most important in effective pinning mechanism (by randomly oriented grain boundary). Therefore, it is not unreasonable to say that the effect of the granularity on the overall intergranular transport properties will be almost similar. Any change in the resistivity, critical current density and other transport parameters of these four superconductors results mostly because of the changes in the rare earths separating the CuO_2 planes.

In **Figure 3.3.4 - Figure 3.3.7** we have shown IV characteristics at several T for YBCO, GBCO, NBCO and EBCO samples. Electric field (E) and current density (J) corresponding to V and I respectively are also shown for each sample [20]. In **Figure 3.3.4**, we have shown IV in the range of T = 86.0 K through 81.0 K for the YBCO superconductor. In the inset of **Figure**

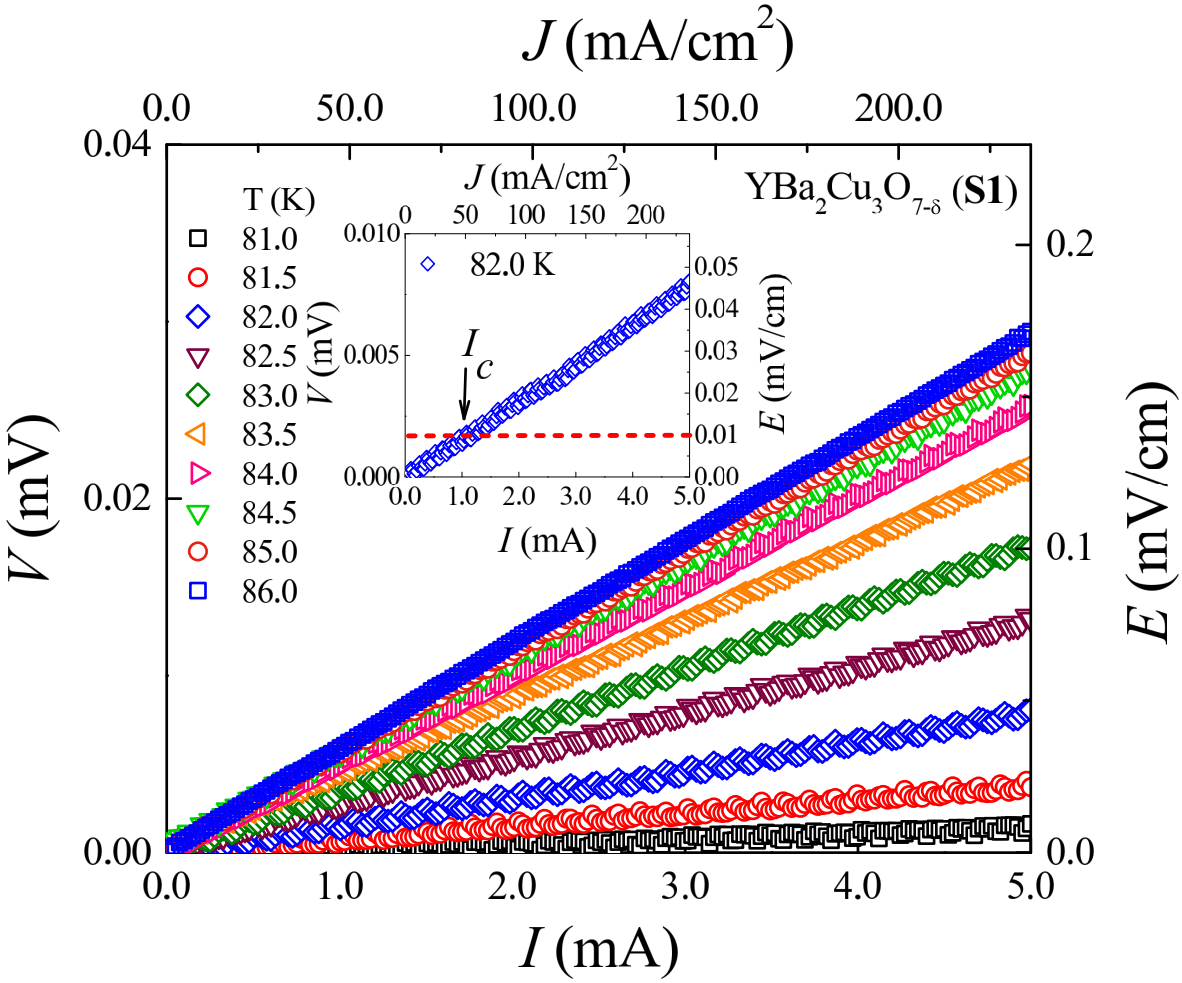

Figure 3.3.4: Current-voltage (IV) characteristics of sample $YBa_2Cu_3O_{7-\delta}$ (**S1**). In the inset, we have shown a representative linear IV together with the extraction criterion.

3.3.4 a representative IV measured at 82.0 K is shown which is found to be linear. In **Figure 3.3.5**, IV characteristics in the range of 80.0 K - 61.6 K corresponding to the GBCO sample are shown. In the inset of **Figure 3.3.5**, a linear IV curve at T = 63.0 K is shown. In **Figure 3.3.6**, in the range of 62.0 K – 37.0 K, we have shown IV curves of the NBCO sample including an inset showing a linear IV at 39.0 K. We have also shown IV characteristics of the EBCO superconductor in the range of 80.0 K - 63.0 K in **Figure 3.3.7** and an inset of it shows the IV curve at 65.0 K. Therefore, below T_c of the corresponding samples, IV curves are found to be linear in a reduced

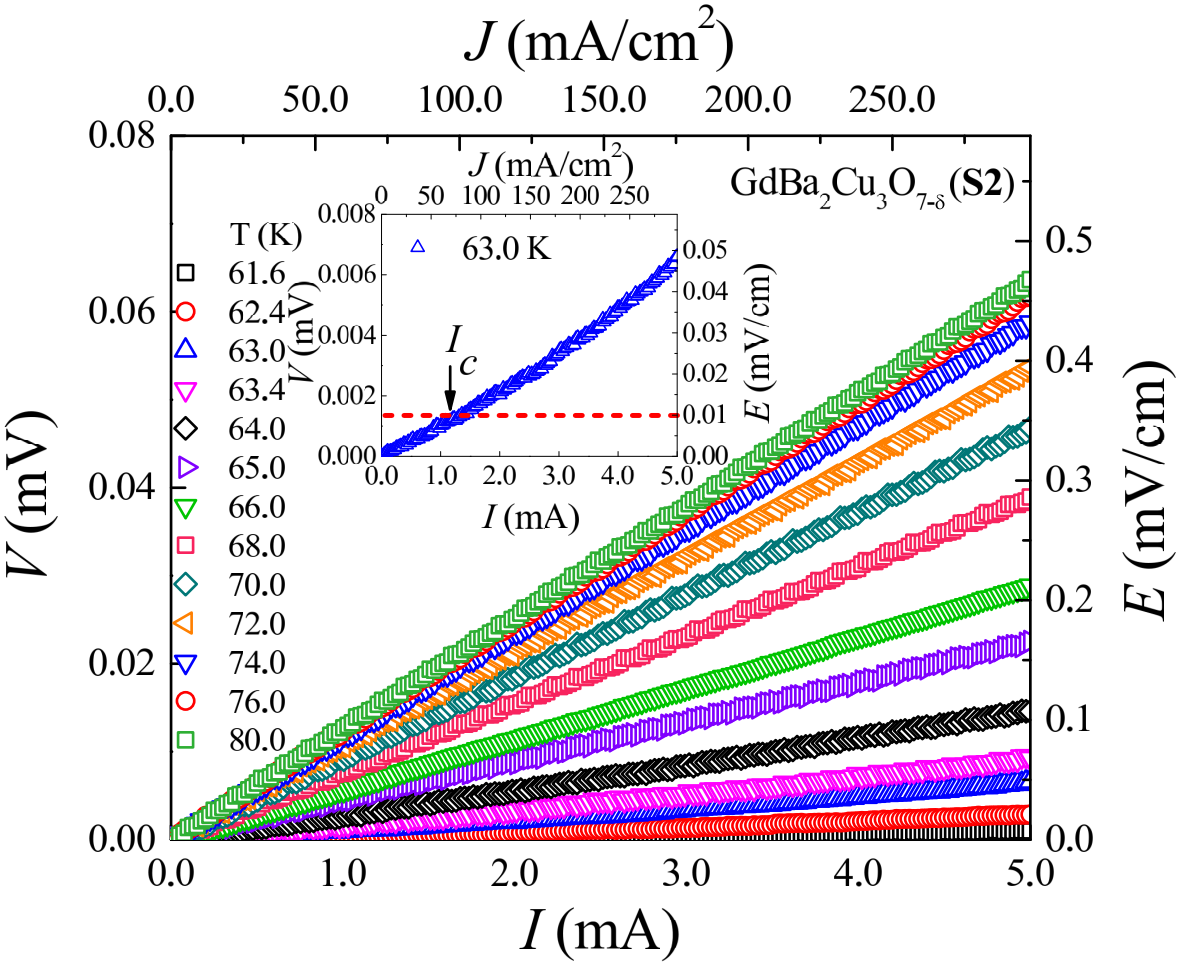

Figure 3.3.5: Current-voltage (IV) characteristics of sample $GdBa_2Cu_3O_{7-\delta}$ (**S2**). In the inset, we have shown a representative linear IV together with the extraction criterion.

temperature, $\varepsilon = T/T_c \geq 0.65$. Both the linear and nonlinear natures of IV below T_c are observed in several superconductors [21, 22]. The determination process of J_c is possible by using IV curves and it is independent of the nature of IV. However, a suitable criterion is known to be a very crucial one in the extraction of J_c [23]. We have used an electric field criterion $E = 0.01$ mV/cm and in the inset of each IV graph, the extraction criterion is shown.

We have extracted two different critical current densities (i) J_{cG} and (ii) J_c using an average granular area and total area of cross-section of the related samples respectively in the same electric field criterion [20, 24]. In **Figure**

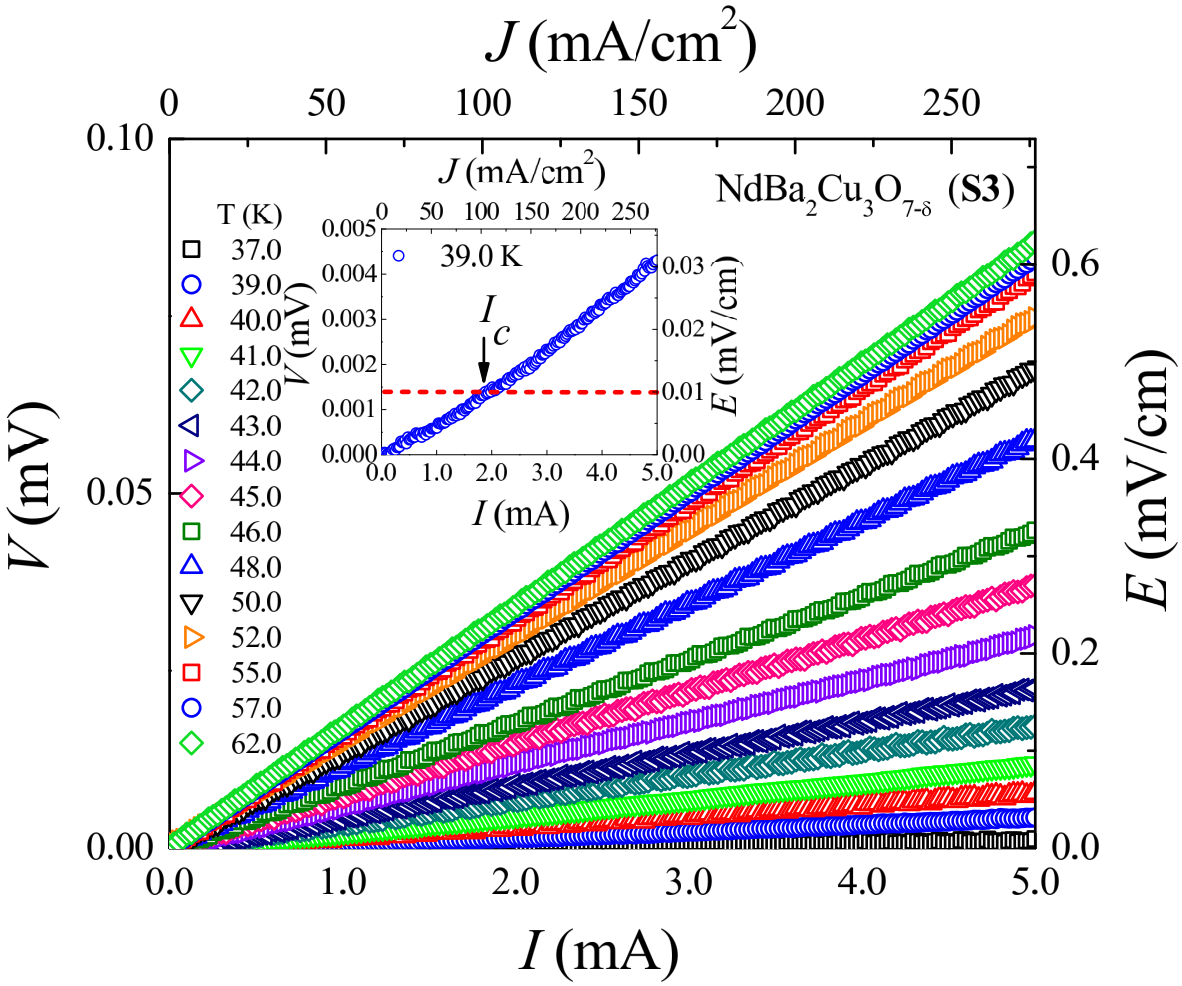

Figure 3.3.6: Current-voltage (IV) characteristics of sample $NdBa_2Cu_3O_{7-\delta}$ (**S3**). In the inset, we have shown a representative linear IV together with the extraction criterion.

3.3.8 we have plotted J_{cG} as a function of T for all four samples. The upward curvature of $J_{cG}(T)$ remains almost unchanged in superconductors having different RE. $J_{cG}(T)$ of GBCO exhibits the maximum $J_{cG} \sim 7{\times}10^7$ mA/cm^2. The maximum J_{cG}s are found to be almost the same in NBCO and EBCO which is $\sim 1.5 \times 10^7$ mA/cm^2. In addition the maximum $J_{cG} \sim 2 \times 10^7$ mA/cm^2 observed in the YBCO is almost comparable with the maximum J_{cG} of the NBCO and EBCO close to the respective T_c ($\rho \sim 0$). Because J_{cG} is mostly confined within the grains, the pinning strength in RBCO is expected to be changed with the intrinsic moment of RE.

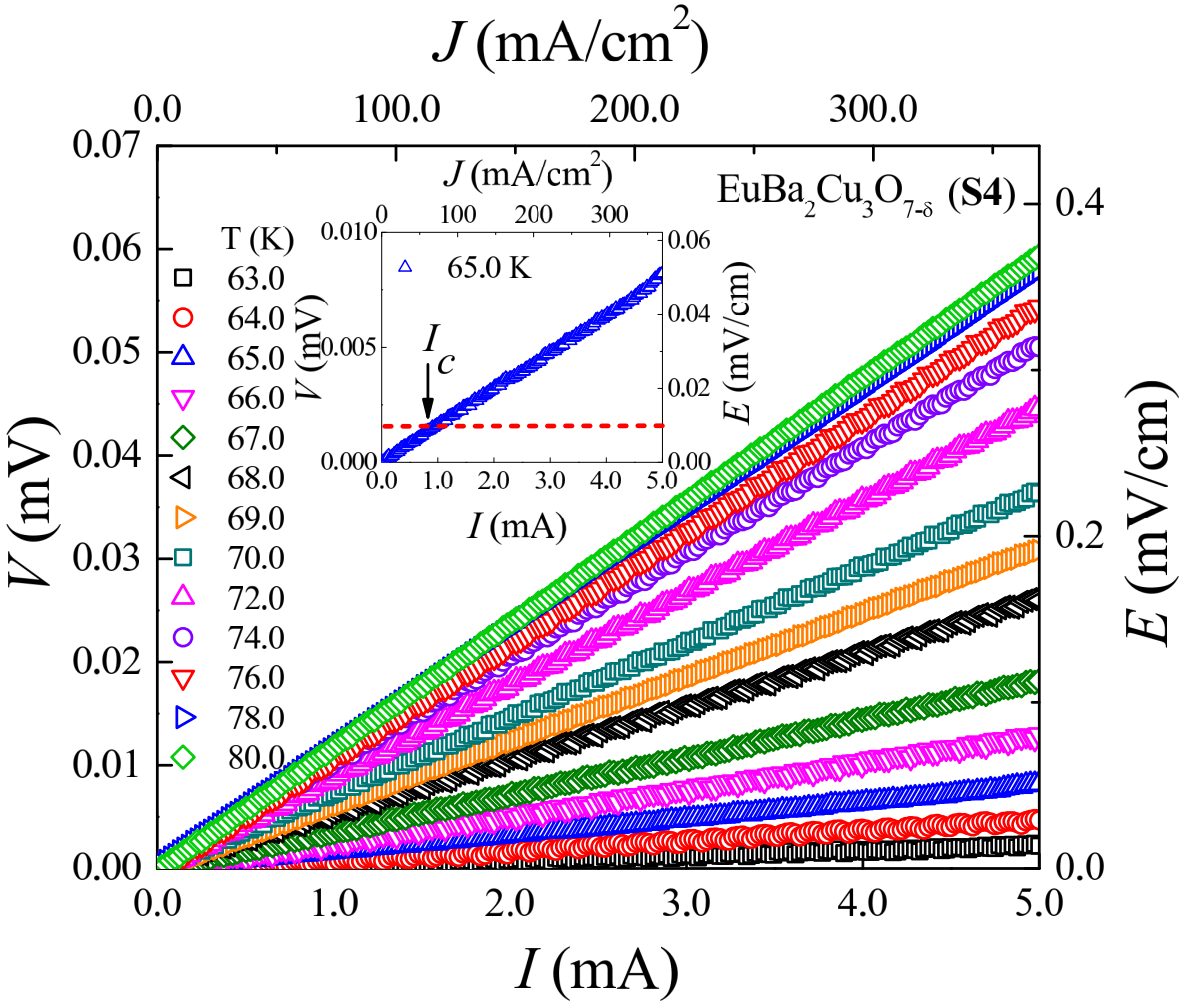

Figure 3.3.7: Current-voltage (IV) characteristics of sample $EuBa_2Cu_3O_{7-\delta}$ (**S4**) superconductors. In the inset, we have shown a representative linear IV together with the extraction criterion.

To determine the nature of the pinning within a grain we have plotted the J_{cG} with (1 - ε^2) in log-log scale in the inset of **Figure 3.3.8** [25]. It reveals that there are at least two linear regions with different slopes. These slopes may be used for the possible changes in the nature of the pinning. An equation for the critical current density is expressed as $J_{cG} \propto (1 - \varepsilon^2)^n$ in which n is known to be an exponent revealing the nature of the pinning [25]. Assuming a linear variation in the lower (1 - ε^2) region an exponent, $n^{HT}_{J_{cG}}$, has been extracted which reveals the nature of the pinning of vortices at higher T -region. We have obtained that $n^{HT}_{J_{cG}}$ = 0.29 $\pm$ 0.09, 0.31 $\pm$ 0.11, 0.13 $\pm$

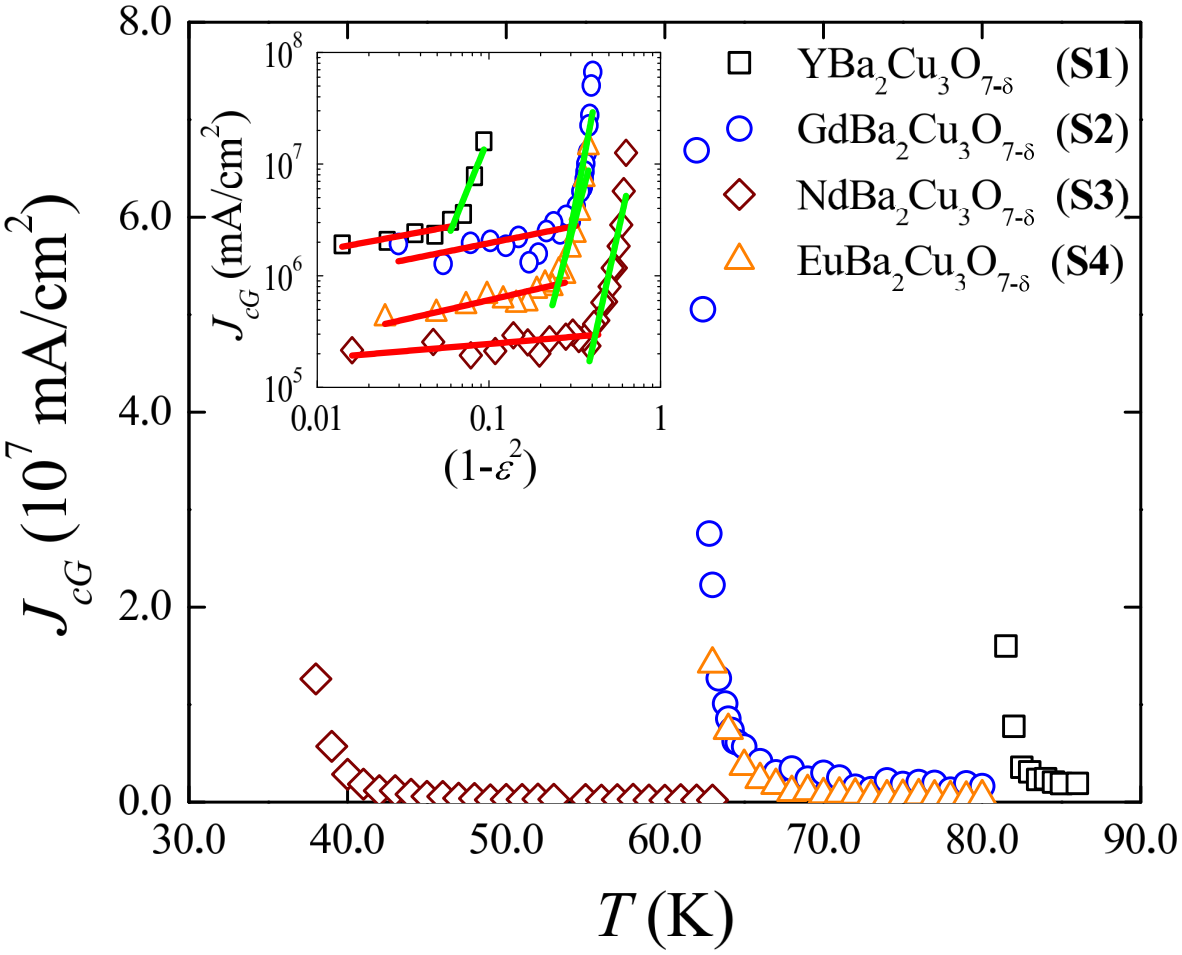

Figure 3.3.8: Critical current density (J_{cG}) as a function of T for all samples. In the inset, we have plotted J_{cG} as a function of (1-ε^2) in the log-log scale. Fitting lines are shown for extracted exponent, $n^{HT}_{J_{cG}}$ and $n^{LT}_{J_{cG}}$.

0.05 and 0.35 $\pm$ 0.06 corresponding to YBCO, GBCO, NBCO and EBCO respectively. A linear variation is also observed at the lower T and hence higher (1 - ε^2) region as shown in the inset of **Figure 3.3.8**. An exponent, $n^{LT}_{J_{cG}}$, is extracted to understand the pinning for the low-T region. It is observed that $n^{LT}_{J_{cG}}$ = 3.75 $\pm$ 0.87, 8.19 $\pm$ 0.14, 6.93 $\pm$ 0.79 and 5.76 $\pm$ 0.78 corresponding to YBCO, GBCO, NBCO and EBCO respectively. Even though $n^{HT}_{J_{cG}} << n^{LT}_{J_{cG}}$ there is a weak variation of both exponents $n^{HT}_{J_{cG}}$ and $n^{LT}_{J_{cG}}$. It also reveals that there may be a region in which the δl-pinning is the most possible description of the pinning corresponding to an exponent of 1.2. However, deviations from

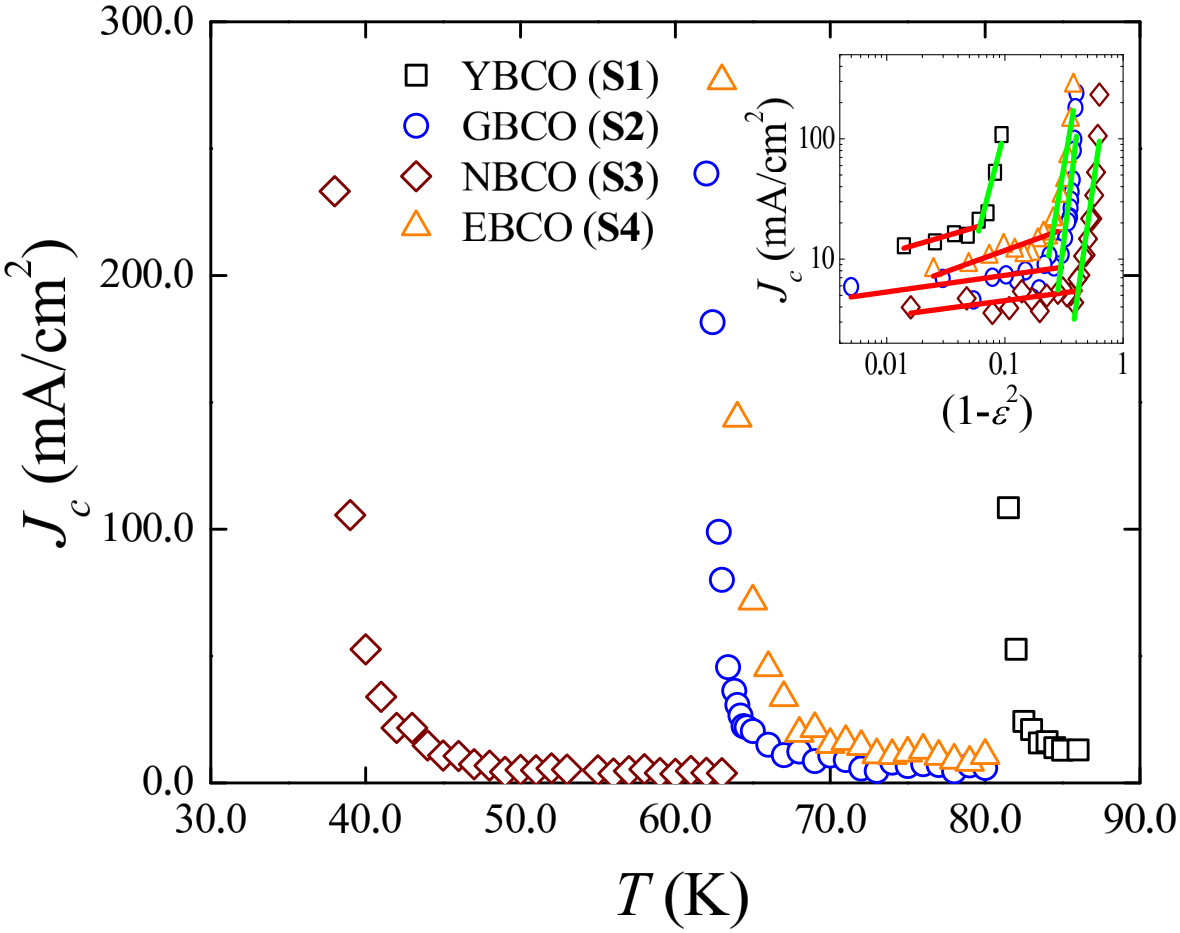

Figure 3.3.9: Critical current density (J_c) as a function of T for all samples. In the inset, we have plotted J_c as a function of (1-ε^2) in log-log scale. Fitting lines are also shown for extracted exponent, $n_{J_c}^{HT}$ and $n_{J_c}^{LT}$.

the nature of the δl-pinning are observed with T.

In **Figure 3.3.9**, we have shown J_c as a function of T. In comparison to the J_{cG}, J_c is found to be much lower because of the presence of the grain boundary networks. Determination of the J_c involves the total area of cross section of the bar-shaped samples which are of the order of a few mm^2. Following SEM as shown in **Figure 3.3.1**, it is observed that angles between two grains marked for all samples exhibit a distribution of angles including very higher angles. Lower J_c may be mostly a result of the presence and the distribution of grain angles **[1]**. However, because of the randomness of the grain boundary in all four samples, the reduction is almost similar in magnitude.

Variation of J_c in four samples is mostly a result of the different interlayer magnetic coupling for the different localized magnetic moments of the rare earth ions. In the inset of **Figure 3.3.9**, we have also shown the variation of J_c as a function of (1 - ε^2) to understand the nature of the pinning. Two different regions exhibit that slopes of the variations are highly different which are quantified by two exponents, $n_{J_c}^{HT}$ and $n_{J_c}^{LT}$. We have obtained $n_{J_c}^{HT}$ = 0.29 $\pm$ 0.09, 0.14 $\pm$ 0.07, 0.13 $\pm$ 0.05, 0.35 $\pm$ 0.06 corresponding to YBCO, GBCO, NBCO and EBCO respectively. Therefore, the extracted pinning exponents, $n_{J_c}^{HT}$ vary weakly with (i) Y, (ii) Gd, (iii) Nd and (iv) Eu. However, the exponent $n_{J_c}^{LT}$ corresponding to the low-T region varies strongly with RE. Extracted $n_{J_c}^{LT}$ are found to be 3.75 $\pm$ 0.87, 8.19 $\pm$ 0.14, 6.93 $\pm$ 0.79 and 5.76 $\pm$ 0.78 corresponding to YBCO, GBCO, NBCO and EBCO respectively revealing strong dependence of exponents on the rare earth.

We propose that the intrinsic magnetic moment originated in the RE sites has an influence on the pinning of vortices and hence on the critical current density in addition to other physical properties **[26, 27]**. In **Figure 3.3.10**, we have plotted pinning exponents, $n_{J_{cG}}^{HT}$ and $n_{J_c}^{HT}$ with p_{RE}, effective Bohr magneton representing localized magnetic moment contributed by four rare earths. It reveals that there is a weak dependence of both exponents ($n_{J_{cG}}^{HT}$ and $n_{J_c}^{HT}$) on p_{RE}. Since the effect of the intrinsic moment of rare earth ions in the high-T region ($T < T_c$) is weak both J_c and J_{cG} are weakly controlled by p_{RE}. However, as the T is further lowered, the effect of the intrinsic moment becomes visible **[28]**. In **Figure 3.3.11**, we have shown pinning exponents, $n_{J_{cG}}^{LT}$ and $n_{J_c}^{LT}$ with p_{RE} for the low-T region ($T < T_c$). Clearly a linear variation of both $n_{J_{cG}}^{LT}$ and $n_{J_c}^{LT}$ with p_{RE} is observed. It reveals that the nature of

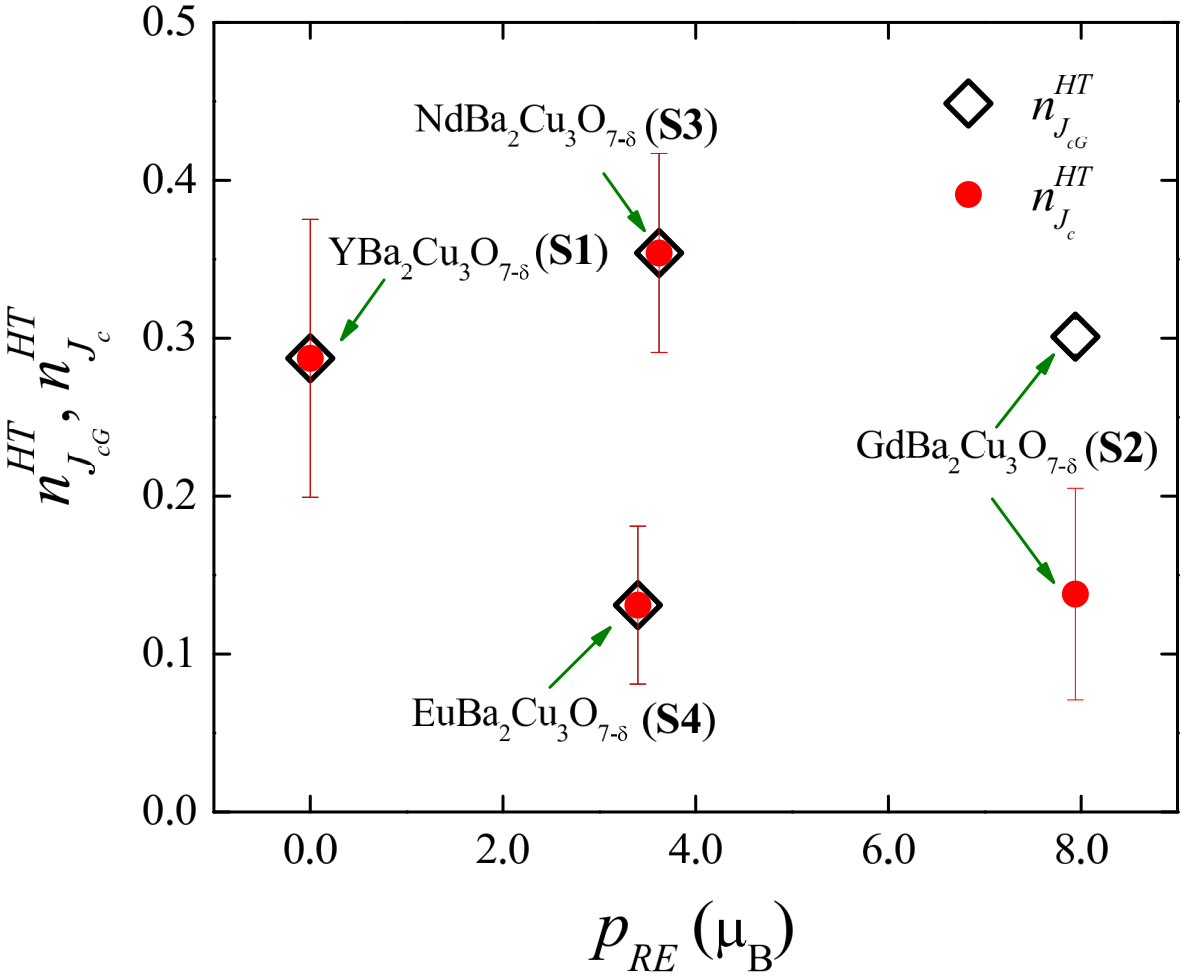

Figure 3.3.10: Variation of the pinning exponents, $n^{HT}_{J_{cG}}$ and $n^{HT}_{J_c}$ with effective Bohr magneton, p_{RE}, which represents the intrinsic magnetic moment of RE ions.

the pinning becomes sensitive to the intrinsic moment at the rare earth sites. Actually, any change in the intrinsic moment in between two superconducting layers of a cuprate superconductor alters the magnetic coupling which in turn may be responsible for enhancing the pinning effect at low-T region [29]. As a result of the enhancement of the pinning by an intrinsic moment both critical current densities gets affected.

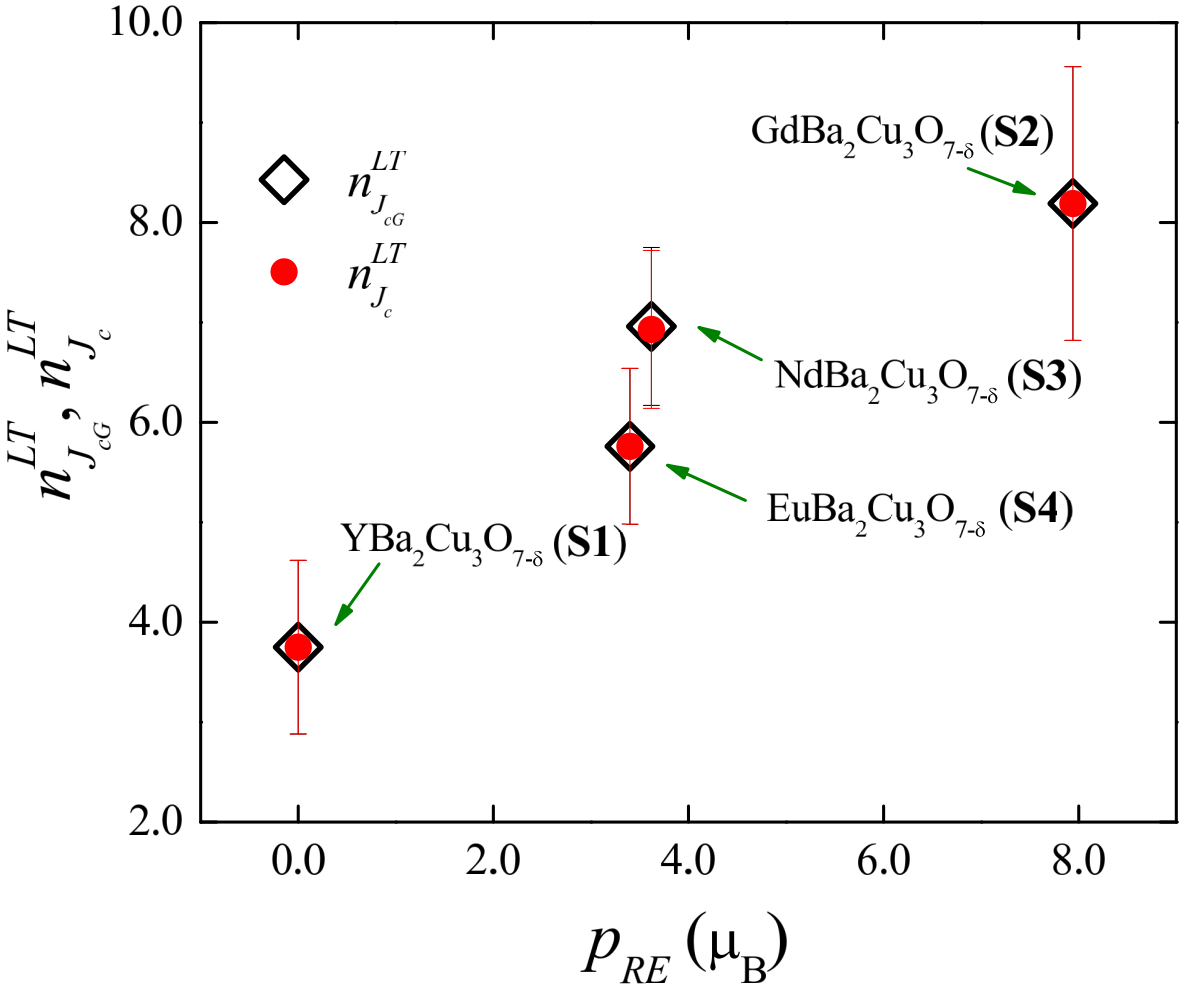

Figure 3.3.11: Variation of the pinning exponents, $n^{LT}_{J_{cG}}$ and $n^{LT}_{J_c}$ with effective Bohr magneton, p_{RE}, which represents the intrinsic magnetic moment of RE ions.

3.4 Summary

Current-voltage (IV) characteristics and micrographs are studied in four bulk RBCO superconductors. We have extracted (i) intra-granular and (ii) total critical current density by using IV characteristics of RBCO superconductors for four different rare earths representing magnetic couplings between superconducting layers. Exponents corresponding to two ranges of temperatures are extracted to understand the nature of pinning by intrinsic magnetic moment. A linear variation of the exponents in the low-T region as a function

of the effective Bohr magneton has been observed for both types of current densities. Intrinsic magnetic moments of rare earths form a magnetic network which controls both the critical current densities in addition to the grain boundary.

3.5 References

1. H. Hilgenkamp, J. Mannhart, Rev. Mod. Phys. **74** (2002) 485.

2. Y. L. Wang, L. R. Thoutam, Z. L. Xiao, B. Shen, J. E. Pearson, R. Divan, L. E. Ocola, G. W. Crabtree, W. K. Kwok, Phys. Rev. B **93** (2016) 045111.

3. D. Larbalestier, A. Gurevich, D. M. fieldmann, A. Polyanskii, Nature **414** (2001) 368.

4. G. Wang, M. J. Raine, D. P. Hampshire, Supercond. Sci. Technol. **31** (2018) 024001.

5. G. Blatter, M. V. Feigel'man, V. B. Geshkenbein, A. I. Larkin, V. M. Vinokur, Rev. Mod. Phys. **66** (1994) 1125.

6. J. M. Tarascon, W. R. McKinnon, L. H. Greene, G. W. Hull, E. M. Vogel, Phys. Rev. B **36** (1987) 226.

7. F. Vidal, J. A. Veira, J. Maza, F. Miguelez, E. Moran, M. A. Alario, Solid State Commun. **66** (1988) 421.

8. V. Rollano, J. del Valle, A. Gomez, M. Velez, L. M. Alvarez-Prado, C. Quiros, J. I. Martin, M. R. Osorio, D. Granados, E. M. Gonzalez, J. L. Vicent, Sci. Rep. **8** (2018) 12374.

9. R. Griessen, Wen Hai-hu, A. J. J. van Dalen, B. Dam, J. Rector, H. G. Schnack, Phys. Rev. Lett. **72** (1994) 1910.

10. S. Mollah, B. Biswas, S. Haldar, A. K. Ghosh, Physica C **539** (2017) 40.

11. S. Haldar, P. Das, A. K. Ghosh, Physica C **563** (2019) 78.

12. I. Mukherjee, A. K. Ghosh, J. Supercond. Nov. Magn. **34** (2021) 365.

13. B. Biswas, A. K. Ghosh, J. Supercond. Nov. Magn. **33** (2020) 2629.

14. P. Das, A. K. Ghosh, Physica C **548** (2018) 27.

15. T. Sk, A. K. Ghosh, AIP Adv. **10** (2020) 065117.

16. G. Wang, M. J. Raine, D. P. Hampshire, Supercond. Sci. Technol. **30** (2017) 104001.

17. D. J. Scalapino, Rev. Mod. Phys. **84** (2012) 1383.

18. N. P. Armitage, P. Fournier, R. L. Greene, Rev. Mod. Phys. **82** (2010) 2421.

19. A. Díaz, J. Maza, Félix Vidal, Phys. Rev. B **55** (1997) 1209.

20. D. Rakshit, T. Sk, P. Das, S. Haldar, A. K. Ghosh, Physica C **588** (2021) 1353909.

21. P. G. Baity, X. Shi, Z. Shi, L. Benfatto, D. Popovic, Phys. Rev. B **93** (2016) 024519.

22. T. Sk, A. K. Ghosh, J. Low Temp. Phys. **198** (2020) 224.

23. A. V. Pan, I. A. Golovchanskiy, S. A. Fedoseev, Europhys. Lett. **103** (2013) 17006.

24. P. Mandal, D. Rakshit, T. Sk, A. K. Ghosh, J. Supercond. Nov. Magn. **35** (2022) 1079.

25. T. Aytug, M. Paranthaman, K. J. Leonard, S. Kang, P. M. Martin, L. Heatherly, A. Goyal, A. O. Ijaduola, J. R. Thompson, D. K. Christen, Phys. Rev. B **74** (2006) 184505.

26. A. Keren, W. Crump, B. P. P. Mallett, S. V. Chong, I. Keren, H. Luetkens, J. L. Tallon, Phys. Rev. B **100** (2019) 144512.

27. A. Llordés, A. Palau, J. Gázquez, M. Coll, R. Vlad, A. Pomar, J. Arbiol, R. Guzmán, S. Ye, V. Rouco, F. Sandiumenge, S. Ricart, T. Puig, M. Varela, D. Chateigner, J. Vanacken, J. Gutiérrez, V. Moshchalkov, G. Deutscher, C. Magen, X. Obradors, Nat. Mater. **11** (2012) 329.

28. J. Felsteiner, Phys. Rev. B **39** (1989) 7248.

29. B. P. P. Mallett, T. Wolf, E. Gilioli, F. Licci, G. V. M. Williams, A. B. Kaiser, N. W. Ashcroft, N. Suresh, J. L. Tallon, Phys. Rev. Lett. **111** (2013) 237001.

Chapter 4

Criteria sensitive analysis of transport critical current density in BZO mixed YBCO

4.1 Introduction

The critical current density, J_c in high-temperature superconductors (HTS) depends not only on the pinning centers strongly but also on the methods of the determination. Critical currents obtained by magnetic measurements and transport measurements are found to be very different in HTS [1]. An electric field (E) criterion is very important to compare critical current density obtained by different methods. Generally, with the help of the current-voltage (IV) characteristics, transport critical current density is determined [2]. The determination of the transport critical current density is very important to establish the correlation between different nature of pinning and J_c. However, it is an extremely complex process to decide a specific criterion on the basis of which the correlation can be decided precisely [1]. There are several criteria

used to determine transport J_c. By changing the criterion, transport J_c and its dependence on T can be highly different in nature and misleading. We have made an attempt to study how different electric field criteria affect the determination of total transport J_c and intra granular transport J_{cG} and its several interpretations.

There are several major aspects of both $J_c(T)$ and $J_{cG}(T)$ related to the role of criterion. Enhancement of the transport J_c by additional pinning is a very important aspect in vortex states. The determination of J_c by a specific criterion is the most crucial one to understand the nature of the pinning. Another observed transition in $J_c(T)$ is known to be the Ambegaokar–Baratoff (AB) to Ginzburg–Landau (GL) transition in HTS **[3 - 5]**. It will be an important investigation to understand how different E-based criteria may change the interpretations of the extracted numbers associated with the change in such transition in $J_c(T)$.

There are a number of studies in which it is observed that J_c in $BaZrO_3$ (BZO) added in YBCO and other superconductors increases **[6, 7]**. Magnetic J_c in BZO doped YBCO is found to be 3.6 x 10^7 A/cm^2 at 5.0 K at very small magnetic field **[8]**. However, it is not clear how zero field transport $J_c(T)$ varies in such composite systems. We have chosen such a composite bulk system consisting of 5.0% BZO and the pure YBCO superconductors. IV characteristics of the sample have been used to extract $J_c(T)$ by using four different criteria based on the electric field, E. The usual behavior of the increasing $J_c(T)$ with decreasing T has been interpreted for several criteria used for the determination. We have also analyzed $J_c(T)$ and $J_{cG}(T)$ within the framework of (i) AB and (ii) GL equations for all criteria. A possible

variation in the coefficients associated with the AB and GL equations has been discussed. The maximum achievable current in such a system and its dependence on different criteria have also been extracted.

4.2 Experimental

We have synthesized BZO added bulk $YBa_2Cu_3O_{7-\delta}$ (YBCO) superconducting samples by using the standard solid-state reaction method. We have added 5.0 weight % $BaZrO_3$ (BZO) before the calcination which is carried out at 850 °C for 24 hours. Pellets are sintered several times at 930 °C with intermediate grindings for a duration of 48 hours. The annealing at 450 °C in flowing oxygen is done for 50 hours [9]. Typical dimensions of the bar-shaped sample used for the transport measurements are $6.0\times2.45\times0.70$ mm^3. The separation between two voltage leads is 1.66 mm. Resistivity as a function of T has been measured by using the standard four-probe method with the help of a close-cycle cryogenerator (Janis, USA). Current-voltage (IV) measurements have been carried out at several temperatures around the phase transition region. The range of the current used for IV measurements is 100.0 nA through 5.0 mA [10].

4.3 Results and Discussions

In **Figure 4.3.1**, we have shown resistivity (ρ) as a function of T of the BZO added $YBa_2Cu_3O_{7-\delta}$ (**S5**) superconductor. In the inset of **Figure 4.3.1**, we have shown $d\rho/dT(T)$. The onset critical temperature, T_c is found to be 87.0

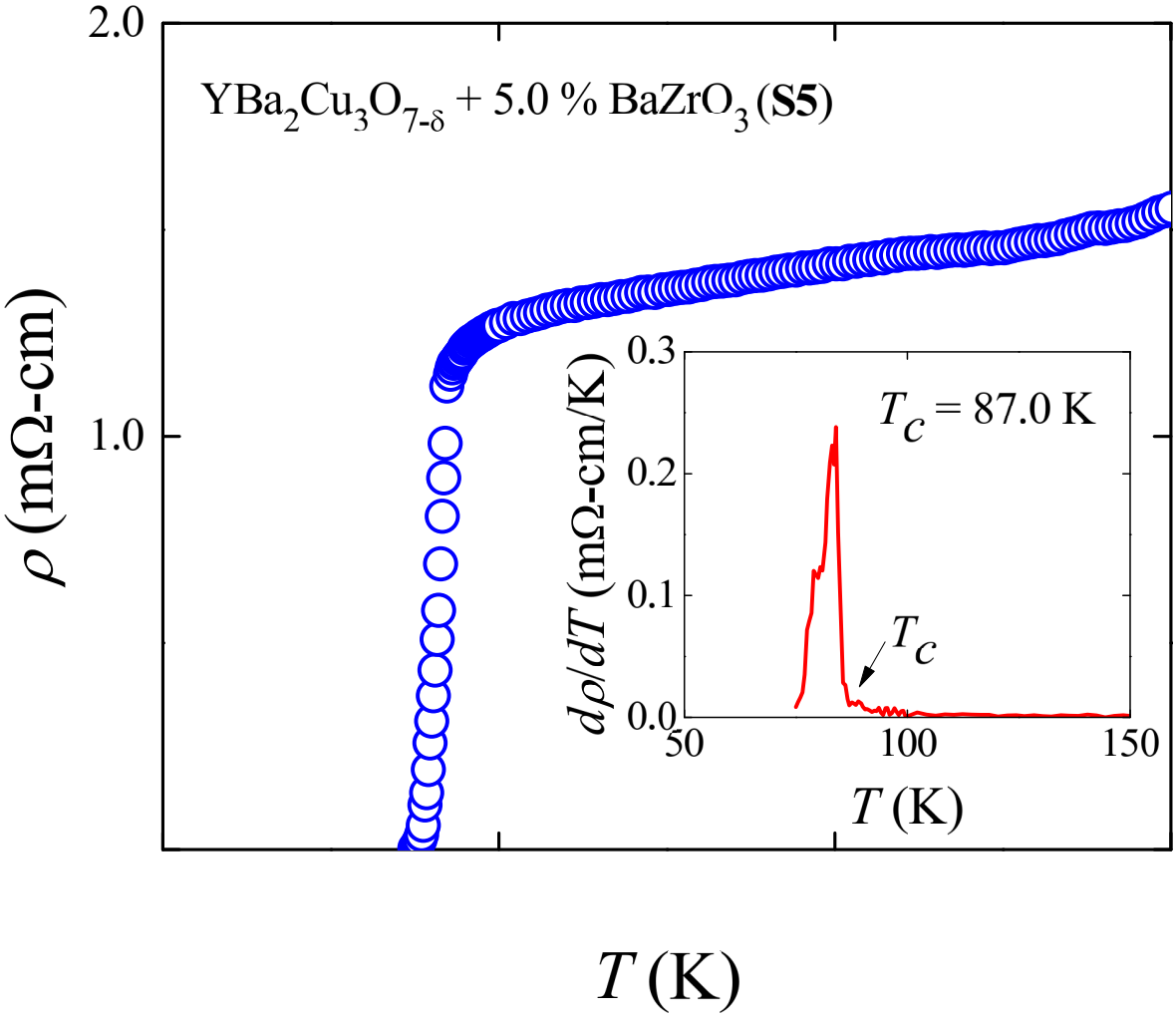

Figure 4.3.1: Resistivity as a function of T in BZO added YBCO. $d\rho/dT$ versus T is shown in the inset. Onset critical temperature T_c is indicated.

K which is also shown in the inset of **Figure 4.3.1**. Below 87.0 K, the resistivity decreases with decreasing T which is known to be the transition region at zero magnetic field. Within the transition width (T < 87.0 K) the current-voltage (IV) characteristics can be used successfully to extract J_c and its dependence on T **[11, 12]**. Even though $J_c(T = T_c)$ should be zero theoretically, it is well known that several criteria are used for the determination of $J_c(T)$. We have focused on how the choices of criteria affect the determination of $J_c(T)$ by using IV characteristics below T = 87.0 K.

We have shown IV characteristics below T_c in **Figure 4.3.2**. The variation

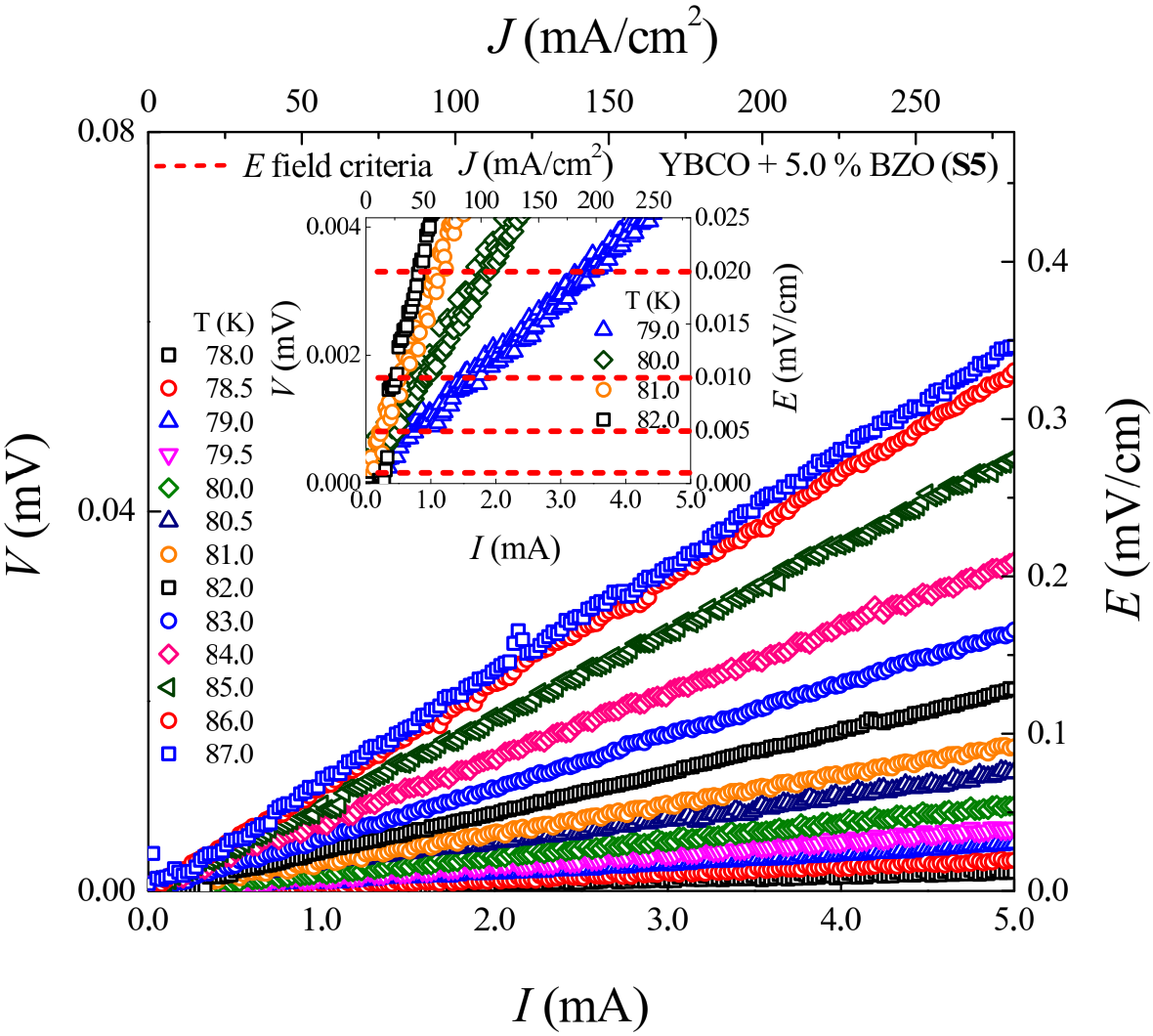

Figure 4.3.2: Current-voltage (IV) characteristics below T_c. In the inset dashed lines corresponding to the criteria of the determination of J_c has been shown as representatives.

of the electric field, E, as a function of the current density, J, has also been shown in **Figure 4.3.2**. Linear IV characteristics are observed in the range of 87.0 – 78.0 K. In the inset of **Figure 4.3.2**, we have shown four linear IV curves around the lowest T. The current density J shown in **Figure 4.3.2** is obtained by the applied current (I) divided by the area $\sim$1.79 mm^2 of the bar-shaped sample. Therefore, J is the total current density which is contributed by individual grains as well as the grain boundaries **[13]**. For $T < T_c = 87.0$ K, the grains are mostly superconducting and therefore J_c is considered as

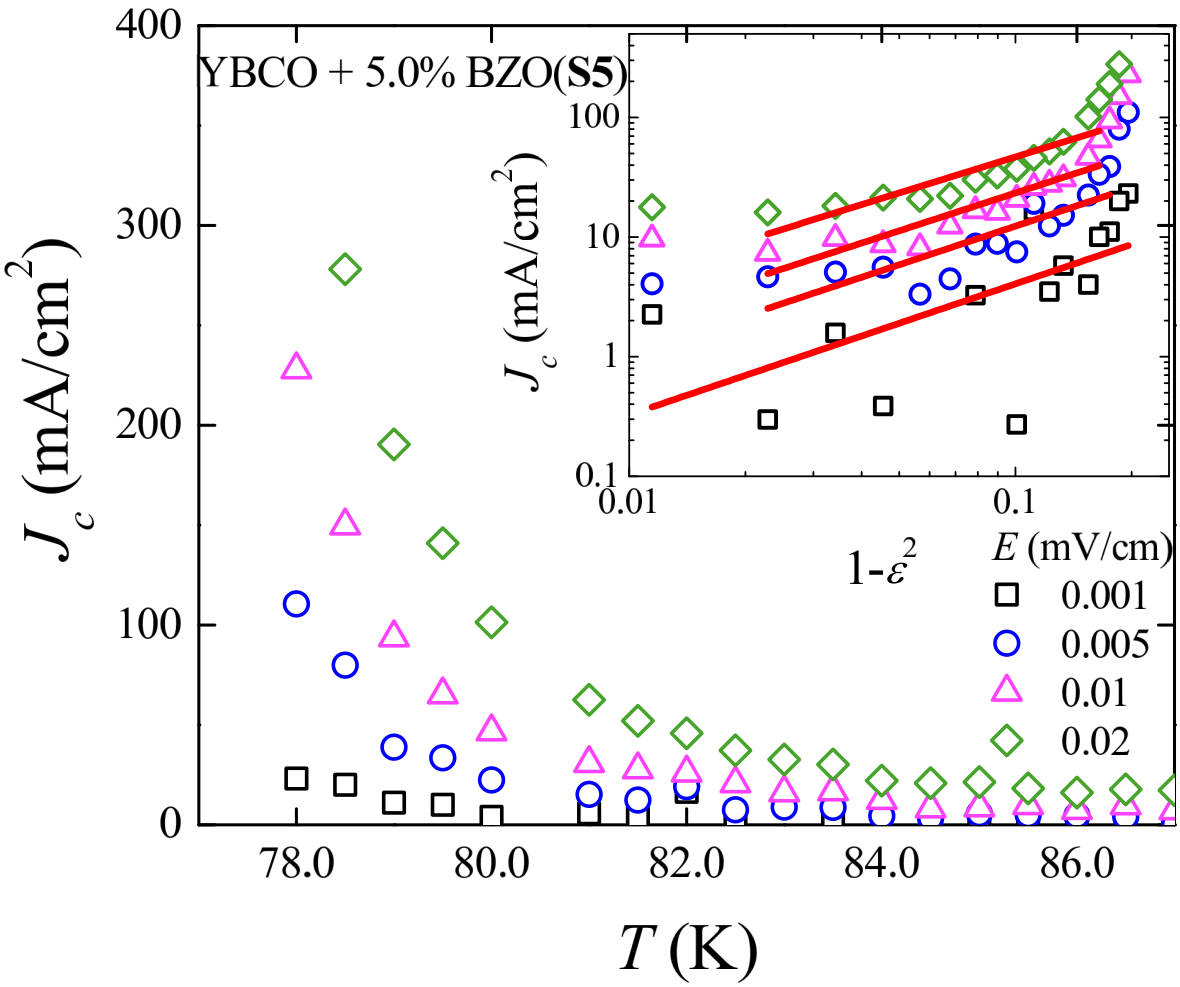

Figure 4.3.3: Critical current density of BZO added YBCO as a function of T for several electric field criteria. In the inset the variation of J_c with [1 - $(T/T_c)^2$] for four E-based criteria

the total critical current density. The determination of the critical current density from the $J(E)$ curves are usually done by using a suitable E-based criterion. However, finding a suitable criterion is really a challenging one for the determination of J_c.

We have determined total transport J_c by using four different criteria, (i) E = 0.001 mV/cm, (ii) 0.005 mV/cm, (iii) 0.01 mV/cm and (iv) 0.02 mV/cm. In the inset of **Figure 4.3.2**, we have shown how a criterion is used to extract J_c for a particular temperature. We have used total $J_c = I_c$/area of cross section of the bar-shaped sample where I_c is current corresponding to a specific E-

based criterion. **Figure 4.3.3**, we have shown extracted $J_c(T)$. Clearly the nature of $J_c(T)$ changes strongly with the choice of the criterion [1, 14]. Near T_c, J_c converges to zero indicating criteria independent nature. However, with the decreasing T, $J_c(T)$ diverges strongly. As revealed in **Figure 4.3.3**, we observe that $J_c(T = 78.0\ \text{K}) \sim 25.0\ \text{mA/cm}^2$ for the criterion $E = 0.001$ mV/cm whereas $J_c(T = 78.0\ \text{K}) \sim 300.0\ \text{mA/cm}^2$ for the criterion with a higher $E = 0.02$ mV/cm. Therefore, if the criterion is enhanced roughly by 20.0 times, the highest observed J_c increases by an order of 12 times at the lowest possible T (78.0 K). Therefore, the highest possible extrapolated $J_c(T = 0)$ will be even more affected in such a process. Using a criterion of $E = 0.002$ mV/cm, the transport J_c in RE-123 superconductors is reported to be $200 - 500\ \text{A/cm}^2$ at zero magnetic field [15].

An exponent n is used successfully to understand the nature of pinning from the variation of $J_c(T)$ in HTS [16, 17]. In the inset of **Figure 4.3.3**, we have shown the J_c as a function of $[1\text{-}(T/T_c)^2]^n$ for all four E-based criteria. We observed that the exponent $n \sim 1.1$ and remains almost unchanged for all four criteria. It indicates that δT_c pinning is dominating in BZO added YBCO [18]. However, the analysis becomes very sensitive on criteria with the increase in $1\text{-}(T/T_c)^2$. Therefore, the exponent-based analysis of J_c to understand the underlying vortex pinning becomes more sensitive as the temperature is lowered from T_c.

An important analysis of $J_c(T)$ in the HTS systems is to describe in terms of (i) the Ambegaokar–Baratoff (AB) equation, (ii) the Ginzburg–Landau (GL) equation and (iii) a possible transition between the AB to GL framework. We have studied how four criteria affect the analysis of $J_c(T)$ based

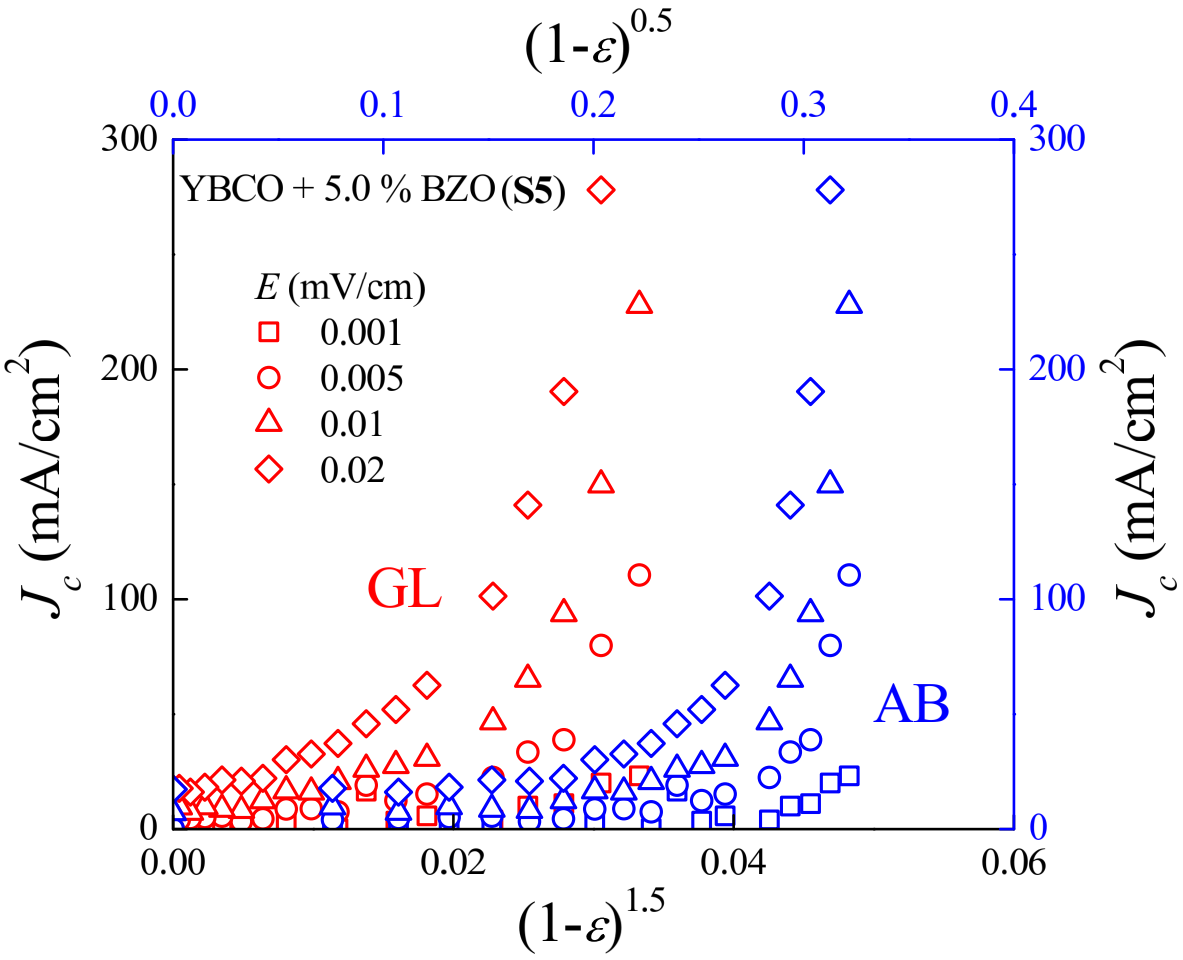

Figure 4.3.4: Variations of total critical current density J_c as a function of (i) $(1\text{-}\varepsilon)^{0.5}$ (AB) and (ii) $(1\text{-}\varepsilon)^{1.5}$ (GL) corresponding to different criteria.

on the AB and GL equations. By using an expression for $J_c(T)$, both AB and GL can be expressed with the help of an exponent α as follows: $J_c(T) = J_c(0)(1 - \varepsilon)^{\alpha}$, $\varepsilon = T/T_c$ is the reduced temperature. Exponents are known to be 1.5 and 0.5 for the GL and AB descriptions, respectively [19]. We have coefficients $J_c(0) = J_c^{GL}(0)$ and $J_c(0) = J_c^{AB}(0)$ corresponding to 1.5 and 0.5, respectively. In **Figure 4.3.4**, we have shown how different criteria affect the interpretations for both the GL and AB description of transport J_c. For both descriptions, a diverging nature is observed with the increase in $(1 - \varepsilon)^{\alpha}$ with the decrease in T.

BZO-added YBCO samples are having granular nature revealed in SEM,

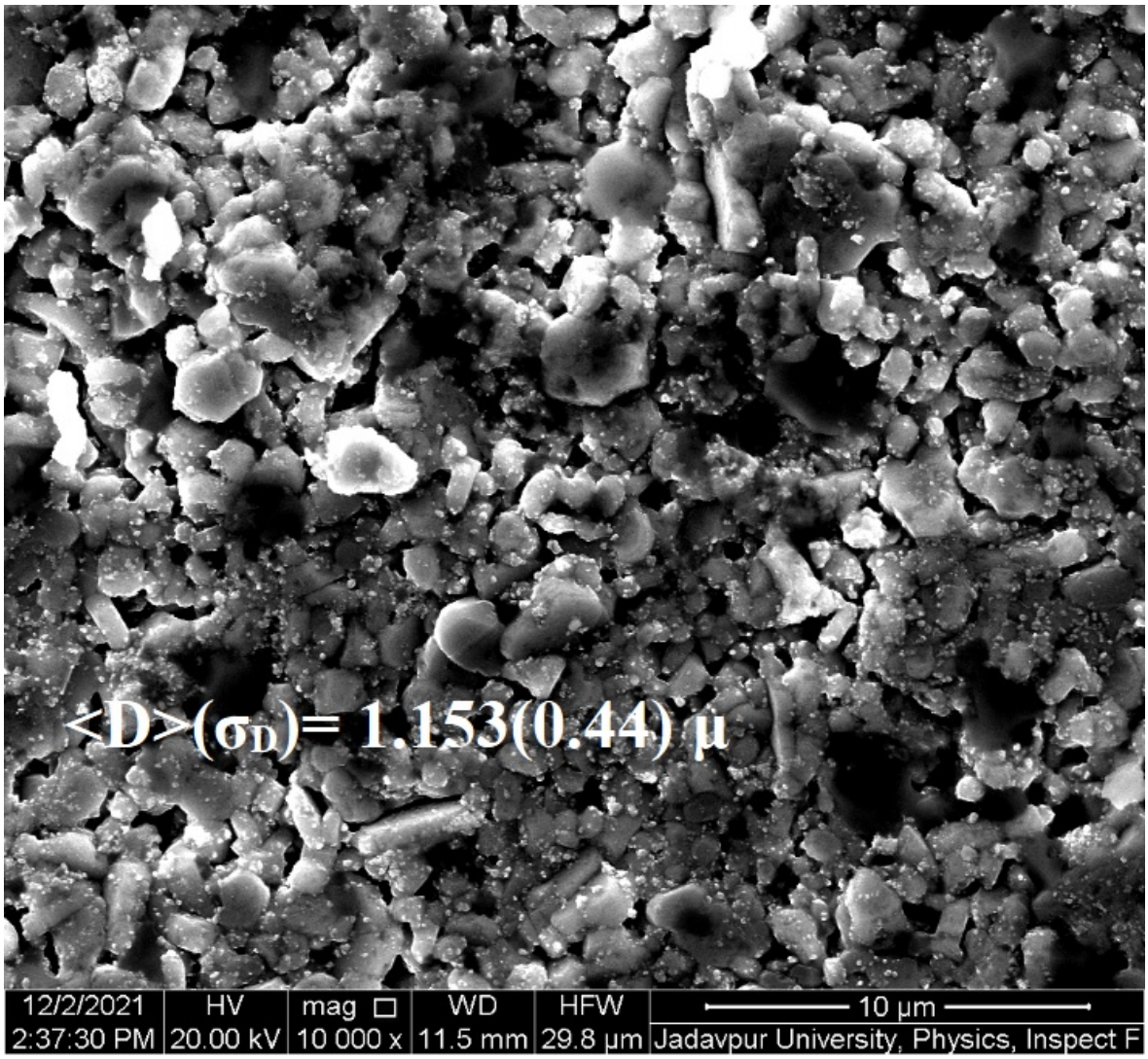

Figure 4.3.5: A typical Scanning Electron micrograph of BZO added YBCO. An average grain size $\sim$ 1.153 μm has been used for the extraction of intra granular J_{cG}.

as shown in **Figure 4.3.5**. The average size of grains of BZO added YBCO is found to be $\sim$ 1.0 μm. Intra granular critical current density, J_{cG} within the grain has been extracted with the help of the average size of grains **[20 - 22]**. We have extracted $J_{cG} = I_c$/average area of a grain. In **Figure 4.3.6**, we have shown $J_{cG}(T)$ for four different criteria. At 78.0 K, J_{cG} is found to be $\sim$ 0.4x10^5 A/cm^2 for the criterion E = 0.001 mV/cm. As we increase E, the possible J_{cG} is increased to 3.7x10^5 A/cm^2. Therefore, by increasing the criterion by 20 times J_{cG} varies by an order of about 9.2 times. In thin

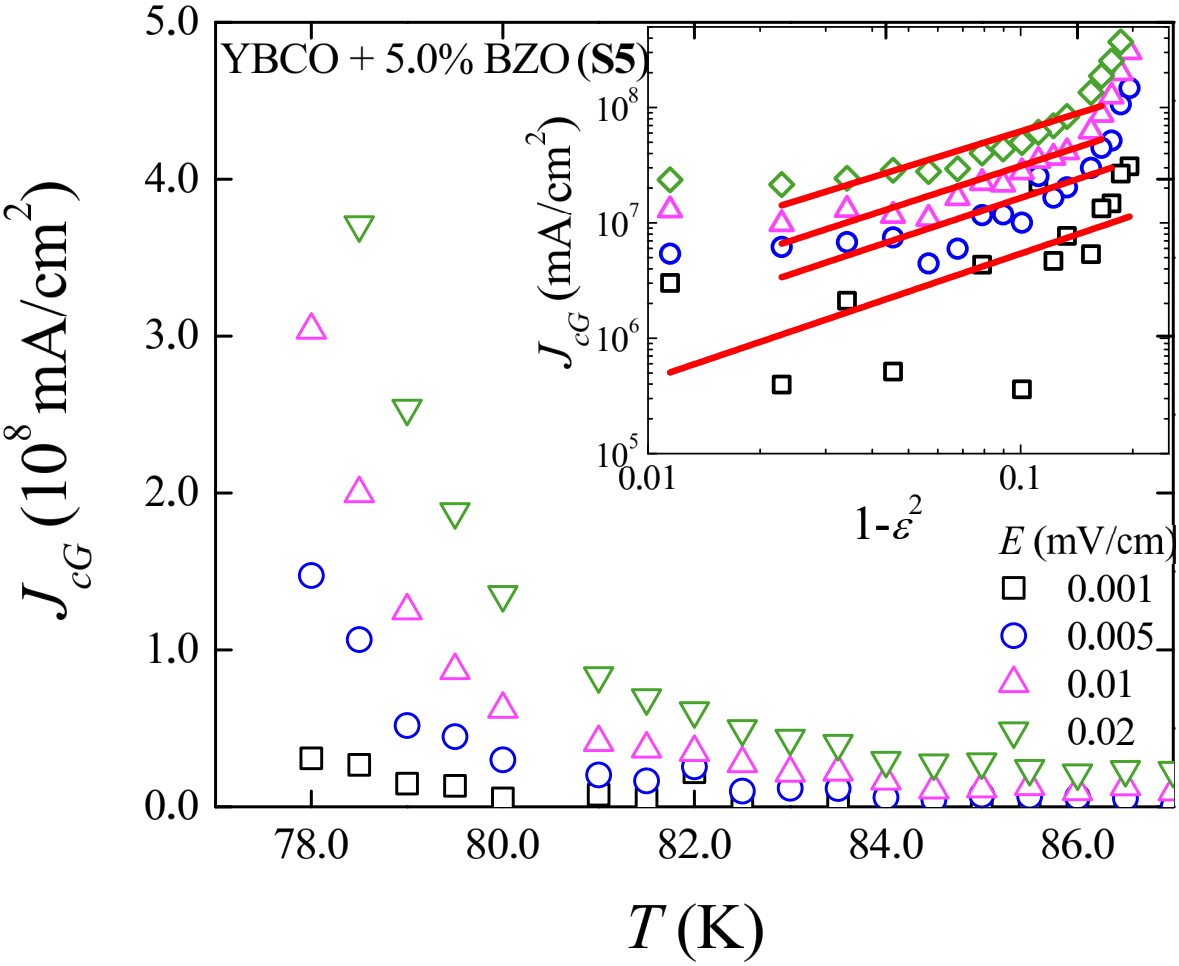

Figure 4.3.6: Intra granular critical current density J_{cG} of BZO added YBCO as a function of T for several electric field criteria. In the inset the log-log variations of J_{cG} with [1 - $(T/T_c)^2$] for four E-based criteria

film of the pure YBCO, $J_c \sim 2.2\text{x}10^6$ A/cm^2 at T = 78.0 K is reported by using IV characteristics and a specific criterion [23]. In addition, the factor by which one compares J_c of any two superconductors such as (i) YBCO and (ii) YBCO+ BZO may also be affected by criteria for the determination of J_c from IV.

It will be important to mention that we have not observed any transition from J_{cG} to J_c in our sample because we have used a current range (100 nA – 5.0 mA). In another sample, it has been detected in relatively higher current $\sim$ few Ampere [24]. Because we do not detect any J_{cG} to J_c transition in our

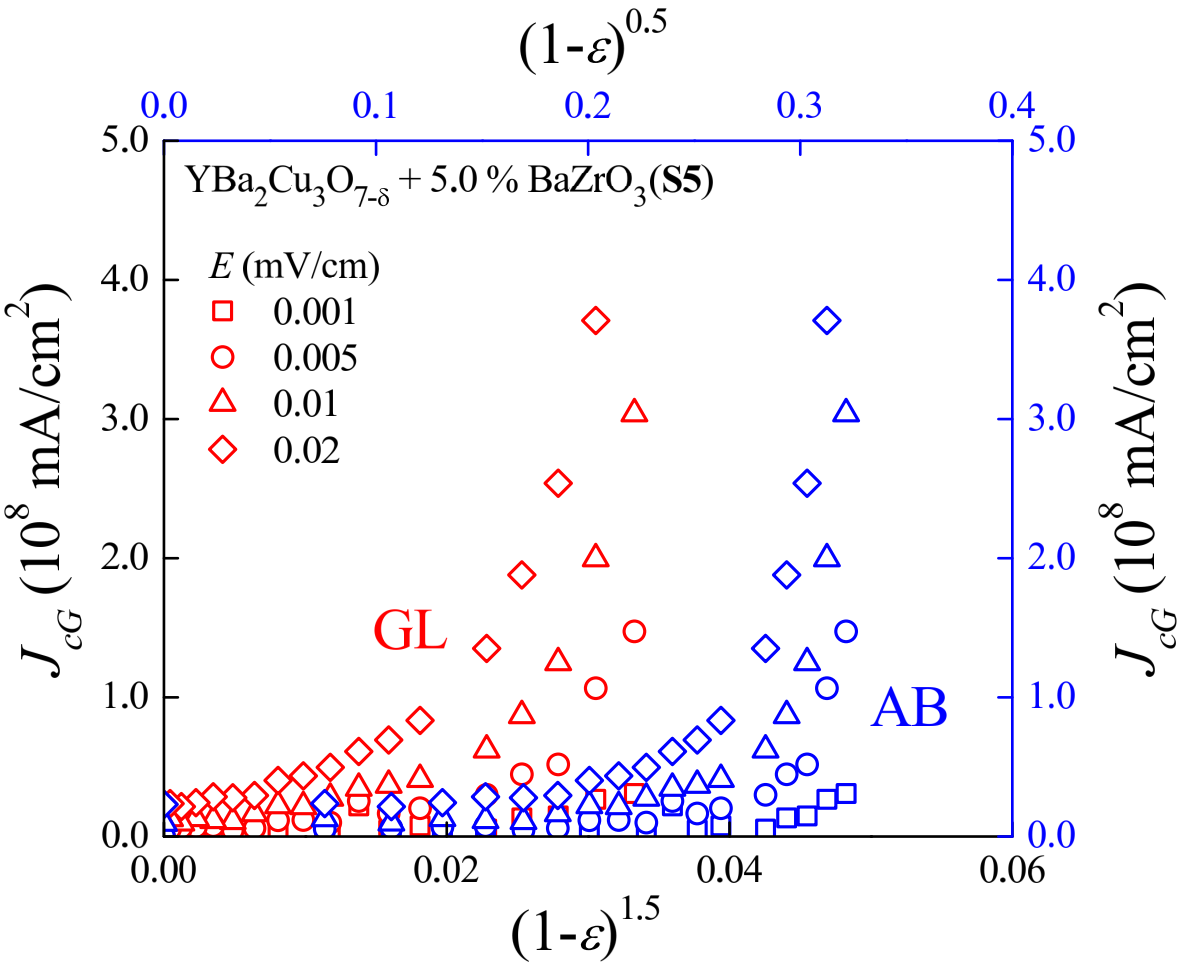

Figure 4.3.7: Variations of intra granular critical current density J_c as a function of (i) $(1 - \varepsilon)^{0.5}$ (AB) and (ii) $(1 - \varepsilon)^{1.5}$ (GL) corresponding to different criteria.

sample, therefore it is not possible to know how different E-based criteria affect the same.

In the inset of **Figure 4.3.6**, we have shown J_{cG} as a function of $[1 - (T/T_c)^2]$ in the log-log scale. We have extracted the exponent n $\sim$ 1.1 for all four criteria. It reveals that intra granular J_{cG} also follows δT_c pinning as is observed in total J_c. Therefore, even though the addition of BZO in the grain boundary of YBCO enhances critical current density, the nature of δT_c pinning remains unaltered ($n \sim 1.1$) and it is almost independent of the criteria at an intermediate range of T. However, as the temperature is lowered, the

analysis of the nature of pinning becomes independent of criteria.

In **Figure 4.3.7**, we have shown how J_{cG} varies with $(1 - \varepsilon)^{0.5}$ within the framework of the AB for different criteria. As $(1 - \varepsilon)^{0.5}$ increases the diverging nature of J_{cG} becomes very prominent with criteria. For the same set of criteria, we have also shown J_{cG} as a function of $(1 - \varepsilon)^{1.5}$ following the GL description. Clearly, as the $(1 - \varepsilon)^{1.5}$ increases, the diverging nature of J_{cG} becomes visible with criteria. Because measuring IV below $T_c(\rho = 0)$ is not possible, a transition from the GL behavior near onset T_c to the AB description at lower T is not observed in the present sample. However, the AB and GL behaviors may also be affected depending on different electric field criteria. It also indicates that for both descriptions, the extrapolated values of $J_{cG}^{AB}(0)$ and $J_{cG}^{GL}(0)$ will strongly depend on criteria.

4.4 Summary

Current-voltage (IV) characteristics below T_c have been used to extract two different critical current densities (J_c and J_{cG}) in BZO added YBCO bulk superconductors. Extraction of J_c and J_{cG} depends strongly on the electric field criteria. The δT_c pinning nature revealed by the temperature dependence of J_c and J_{cG} may be altered by the variations of criteria. The AB and GL coefficients (at $T = 0$) change in order of magnitude with the electric field criteria.

4.5 References

1. A. V. Pan, I. A. Golovchanskiy, S. A. Fedoseev, Euro. Phys. Lett. **103** (2013) 17006.

2. P. Sunwong, J. S. Higgins, Y. Tsui, M. J. Raine, D. P. Hampshire, Supercond. Sci. Technol. **26** (2013) 095006.

3. V. Ambegaokar, A. Baratoff, Phys. Rev. Lett. **10** (1963) 486; **11** (1963) 104.

4. H. Darhmaoui, J. Jung, Phys. Rev. B **53** (1996) 14621.

5. J. R. Clem, B. Bumble, S. I. Raider, W. J. Gallagher, Y. C. Shih, Phys. Rev. B **35** (1987) 6637.

6. S. H. Wee, A. Goyal, E. D. Specht, C. Cantoni, Y. L. Zuev, V. Selvamanickam, S. Cook, Phys. Rev. B **81** (2010) 140503.

7. K. Schlesier, H. Huhtinen, P. Paturi, Y. P. Stepanov, R. Laiho, IEEE Trans. Appl. Supercond. **19** (2009) 3407.

8. M. Peurla, H. Huhtinen, M. A. Shakhov, K. Traito, Yu. P. Stepanov, M. Safonchik, P. Paturi, Y. Y. Tse, R. Palai, R. Laiho, Phys. Rev. B **75** (2007) 184524.

9. D. Rakshit, T. Sk, P. Das, S. Haldar, A. K. Ghosh, Physica C **588** (2021) 1353909.

10. T. Sk, A. K. Ghosh, J. Low Temp. Phys. **198** (2020) 224.

11. G. Wang, M. J. Raine, D. P. Hampshire, Supercond. Sci. Technol. **30** (2017) 104001.

12. A. Crisan, M. M. A. Kechik, P. Mikheenko, V. S. Dang, A. Sarkar, J. S. Abell, Supercond. Sci. Technol. **22** (2009) 045014.

13. H. Hilgenkamp, J. Mannhart, Rev. Mod. Phys. **74** (2002) 485.

14. I. A. Golovchanskiy, A. V. Pan, S. A. Fedoseev, O. V. Shcherbakova, S. X. Dou, Physica C **479** (2012) 151.

15. S. Jin, R. A. Fastnacht, T. H. Tiefel, R. C. Sherwood, Phys. Rev. B **37** (1988) 5828.

16. R. Griessen, W. Hai-Hu, A. J. J. van Dalen, B. Dam, J. Rector, H. G. Schnack, Phys. Rev. Lett. **72** (1994) 1910.

17. G. Blatter, M. V. Feigel'man, V. B. Geshkenbein, A. I. Larkin, V. M. Vinokur, Rev. Mod. Phys. **66** (1994) 1125.

18. T. Aytug, M. Paranthaman, K. J. Leonard, S. Kang, P. M. Martin, L. Heatherly, A. Goyal, A. O. Ijaduola, J. R. Thompson, D. K. Christen, Phys. Rev. B **74** (2006) 184505.

19. J. L. Cardoso, P. Pereyra, Phys. Rev. B **61** (2000) 6360.

20. J. R. Thompson, J. Brynestad, D. M. Kroeger, Y. C. Kim, S. T. Sekula, D. K. Christen, E. D. Specht, Phys. Rev. B **39** (1989) 6652.

21. P. Mandal, D. Rakshit, T. Sk, A. K. Ghosh, J. Supercond. Nov. Mag. **35** (2022) 1079.

22. P. Mandal, D. Rakshit, I. Mukherjee, T. Sk, A. K. Ghosh, Phys. Lett. A **436** (2022) 128072.

23. M. Darwin, J. Deak, L. Hou, M. McElfresh, E. Zeldov, J. R. Clem, M. Indenbom, Phys. Rev. B **48** (1993) 13192.

24. A. Diaz, J. Maza, F. Vidal, Phys Rev. B **55** (1997) 1209.

Chapter 5

Microparticle controlled superfluid density and critical current density in $YBa_2Cu_3O_{7-\delta}$

5.1 Introduction

The critical current density of high-temperature superconductors (HTSs) is influenced by the interaction of vortices and the pinning centers located within the lattice. Size, shape and orientation of the pinning centers with the columnar vortex in YBCO are very crucial factors to control the critical current density by an order of magnitude [1, 2]. Besides the pinning by the disorder in the lattice sites of YBCO, pinning by the intergranular region has been very efficient in bulk superconductors [3 - 5]. Inclusions of different pinning centers in the intergranular region (outside the lattice and grains) have been attempted to enhance the critical current density [6, 7]. Density of such pinning centers in addition to the nature of the inclusions in the intergranular networks plays a very crucial role. Even though it is not clear why the in-

clusions in the intergranular networks will affect the critical current density, several ideas are emerging to resolve related issues which will be of immense help in enhancing the critical current density [8 - 10].

There are several methods to understand the correlation between the critical temperature and the superfluid phase stiffness (SPS) [11, 12]. Superfluid density has a major impact on the upper critical field and critical current density. Near the onset of the superconducting transition, the superfluid density starts growing with the decrease in T [13]. However, it is not known how the superfluid density and hence the critical current density will be affected by the intergranular region in bulk superconductors. Several attempts have been made to enhance the critical current density by adding additional pinning sites in the intergranular regions [14 - 16]. $BaZrO_3$ (BZO) is such a compound, and the addition of which affects the current density strongly in YBCO [17 - 20]. We have studied the exponent (η) and the superfluid phase stiffness (J_s) by using the current-voltage (IV) characteristics of several YBCO +x% BZO composite bulk systems. The critical current density in the phase transition region of such systems has been extracted using a specific criterion. The variations of $J_s(T)$, $J_c(T)$ and $J_{cG}(T)$ have been studied to obtain a probable correlation near the phase transition region.

5.2 Experimental

Synthesis of bulk $YBa_2Cu_3O_{7-\delta}$ (YBCO) superconducting samples has been done by using the standard solid-state reaction method [21, 22]. The sintering temperatures of the pure (**S6**) YBCO (x = 0.0) in different stages re-

main in the range between 925 and 950 °C. $BaZrO_3$ (BZO) powder has been mixed in YBCO to obtain YBCO-BZO compound during the sintering. We have used x = 2.5% (**S7**), 5.0% (**S8**), 7.5% (**S9**) and 10.0% (**S10**) of BZO as weight % of pure YBCO. Annealing of the pure and mixed samples is carried out at 450 °C using a uniform oxygen flow rate for 60 hours. We annealed all samples together at a temperature of 450 °C using a rate of increase of 5 °C/min, and the cooling rate is 2 °C/min for the homogenization of oxygen. The annealing process has been done for a longer period of 60 hours which is very usual in YBCO. We have characterized all samples by using standard scanning electron micrographs (SEMs). We have used a bar-shaped sample for transport measurements. Typical dimensions of the samples are 5.8 mm×2.4 mm×0.6 mm. Resistivity as a function of temperature has been measured by using the standard four-probe method with the help of a cryo-generator (Janis, USA) [23 - 25]. The temperature sweep rate used in $R(T)$ measurement is $\sim$ 0.5 K/min. At several constant temperatures, IV measurements have been carried out below T_c. The range of the current used for IV measurements is 100.0 nA through 5.0 mA.

5.3 Results and Discussions

In **Figure 5.3.1**, we have shown the representative micrographs of the pure and BZO-mixed YBCO samples. The microstructure of the pure YBCO is found to be in well-separated granular nature with a distribution of the size of grains. Using an ImageJ software program, we have extracted the average grain size (D) and variance (σ_D) as shown in **Figure 5.3.1** [26]. We observed

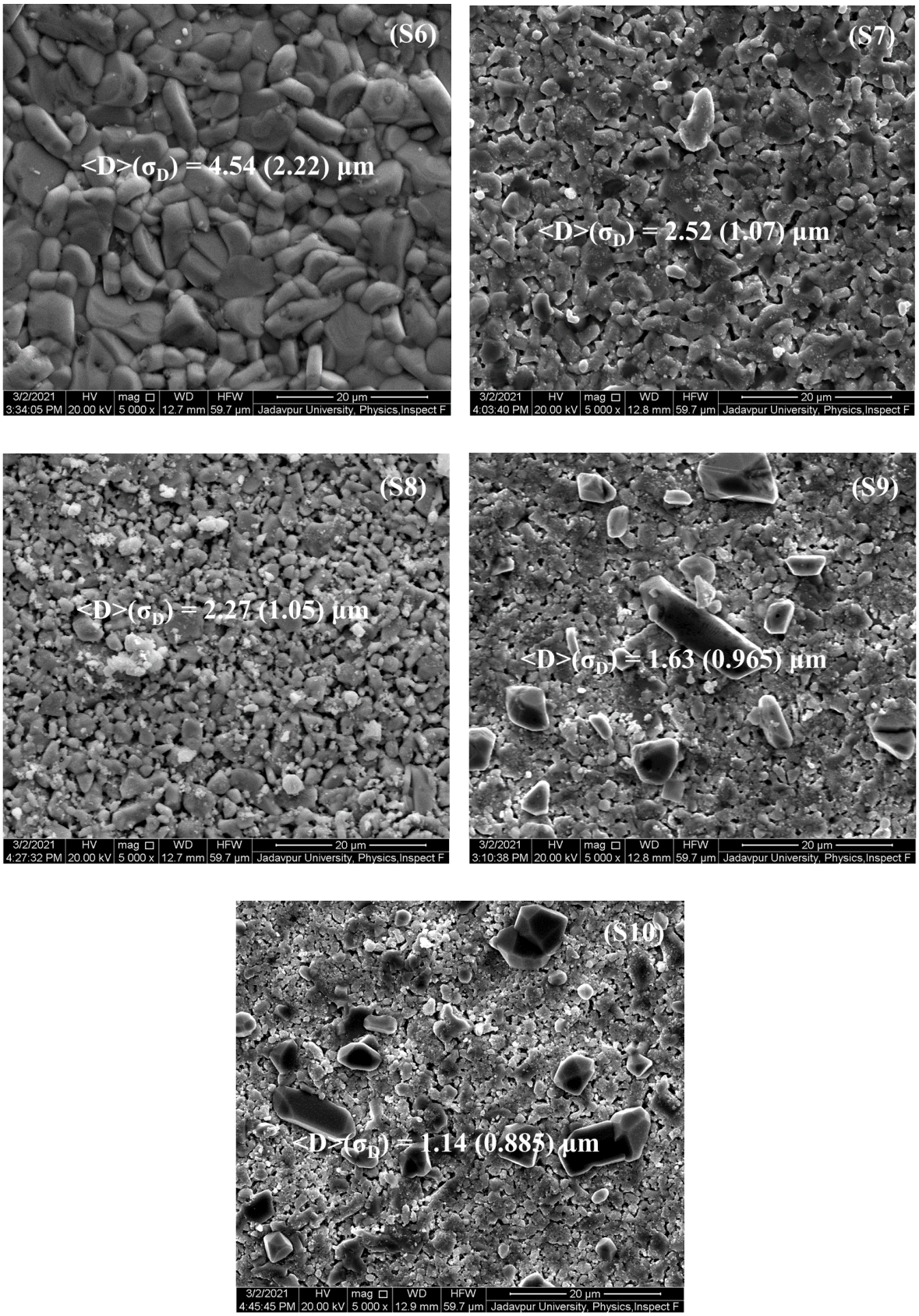

Figure 5.3.1: Representative scanning electron micrographs (SEMs) of the samples with x = 0.0 (**S6**), 2.5 (**S7**), 5.0 (**S8**), 7.5 (**S9**) and 10.0 (**S10**)

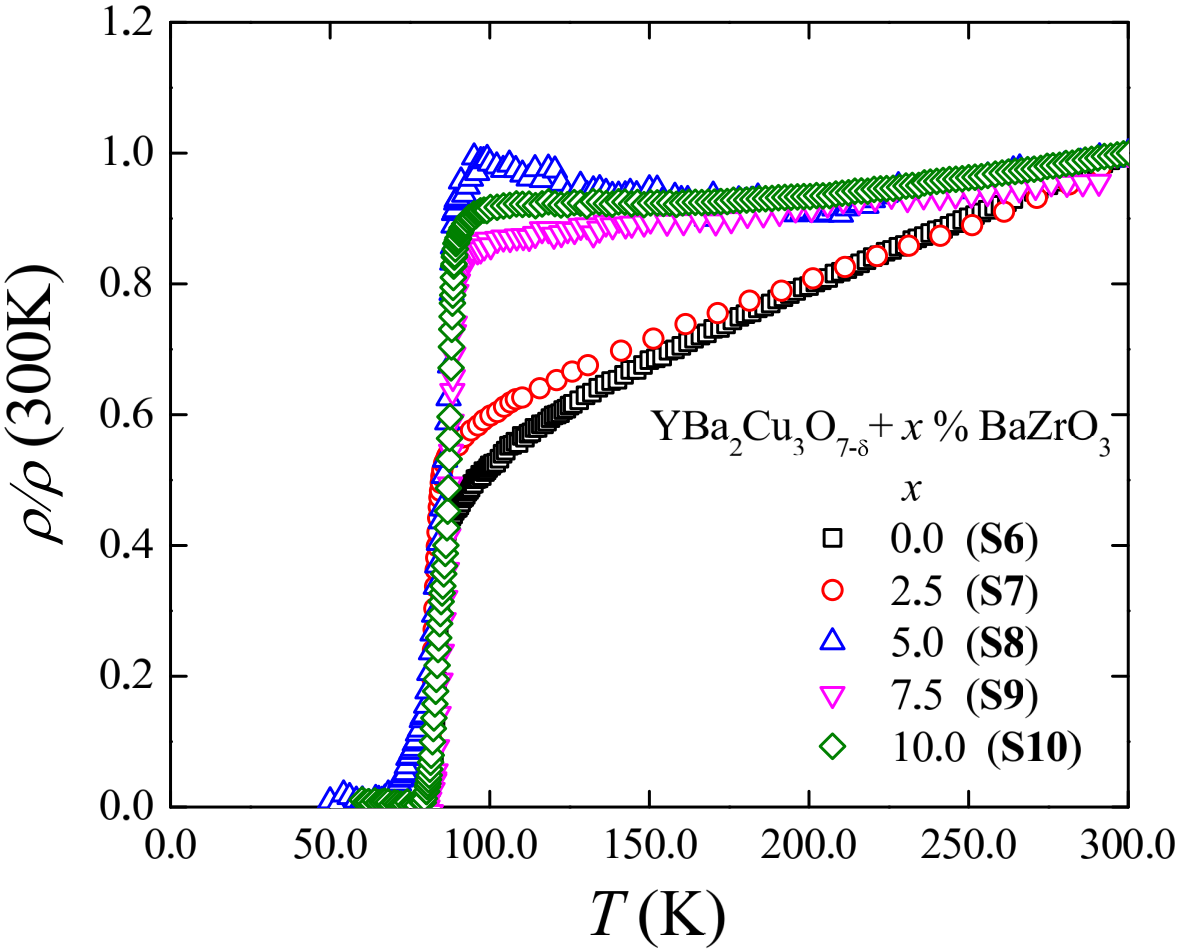

Figure 5.3.2: Normalised resistivity as a function of the temperature of pure (x = 0.0) $YBa_2Cu_3O_{7-\delta}$ (YBCO) superconductor and BZO-mixed YBCO with x = 2.5%, 5.0%, 7.5% and 10.0%

that the average grain size decreases with the increase of x. However, as the concentration of BZO is increased, the intergranular region is filled with the BZO and it results in the lowering in the separation between grains as well.

We have shown the variations of the normalised resistivity, $\rho/\rho(300\ \mathrm{K})$, as a function of T in **Figure 5.3.2**. The onset critical temperatures (T_c) are found to be 88.0 K, 87.1 K, 92.0 K, 92.2 K, and 89.6 K corresponding to x = 0.0, 2.5, 5.0, 7.5, and 10.0, respectively. Therefore, there is no systematic change in onset critical temperature. It is important to understand the role of oxygen inhomogeneity within grains because it affects T_c. However, the

longer annealing highly minimizes T_c variation from grain to grain because of the longer diffusion time [27 - 29]. It reflects that added low-density BZO microparticles are mostly confined in the intergranular regions. However, the region just above the onset critical region gets strongly affected which has been revealed in the change in the ratio $\rho/\rho(300\ \mathrm{K})$. A drastic change in $\rho/\rho(300\ \mathrm{K}) = 0.4$ for $x = 2.5\%$ to $\rho/\rho(300\ \mathrm{K}) = 0.8$ for $x > 2.5\%$ has been observed in the vicinity of the onset critical temperature of pure YBCO. Change in resistivity as a result of the addition of BZO in superconductor has also been observed [30]. As a result of the inclusion of BZO in the intergranular region, an elongated Δ-shaped region has been observed in the variation of $\rho/\rho(300\ \mathrm{K})$ as a function of T. In the Δ-shaped region at constant T above T_c, an abrupt change in $\rho/\rho(300\ \mathrm{K})$ with x has been observed and this effect gets suppressed with the increase in T. Therefore, impact of the BZO above a certain percentage of x may not be that effective in changing the intergranular region in controlling the normal-state transport properties in a wide range of temperatures. In addition, it has been observed that the superconducting phase transition region is highly affected as a result of BZO nanoparticles even in the zero magnetic field [31]. In polycrystalline **S7 – S10** samples, grain boundary plus microparticles of BZO together form the insulating (I) region of the Josephson junctions (superconductor-insulator-superconductor (SIS)) [32]. T_c of superconductors (in an SIS) does not change due to a change in the insulating region, but definitely, the overall current flow gets affected. Moreover, within a Josephson junction, it is really difficult to separate out and quantify how much granularity and BZO contribute to the transport. BZO is added in the intergranular region between randomly oriented grains.

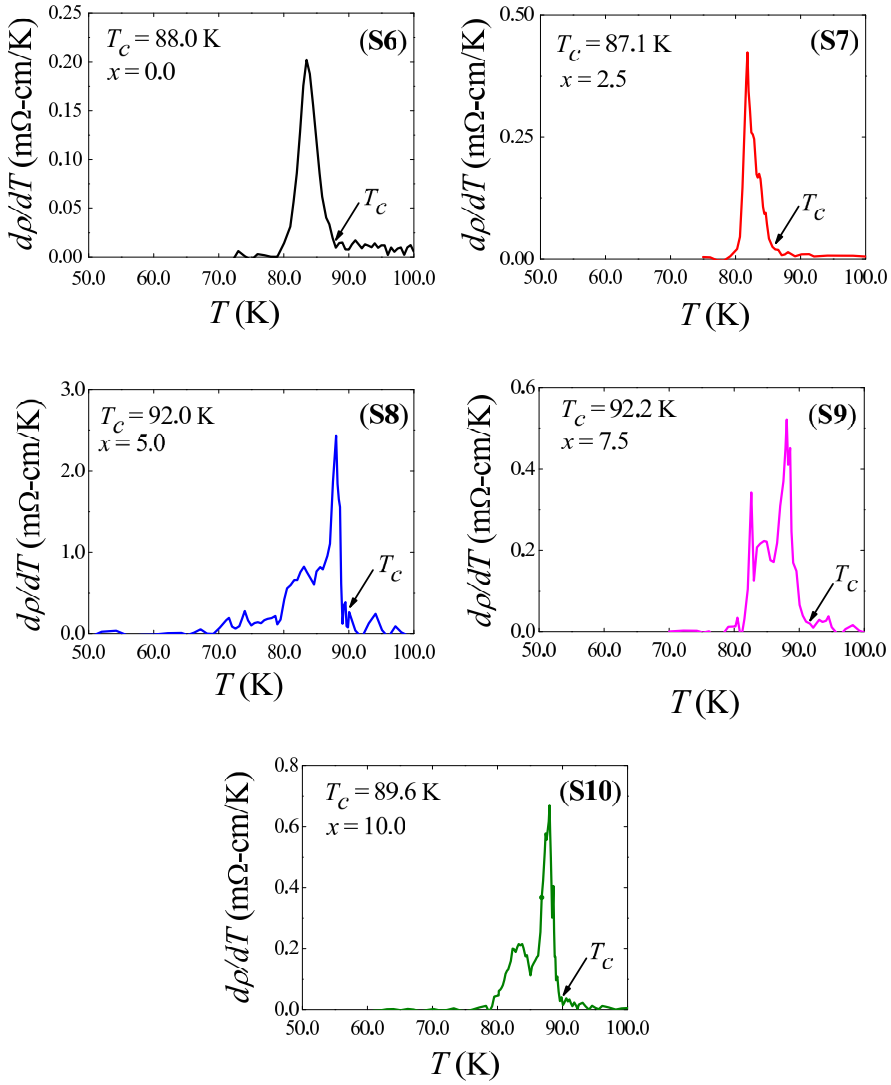

Figure 5.3.3: Variations of $d\rho/dT$ as a function of T of YBCO with x = 0.0, 2.5, 5.0, 7.5 and 10.0. We have shown critical temperatures by an arrow.

Because all samples (**S6** – **S10**) are granular in nature, therefore we believe BZO together with grain boundary affects resistivity [33]. However, since T_c is an intrinsic property (related to the onset of pairing) that is affected weakly, no systematic trend is observed because of the randomness of the addition of BZO.

In **Figure 5.3.3**, we have shown the variation of $d\rho/dT$ as a function of T corresponding to x = 0.0, 2.5, 5.0, 7.5 and 10.0, respectively. For x = 0.0 and 2.5, we have seen that there is a single peak in the variation of

$d\rho/dT$, representing that at low concentration of the BZO, the intergranular region is affected but not the superconducting onset temperature [34]. We have observed that for $x = 5.0$, there is a peak $d\rho/dT \sim 2.2$ mΩ-cm/K which is the highest value of comparing all samples with x. In addition, there is a signature of the visibility of a broad peak below the onset sharp peak. With the further increase in $x = 7.5$ and 10.0, we have observed multiple peaks in $d\rho/dT$. It indicates that even though the critical temperature does not change strongly and systematically with the increase in x, the intergranular region gets heavily affected for $x > 2.5$. The variation of the peak in $d\rho/dT(T)$ with x is very consistent with the variation of T_c in BZO-added YBCO thin film [15]. In addition, the variation of T_c in BZO-added YBCO has been found to be less than 2.0 K which is also comparable to the result of BZO added in the bulk YBCO superconductor up to $x = 10.0$ [15, 35].

We have shown IV characteristics of the pure YBCO ($x = 0.0$) below T_c in **Figure 5.3.4**. At the lowest temperature of $T = 82.4$ K as shown in **Figure 5.3.4**, IV curve exhibits a nonlinear behavior [36, 37]. The nonlinear behavior of IV curves persists over a range of temperature, and the linearity in IV appears above ~ 86.0 K. In **Figure 5.3.5**, we have shown IV characteristics of the sample with $x = 2.5$ in the range of $T = 80.2 - 87.0$ K. For $x = 2.5$, the nonlinear behavior of IV has been observed in the range of 80.0 K through 83.0 K. In **Figure 5.3.6**, we have shown IV characteristics of the composite sample with $x = 5.0$ within the range of $T = 74.0$ K through 92.0 K. The nonlinear behavior is prominent below 84.0 K. IV curves for the sample with $x = 7.5$ are plotted in **Figure 5.3.7** in which nonlinearity is observed in the range of 78.0 K through 85.0 K. The sample with the highest BZO concentration of

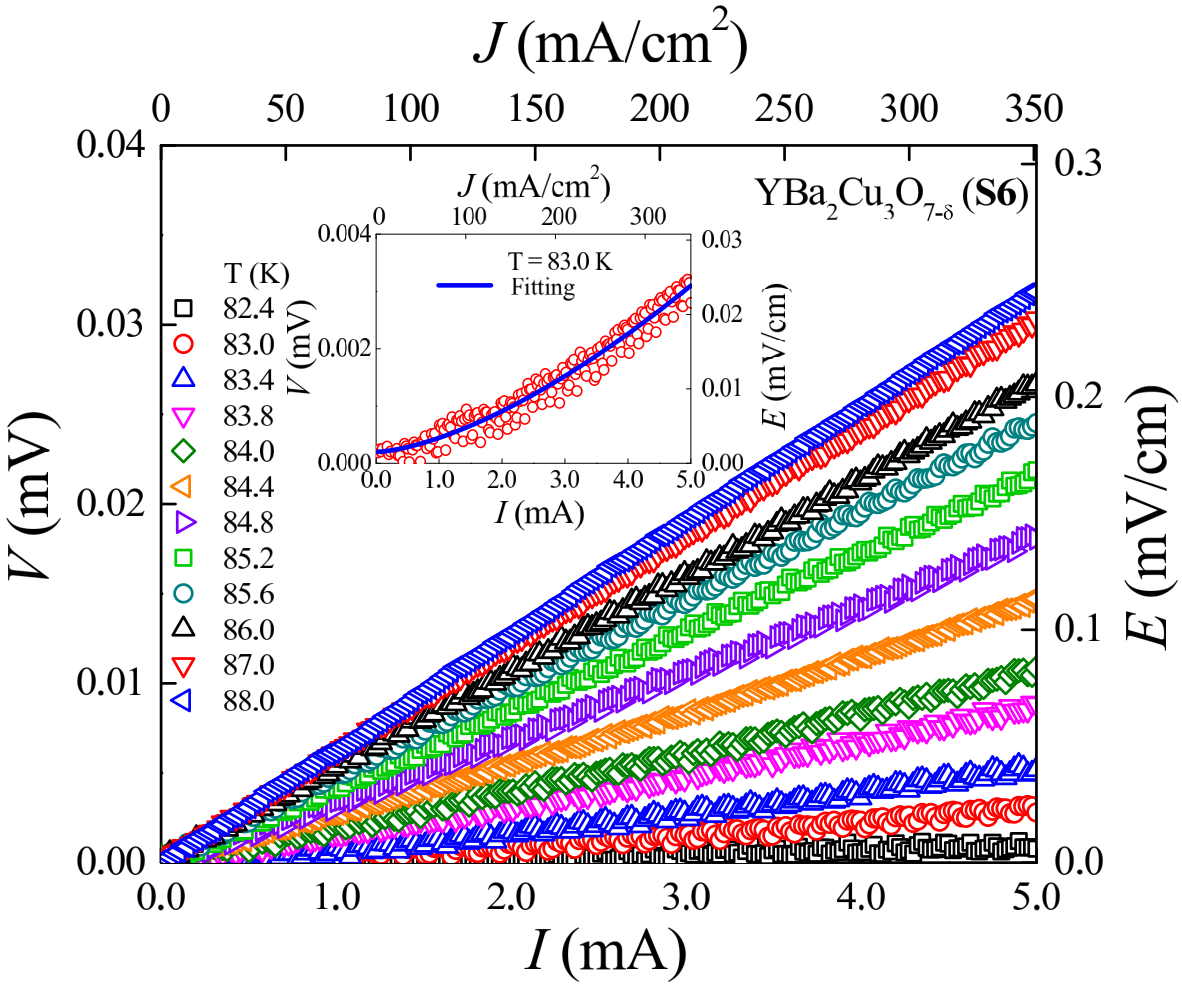

Figure 5.3.4: Current–voltage (IV) characteristics of the sample with $x = 0.0$ (**S6**) at several temperatures below critical temperature

$x = 10.0$ exhibits a nonlinear behavior of IV in the range of 77.0 K through 82.0 K as shown in **Figure 5.3.8** [38, 39].

Table 5.1: Fitting parameters of the critical current density (J_c)

x(%)	J_{c0}(mA/cm^2)	$J_c(0)$(mA/cm^2)	T_{0J}(K)
0.0 (**S6**)	11.12	2.20×10^{52}	0.72
2.5 (**S7**)	8.41	1.2×10^{60}	0.60
5.0 (**S8**)	1.96	3.11×10^{26}	1.33
7.5 (**S9**)	5.03	3.54×10^{29}	1.26
10.0 (**S10**)	7.03	1.38×10^{27}	1.36

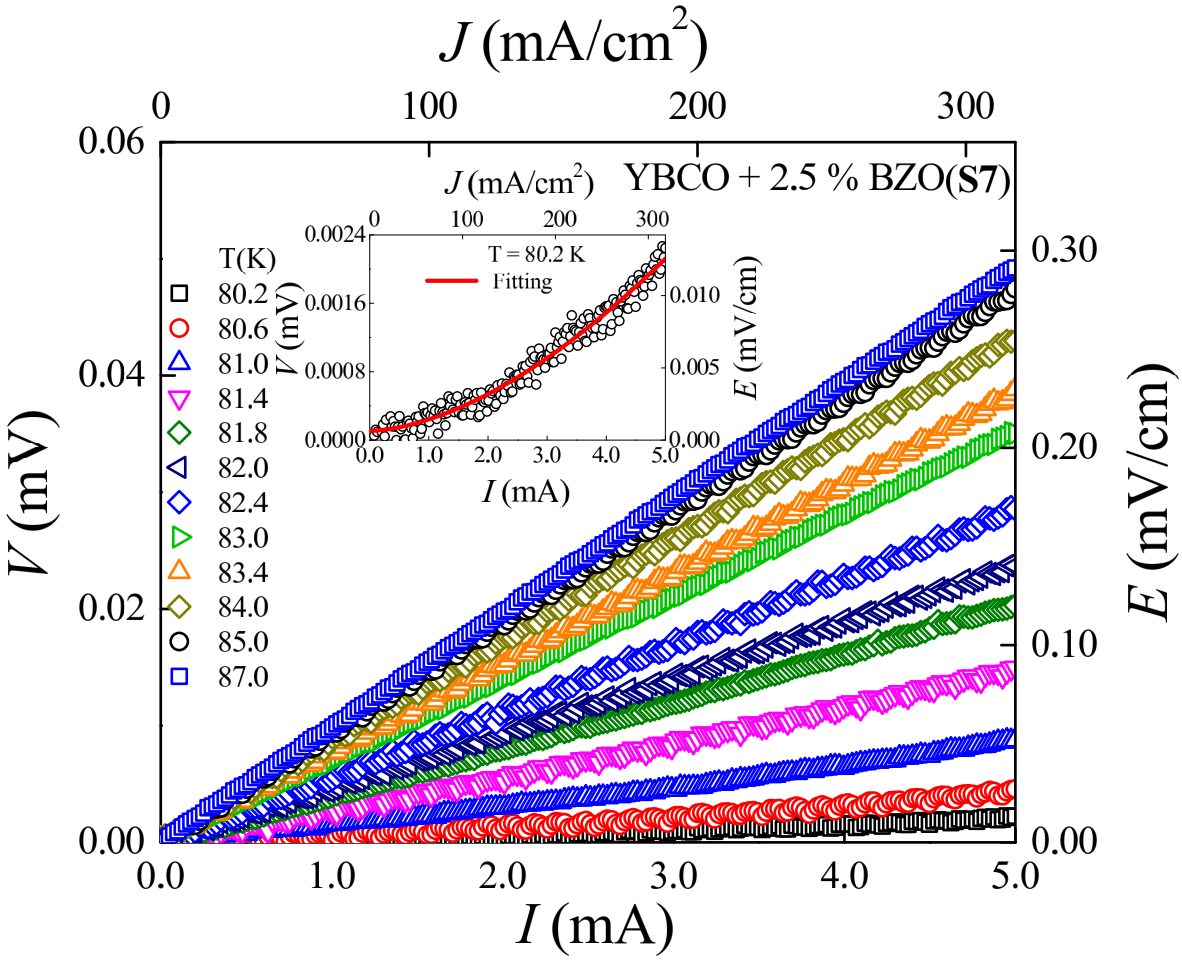

Figure 5.3.5: Current–voltage (IV) characteristics of the sample with $x = 2.5$ (**S7**) at several temperatures below critical temperature

Table 5.2: Fitting parameters of the granular current density (J_{cG})

$x(\%)$	J_{cG0}(mA/cm^2)	$J_{cG}(0)$(mA/cm^2)	T_{0JG}(K)
0.0 (**S6**)	7.68×10^{5}	1.52×10^{57}	0.72
2.5 (**S7**)	2.08×10^{6}	2.98×10^{65}	0.60
5.0 (**S8**)	4.59×10^{5}	7.26×10^{31}	1.33
7.5 (**S9**)	3.06×10^{6}	2.16×10^{35}	1.26
10.0 (**S10**)	9.31×10^{6}	1.84×10^{33}	1.36

By using the criterion $E = 0.01$ mV/cm, we have extracted the critical current density (J_c) as a function of T near T_c for all samples as shown in **Figure 5.3.9 [40]**. Following **Figure 5.3.9**, we have observed that the value

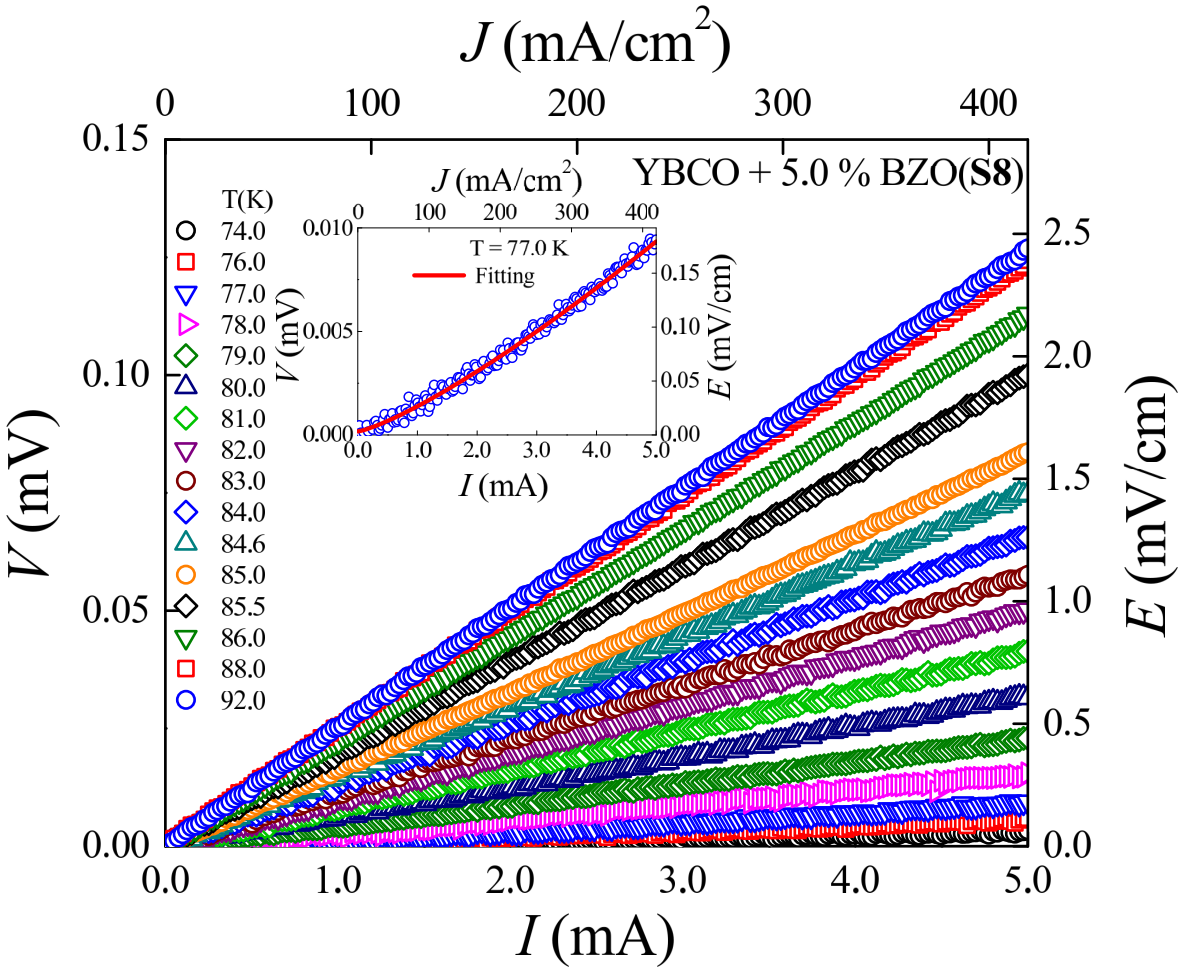

Figure 5.3.6: Current–voltage (IV) characteristics of the samples with $x = 5.0$ (**S8**) at several temperatures below critical temperature

of J_c is very low near T_c. Low J_c is associated with the bulk nature and the area of cross section (typically $\sim$ mm^2) of the bar-shaped samples. The area of the cross section of the bar-shaped sample has been used which gives us such a low J_c because it includes the current within the intergranular region in addition to the current in the superconducting grains. We have observed a major change in the variation of J_c with the increase in x. We have fitted $J_c(T)$ by using an equation, $J_c(T) = J_{c0} + J_c(0)\exp(-T/T_{0J})$ [41]. J_{c0} is a remnant current density that depends on the criterion $E = 0.01$ mV/cm. However, $J_c(0)$ is an extrapolated current density at $T = 0.0$ K. In **Table 5.1**, we have given all fitting numbers. Interestingly, the limitation of the equation is that the ob-

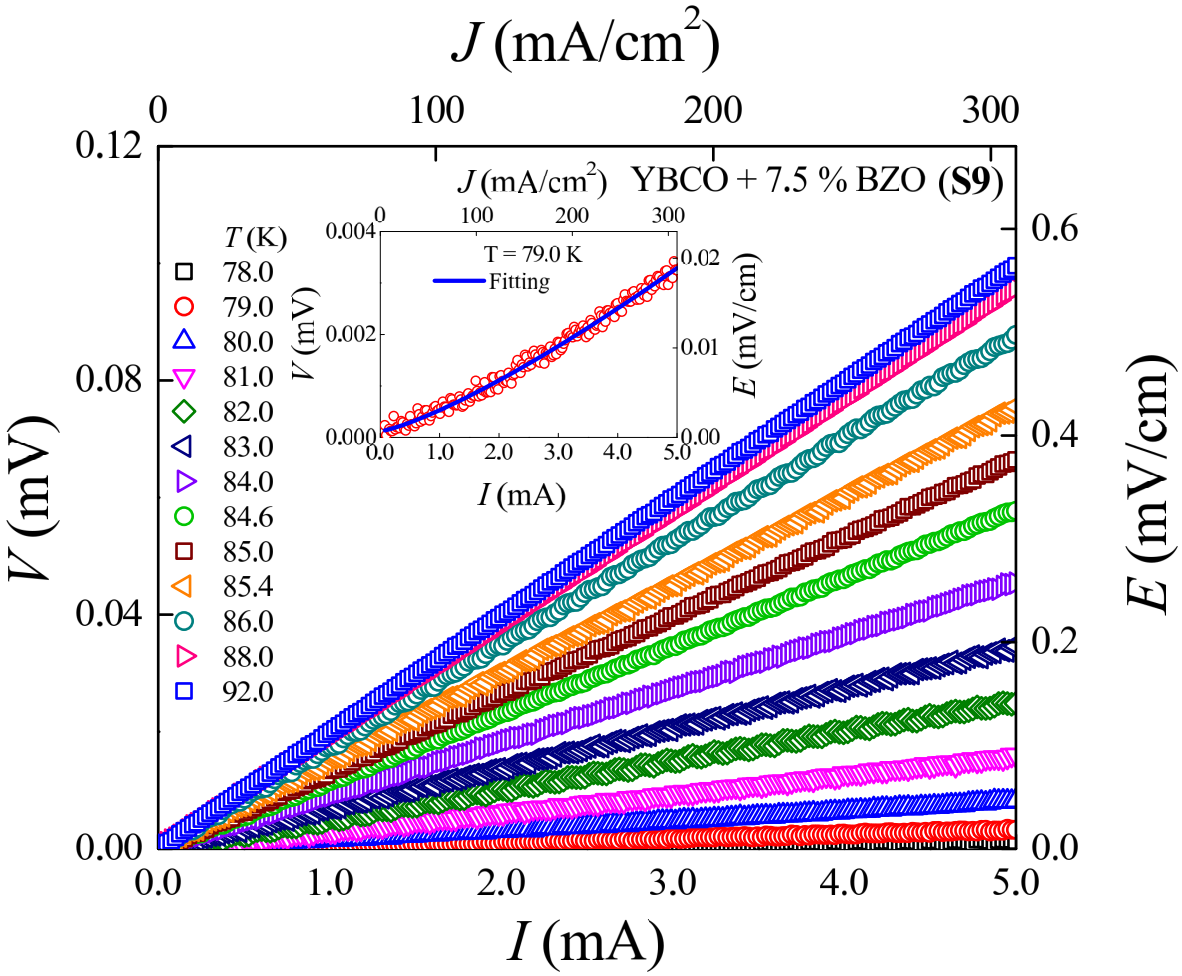

Figure 5.3.7: Current–voltage (IV) characteristics of the samples with $x = 7.5$ (**S9**) at several temperatures below critical temperature

served $J_c(0)$ is very high which may be unrealistic. However, it indicates that even though an exponential behavior of J_c is observed in a range of T close to T_c, the nature of variation changes drastically at lower T. The region we are dealing with is mostly a region in which the vortex fluid state is present. As we lower T, the nature of variation will not be similar as a result of the presence of different solid vortex matter as suggested by Ambegaokar and Baratof [42]. We have also observed that for all samples, $J_{c0} << J_c(0)$ which enables us to use $J_c(T) \cong J_c(0)\ \exp(-T/T_{0J})$. In this nature of variation, T_{0J} is a characteristic temperature. In **Table 5.1**, we have given fitting parameters. Extrapolated $J_c(0)$ is found to be very high which is unphysical for cuprate

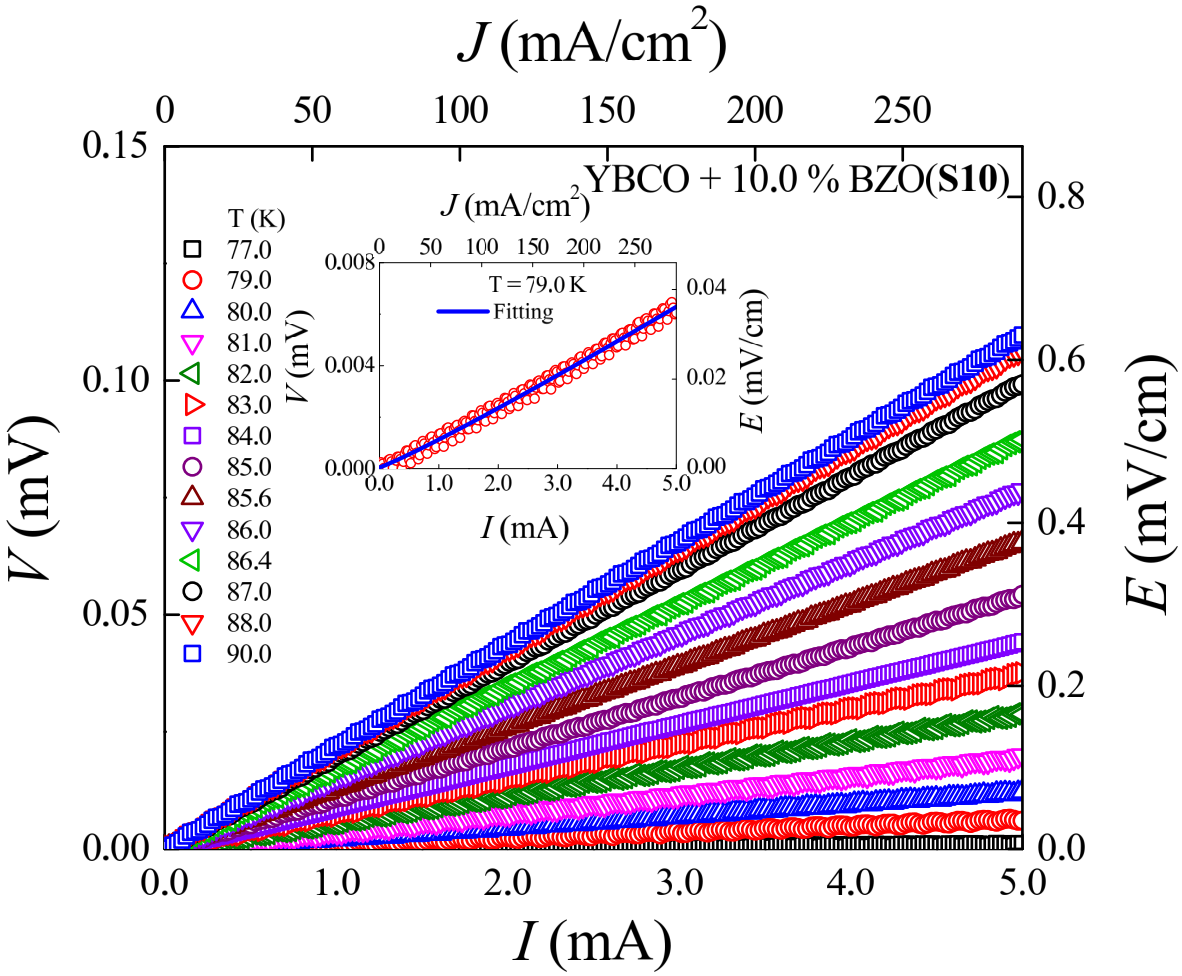

Figure 5.3.8: Current–voltage (IV) characteristics of the samples with x = 10.0 (**S10**) at several temperatures below critical temperature

superconductors. However, close to T_c for vortex liquid states, an exponential function explains $J_c(T)$. Clearly, T_{0J} is sensitive to x which affects mostly the intergranular region. We propose that the characteristic energy scale (T_{0J}) is related to the pinning strength due to the intergranular pinning force density resulting from the added BZO **[19, 43]**. It would be important to mention that we have used an exponential form of both $J_c(T)$ and $J_{cG}(T)$ to understand the vortex liquid state in the vicinity of T_c.

We have also used the average grain area (typically $\sim\mu^2$) for the determination of the granular current density, J_{cG}. Using the average grain area obtained from the analysis of SEM, we have extracted $J_{cG}(T)$. In **Figure**

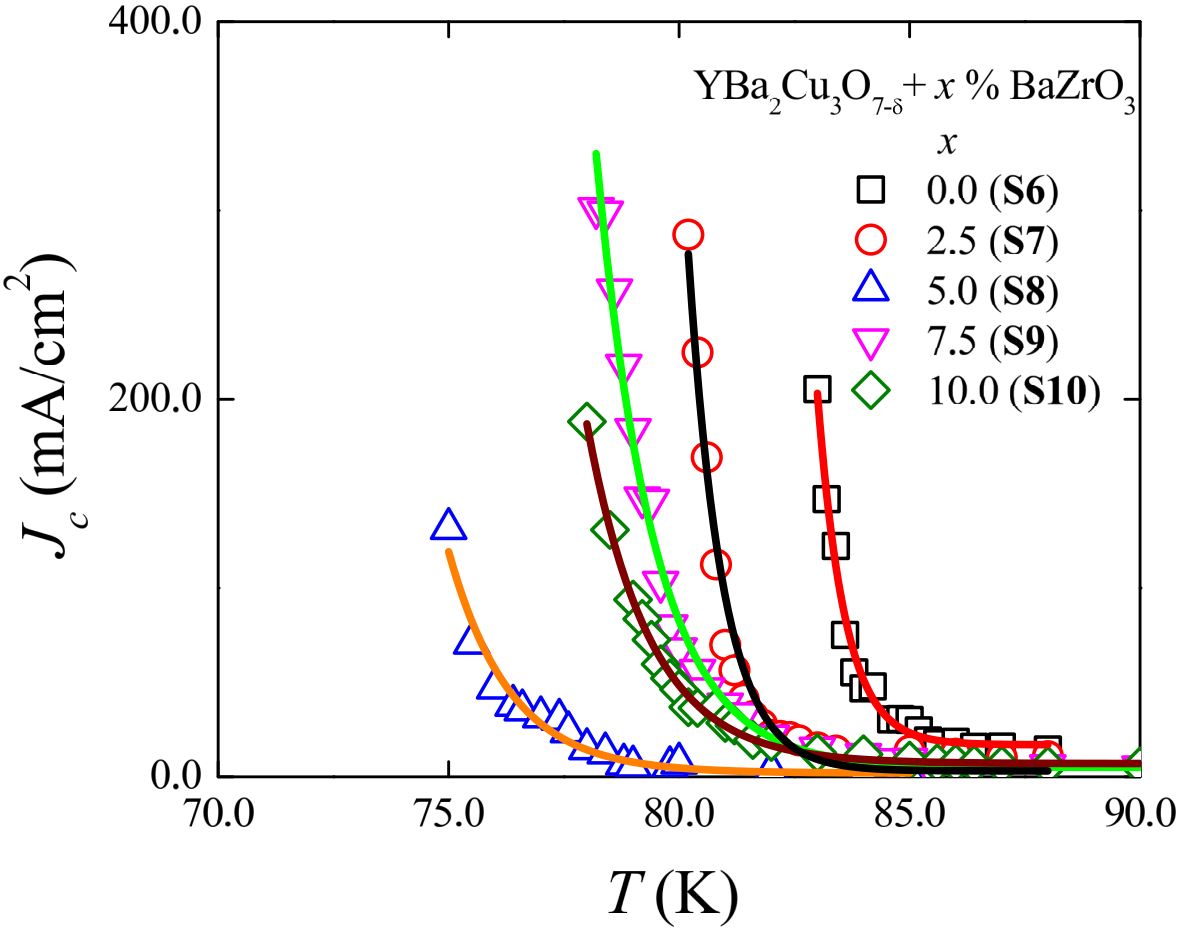

Figure 5.3.9: Critical current density (J_c) as a function of T for all samples with x = 0.0, 2.5, 5.0, 7.5 and 10.0. Solid lines are the exponential fitting.

5.3.10, we have shown $J_{cG}(T)$ for samples **S7** – **S10**. In the inset of **Figure 5.3.10**, we have also shown $J_{cG}(T)$ corresponding to the pure YBCO (**S6**). Clearly, J_{cG} is found to be very high in comparison to J_c. We have also observed a huge change in $J_{cG}(T)$ with the addition of the BZO in the intergranular region of YBCO. We added BZO in a similar YBCO to ensure any change in $J_{cG}(T)$ as a result of BZO. The enhancement of $J_{cG}(T)$ with x reveals that the vortex pinning is controlled from the intergranular BZO microparticles. We have also fitted $J_{cG}(T)$ by using the equation $J_{cG}(T) = J_{cG0} + J_{cG}(0)\exp(-T/T_{0JG})$. We have observed that $J_{cG0} << J_{cG}(0)$ in all samples and, therefore, an approximated equation is represented by $J_{cG}(T) \cong J_{cG}(0)$

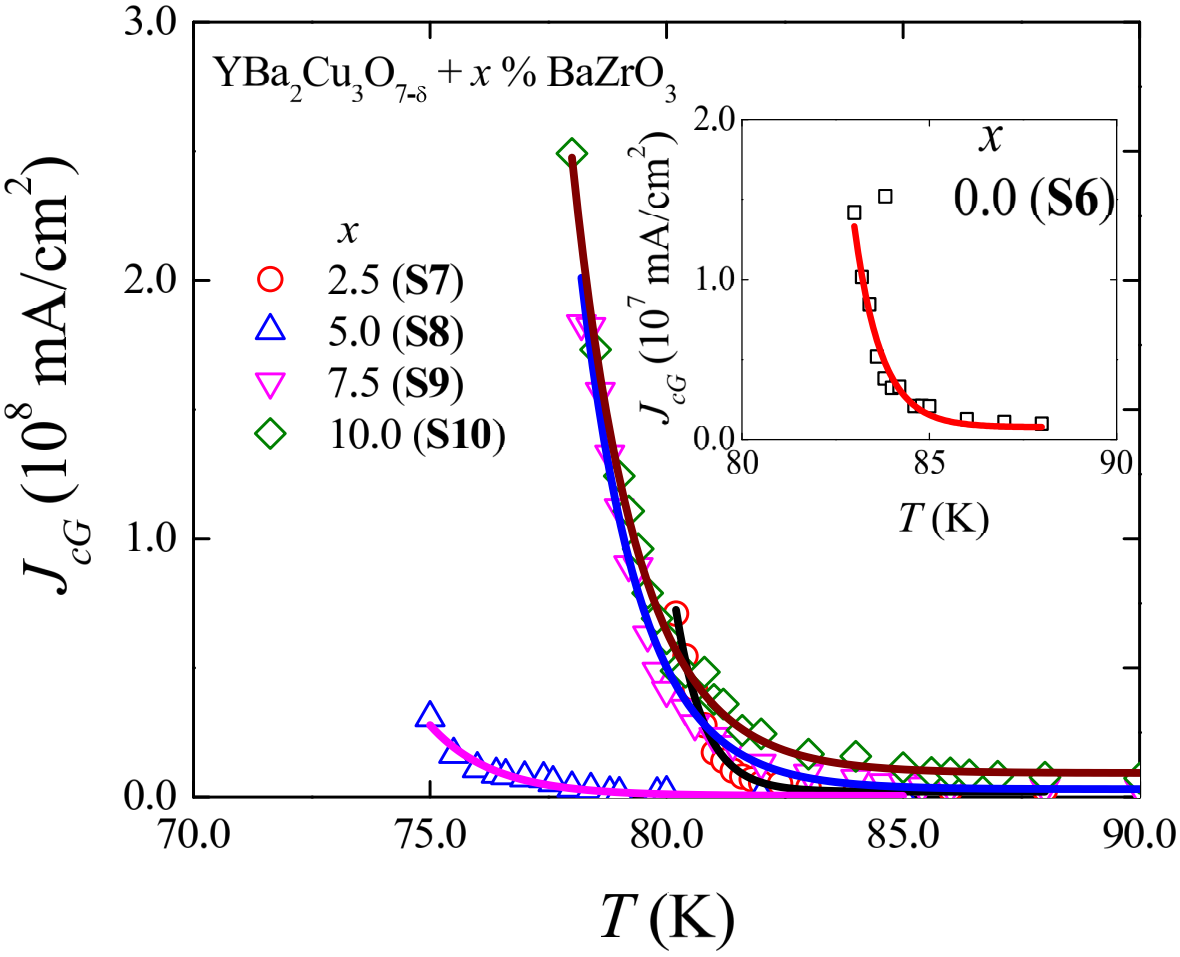

Figure 5.3.10: Critical current density (J_{cG}) as a function of T for samples with $x = 2.5$, 5.0, 7.5 and 10.0. In the inset, we have shown $J_{cG}(T)$ for YBCO ($x = 0.0$). Solid lines represent the exponential equation as given in the text

exp(-T/T_{0J}). In **Table 5.2**, we have given all fitting parameters of the critical current density, J_{cG}.

In bulk YBCO (**S6**), intrinsic point defects and the grain boundary together act as the pinning centers. For the **S7** – **S10** polycrystalline samples, grain boundary and BZO microparticles together act as the pinning network. Actually, the pinning of the line vortices by nanoparticles is really very effective in YBCO. However, the mechanism of pinning in such a scenario needs much more research. Line vortex pinning in YBCO by nanoparticles is not only due to matching of the size of the pinning centers with respect to the

coherence length. It is really a very complex process even though the length matching is very important to maximise current density. It is also known that grain boundaries are also very effective for the enhanced pinning even in the presence of the size mismatch (with respect to the coherence length$\sim$ few angstrom) and randomness [3, 44]. Therefore, if we modify the nature of the intergranular regions (whose size is typically $\sim$ micron) by adding microparticles, definitely the pinning is affected as it is observed in critical current density.

Table 5.3: Fitting parameters of the variable η

$x(\%)$	η_0	η_a	T_0(K)
0.0 (**S6**)	0.997	2.51×10^{47}	2.27
2.5 (**S7**)	1.00	3.38×10^{55}	0.63
5.0 (**S8**)	1.02	8.12×10^{18}	1.70
7.5 (**S9**)	1.00	1.14×10^{22}	1.51
10.0 (**S10**)	0.998	1.36×10^{27}	1.23

The nonlinear behavior of IV has been investigated by using an equation, $V = aI^{\eta}$ in which η is known to be an exponent. The nonlinear behavior of IV is revealed for $\eta > 1$. Following the idea of Kosterlitz-Thouless transition in superconducting systems, the existence of the dissociation of bound pairs has been confirmed by using IV characteristics [45, 46]. It is known that for the BKT transition, the exponent changes from $\eta = 1$ to $\eta = 3$ with the decrease in T. We have extracted η as a function of T for pure YBCO and all composite systems having BZO in the intergranular networks mostly. In **Figure 5.3.11**, we have shown $\eta(T)$ corresponding to $x = 0.0$, 2.5, 5.0, 7.5 and 10.0, respectively. Variations exhibit that the Kosterlitz-Thouless (KT)

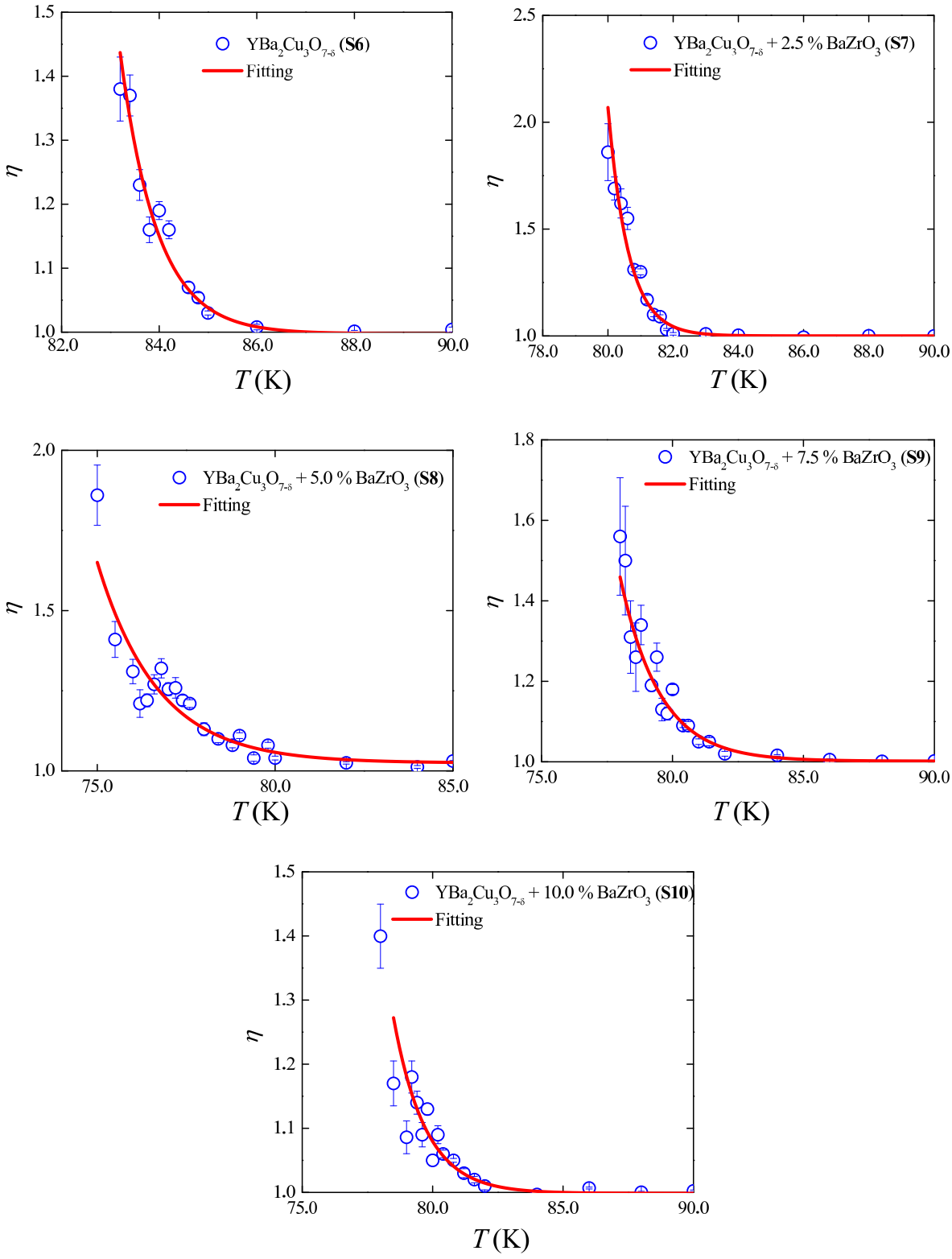

Figure 5.3.11: Variations of exponent η with the temperature of samples with x = 0.0, 2.5, 5.0, 7.5 and 10.0. Solid lines are the exponential ftting.

transition can be tuned in all samples (**S6 – S10**) at lower temperatures. We have fitted $\eta(T)$ using an equation in the form of $\eta(T) = \eta_0 + \eta_a \exp[-T/T_0]$, and all fitting numbers are listed in **Table 5.3**. The extrapolated high value of η_a reveals that the above formula has limitations of using it at much lower T ($T << T_c$). However, near T_c, the equation explains the behavior of $\eta(T)$ and it hints at the possibility of the KT transition. The characteristics temperature (T_0) representing an energy scale has been extracted as shown in **Table 5.3**. It will be interesting to observe that both energy scales (T_{0J} and T_0) are comparable. We attribute the comparable energy scale as the correlation of the presence of the superfluid density and the critical current density. In other words, near the critical temperature, the superfluid density strongly affects the variation of the critical current density.

By using the variation exponent $\eta(T)$ and following the AHNS model, we have extracted the superfluid phase stiffness (J_s) by using an equation, $J_s = [\eta - 1]T/\pi$ **[47 - 50]**. Within the superconducting phase transition region, the critical current density varies with T and the variation of the superfluid phase stiffness with T affects strongly the variation. In **Figure 5.3.12**, we have shown the variations of $J_s(T)$ for all samples. The superfluid density varies nonlinearly with T for all x values. The nonlinear variation of J_s has been observed in several other superconducting systems **[51]**. It will also be very interesting to compare J_s extracted by different methods. By using the mutual inductance technique (two-coil method), the real part of the voltage in the pick-up coil for the thin films of the overdoped cuprates is measured. A precision in the measurement of the London penetration depth is possible which is used for the determination of the SPS in two-coil methods **[1, 11]**.

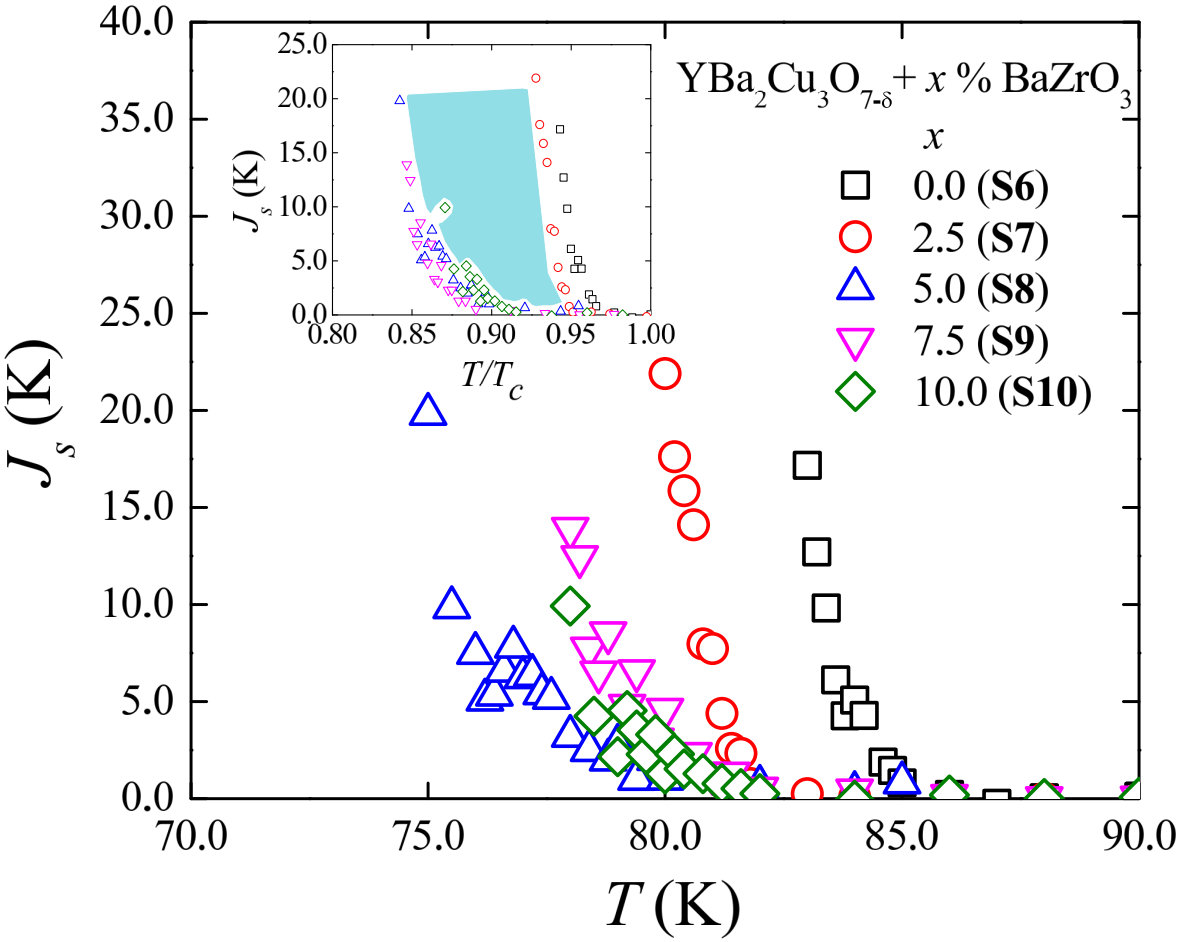

Figure 5.3.12: Variation of superfluid stiffness (J_s) with the temperature extracted by using the AHNS formula for x = 0.0, 2.5, 5.0, 7.5 and 10.0. In the inset, there is a constant J_s over a wide range of T for all samples with x = 0.0, 2.5, 5.0, 7.5 and 10.0 with a shaded region

In the *IV* method, the determination of the London penetration depth is not required and SPS can be extracted. SPS extracted by both methods reveals similar nonlinear behavior ($J_s(T)$) in different sample geometries. In the inset of **Figure 5.3.12**, we have shown J_s as a function of T/T_c which reveals that J_s is most sensitive to the lower concentration of BZO. However, the sensitivity gets reduced above x = 5.0. We have also observed a region shaded in the inset of **Figure 5.3.12** in which there is constant J_s over a wide range of T for different samples. It indicates that within a wide range of temperatures, there is a possibility to control the superfluid density in the presence of higher

concentration of BZO. Therefore, the presence of the BZO in the intergranular region may be responsible for affecting the superfluid density strongly in addition to the change in the pinning force density [52, 53].

The variations of T_c and J_s are not exactly having similar origins. So far, the SPS is concerned the phase gradient between two Cooper pairs matter whereas T_c is related with the onset of the pairing formation interactions. There is no direct experimental evidence on how the minimum oxygen inhomogeneity will affect the SPS. Dependence of SPS on weak oxygen inhomogeneity may be possible because it affects the pairing mechanism and T_c. In addition, adding BZO microparticles in the intergranular region of similar YBCO used for mixing BZO will dominate over weak intrinsic oxygen inhomogeneity from grain to grain. The variation of SPS from **S7** to **S10** is mostly controlled by the granular network including BZO microparticles. The change in the superfluid density ($\propto J_s$) in YBCO + BZO (**S7** – **S10**) with respect to that of the YBCO (**S6**) is affected by the modified Josephson region consisting of the intergranular network. Actually, the phase separation between any two grains gets affected by the modified intergranular networks and, therefore, the superfluid phase stiffness and hence the superfluid density change drastically. Any change in the superfluid density affects the critical current density (both $J_c(T)$ and $J_{cG}(T)$) in superconducting systems. Therefore, we attribute that the change in the critical current density in mixed systems can be attributed mostly to the change in the superfluid density through the Josephson region like intergranular networks consisting of even microparticles.

5.4 Summary

Using *IV* characteristics of superconducting systems consisting of YBCO and microparticles of BZO has been used successfully to extract the superfluid phase stiffness and critical current density. Controlling the SPS is observed by the microparticle residing in the Josephson junction-like intergranular regions. The addition of BZO microparticles in the intergranular region in YBCO superconductors affects the transport properties drastically in addition to the reduction in grain size. The variations of the critical current density with T are governed by the intergranular region as a result of the change in the superfluid density. There is a complex relation between the randomly controlled superfluid density and the temperature variation of the critical current densities.

5.5 References

1. G. Blatter, M. V. Feigelman, V. B. Geshkenbein, A. I. Larkin, V. M. Vinokur, Vortices in high-temperature superconductors, Rev. Mod. Phys. **66** (1994) 1125.

2. T. J. Haugan, T. Puig, K. Matsumoto, J. Wu, Supercond. Sci. Technol. **33** (2020) 040301.

3. H. Hilgelkamp, J. Mannhart, Rev. Mod. Phys. **74** (2002) 485.

4. M. Djupmyr, S. Soltan, H. -U. Habermeier, J. Albrecht, Phys. Rev. B **80** (2009) 184507.

5. T. Sk., A. K. Ghosh, J. Low Temp. Phys. **198** (2020) 224.

6. J. Gutiérrez, A. Llordés, J. Gázquez, M. Gibert, N. Romà, S. Ricart, A. Pomar, F. Sandiumenge, N. Mestres, T. Puig, X. Obradors, Nature Mater. **6** (2007) 367.

7. E. Bartolomé, A. Palau, A. Llordés, T. Puig, X. Obradors, Phys. Rev. **81** (2010) 184530.

8. P. Pahlke, M. Siege, R. Ottolinger, M. Lao, M. Eisterer, A. Meledin, G. V. Tendeloo, J. Hänisch, B. Holzapfel, L. Schultz,K. Lielsch, R. Huhne, Supercond. Sci. Technol. **31** (2018) 044007.

9. V. F. Solovyov, Q. Li, W. Si, B. Maiorov, T. J. Haugan, J. L. MacManus-Driscoll, H. Yao, Q. X. Jia, E. D. Specht, Phys. Rev. B **86** (2012) 094511.

10. B. Maiorov, S. A. Baily, H. Zhou, O. Ugurlu, J. A. Kennison, P. C. Dowden, T. G. Holesinger, S. R. Foltyn, L. Civale, Nature Mater. **8** (2009) 398.

11. I. Božović, X. He, J. Wu, A. T. Bollinger, Nature **536** (2016) 309.

12. I. Hetel, T. R. Lemberger, M. Randeria, Nature Phys. **3** (2007) 700.

13. N. R. Lee-Hone, J. S. Dodge, D. M. Broun, Phys. Rev. B **96** (2017) 024501.

14. A. Llordés, A. Palau, J. Gázquez, M. Coll, R. Vlad, A. Pomar, J. Arbiol, R. Guzmán, S. Ye, V. Rouco, F. Sandiumenge, S. Ricart, T. Puig, M. Varela, D. Chateigner, J. Vanacken, J. Gutiérrez, V. Moshchalkov, G. Deutscher, C. Magen, X. Obradors, Nature Mater. **11** (2012) 329.

15. J. L. Macmanus-Driscoll, S. R. Foltyn, Q. X. Jia, H. Wang, A. Serquis, L. Civale, B. Maiorov, M. E. Hawley, M. P. Maley, D. E. Peterson, Nature Mater. **3** (2004) 439.

16. G. Wang, M. J. Raine, D. P. Hampshire, Supercond. Sci. Technol. **30** (2017) 104001.

17. M. Peurla, H. Huhtinen, M. A. Shakhov, K. Traito, Yu. P. Stepanov, M. Safonchik, P. Paturi, Y. Y. Tse, R. Palai, R. Laiho, Phys. Rev. B **75** (2007) 184524.

18. E. Bartolomé, F. Vallés, A. Palau, V. Rouco, N. Pompeo, F. F. Balakirev, B. Maiorov, L. Civale, T. Puig, X. Obradors, E. Silva, Phys. Rev. B **100** (2019) 054502.

19. A. Xu, V. Braccini, J. Jaroszynski, Y. Xin, D. C. Larbalestier, Phys. Rev. B **86** (2012) 115416.

20. T. Horide, N. Matsukida, M. Ishimaru, R. Kita, S. Awaji, K. Matsumoto, Appl. Phys. Lett. **110** (2017) 052601.

21. P. Das, A. K. Ghosh, Physica C **548** (2018) 27.

22. T. Sk, A. K. Ghosh, AIP advances **10** (2020) 065117.

23. S. Mollah, B. Biswas, S. Haldar, A. K. Ghosh, Physica C **539** (2017) 40.

24. S. Haldar, P. Das, A. K. Ghosh, Physica C **563** (2019) 78.

25. I. Mukherjee, A. K. Ghosh, J. Supercond. Nov. Mag. **34** (2021) 365.

26. A. R. Bigansolli, T. G. da Cruz, F. R. de Souza Machado, D. Rodrigues Jr., Adv. Mater. Res. **975** (2014) 128.

27. R. Hauff, V. Breit, H. Claus, D. Hen-mann, A. Knierim, P. Sehweiss, H. Wüh, A. Erb, G. Mülller-Vogt, Phys. C **235–240** (1994) 1953.

28. T. B. Lindemer, J. F. Hunley, J. E. Gates, A. L. Sutton Jr., J. Brynestad, C. R. Hubbard, P. K. Gallagher, J. Am. Ceram. Soc. **72** (1989) 1775.

29. M. D. Vázquez-Navarro, A. Kuršumovic, J. E. Evetts, Supercond. Sci. Technol. **12** (1999) 1117.

30. B. A. Malik, M. A. Malik, K. Asokan, AIP Advances **6** (2016) 045317.

31. M. Safonchik, K. Traito, S. Tuominen, P. Paturi, H. Huhtinen, R. Laiho, Supercond. Sci. Technol. **22** (2009) 065006.

32. Y. Yeshurun, A. P. Malozemoff, Phys. Rev. Lett. **60** (1988) 2202.

33. M. Prester, Supercond. Sci. Technol. **11** (1998) 333.

34. J. Z. Wu, J. J. Shi, F. J. Baca, R. Emergo, J. Wilt, T. J. Haugan, Supercond. Sci. Technol. **28** (2015) 125009.

35. K. Traito, M. Peurla, H. Huhtinen, Yu. P. Stepanov, M. Safonchik, Y. Y. Tse, P. Paturi, R. Laiho, Phys. Rev. B **73** (2006) 224522.

36. N. P. Armitage, P. Foumier, R. L. Greene, Rev. Mod. Phys. **82** (2010) 2421.

37. Y. Matsuda, S. Komiyama, T. Onogi, T. Terashima, K. Shimura, Y. Bando, Phys. Rev. B **48** (1993) 10498.

38. P. G. Baity, X. Shi, Z. Shi, L. Benfatto, D. Popović, Phys. Rev. B **93** (2016) 024519.

39. D. P. Norton, D. H. Lowndes, Phys. Rev. B **48** (1993) 6460.

40. B. Biswas, A. K. Ghosh, J. Supercond. Nov. Mag. **33** (2020) 2629.

41. D. Rakshit, T. Sk., P. Das, S. Haldar, A. K. Ghosh, Physica C **588** (2021) 1353909.

42. V. Ambegaokar, A. Baratoff, Phys. Rev. Lett. **10** (1963) 486.

43. M. Miura, B. Maiorov, S. A. Baily, N. Haberkorn, J. O. Willis, K. Marken, T. Izumi, Y. Shiohara, L. Civale, Phys. Rev. B **83** (2011) 184519.

44. A. Palau, J. H. Durrell, J. L. MacManus-Driscoll, S. Harrington, T. Puig, F. Sandiumenge, X. Obradors, M. G. Blamire, Phys. Rev. Lett. **97** (2006) 257002.

45. J. M. Kosterlitz, D. J. Thouless, J. Phys. C **6** (1973) 1181.

46. V. L. Berezinskii, Zh. Eksp. Teor. Fiz. **61** (1971) 1144.; Sov. Phys. JETP **34** (1972) 610.

47. V. Ambegaokar, B. I. Halperin, D. R. Nelson, E. D. Siggia, Phys. Rev. Lett. **40** (1978) 783; Phys. Rev. B **21** (1980) 1806.

48. B. I. Halperin, D. R. Nelson, J. Low Temp. Phys. **36** (1979) 599.

49. D. R. Nelson, J. M. Kosterlitz, Phys. Rev. Lett. **39** (1977) 1201.

50. A. Andersson, J. Lidmar, Phys. Rev. B **87** (2013) 224506.

51. I. Božović, X. He, J. Wu, A. T. Bollinger, J Supercond. Nov. Mag. **31** (2018) 2683.

52. T. Haugan, P. N. Barnes, R. Wheeler, F. Meisenkothen, M. Sumption Nature **430** (2004) 867.

53. N. Haberkorn, M. Miura, J. Baca, B. Maiorov, I. Usov, P. Dowden, S. R. Foltyn, T. G. Holesinger, J. O. Willis, K. R. Marken, T. Izumi, Y. Shiohara, L. Civale, Phys. Rev. B **85** (2012) 174504.

Chapter 6

Insulating nanoparticle induced pinning in YBCO superconductor: crossover from collective to strong pinning regimes

6.1 Introduction

Controlling of vortices is possible both (i) from the granular region as well as (ii) from the intergranular region of the bulk superconductors. Technological aspects of the application of the superconductors at higher magnetic fields suggest that it is very important to control collective pinning and hence the motion of vortices from the remote positions, such as the inter-granular regions [1]. Improving critical current density by nanoparticles is an important area of research in the presence of Abrikosov vortices [2, 3]. There are several aspects of the pinning of vortices in superconductors by particles which generally act as pinning centers from outside the grains in bulk samples. In granular samples, microstructure affects nature and strength of pinning [4]. The collective pinning (CP) theory of Larkin and Ovchinnikov (LO) explains

how in-field critical current density in superconductors can be controlled by adjusting several features including the number density of the pinning centers [5]. Tuning size of pinning particles to enhance the pinning strength and current density has been studied thoroughly [6]. It will be also important to understand how the distribution and number density of insulating nanoparticles in the inter-granular region of the bulk YBCO superconductor affects the pinning scenarios of line vortices and other related properties. Several insulating inclusions in YBCO have been studied to enhance pinning [7, 8]. However, the enhancement of the magnetic critical current density is not universal. The optimization of T, H and the density of inclusions are very crucial and need more in-depth studies to maximize critical current density [9, 10].

We have studied transport critical current density as a function of temperature using current-voltage (IV) characteristics of several composite systems consisting of nanoparticles of BTO and YBCO superconductors. Granular natures of composite samples have been used to extract two different types of transport critical current densities (J_c and J_{cG}). Impacts of BTO nanoparticles in variations of J_c and J_{cG} have been studied. Magnetization (M) of (i) the pure YBCO and (ii) a composite system consisting of YBCO and 4.0% BTO have been studied to extract magnetic critical current density, J_{cm}, as a function of H at several temperatures below the critical temperature, T_c. Possible shifting of irreversibility (H-T) line has also been studied. We have studied the possible scenario of the collective pinning (CP) at the intermediate range of the field and it is shifting with the inclusion of BTO particles. Role of the temperature-dependent density of the pinning centers (n_p) within the framework of the LO theory for limited CP has been discussed. We have analyzed

J_{cm} (H) using an exponent to explore possible crossover to the strong pinning (SP) regime in the intermediate range of the field in both the pure and BTO nanoparticles added YBCO.

6.2 Experimental

Synthesis of bulk $YBa_2Cu_3O_{7-\delta}$(YBCO) superconducting samples has been carried out following the standard solid state reaction method **[11 - 13]**. Sintering of YBCO (x = 0.0) (**S11**) between 925 °C and 950 °C with two intermediate grindings are done before adding nanoparticles of $BaTiO_3$ (BTO). The maximum size of the added nanoparticles of the BTO is $\sim$ 100 nm. We have mixed four weight percentages, x = 2.0% (**S12**), 4.0% (**S13**), 8.0% (**S14**) and 16.0% (**S15**) of BTO with respect to the weight of the pure YBCO powder. Pressing composite powder of YBCO-BTO in the form of pellets the last sintering is done at 930 °C for 48 hours. Annealing of the pure and mixed samples has been carried out at 450 °C using uniform oxygen flow rate for a duration of 50 hours. Scanning electron microscope is for observing granular nature. Typical dimensions of the samples used for the transport measurements are 6.1 mm$\times$ 2.5 mm$\times$ 0.7 mm. Resistivity as a function of temperature has been measured using the standard four-probe method with the help of a cryogenerator (Janis, USA) **[14, 15]**. At several temperatures, IV measurements have been carried out below T_c. The range of the current used for IV measurements is 100.0 nA through 5.0 mA. Magnetization (M) as a function of magnetic field (H) has been measured at several temperatures below T_c in the field range 0 - 7.0 T using 7.0 T VSM (Cryogenics, USA).

6.3 Results and Discussions

We have shown the representative micrographs of the pure and BTO-mixed YBCO samples in **Figure 6.3.1**. Using the ImageJ software, we have extracted the average grain size (D) and variance (σ_D), as shown in **Figure 6.3.1**. We have considered several micrographs at different positions and magnifications for averaging the size of grains of each sample. The average size of grains in YBCO (**S11**) is observed to be 1.61$\pm$1.1 μm. Average size of grain changes weakly with the increase in x. D is found to be maximum 2.05$\pm$1.1 μm in **S13** (x = 4.0). However, D is found to be 1.75$\pm$0.88 μm in **S15** having the highest concentration (x = 16.0) of BTO. Therefore, no systematic increasing trend is observed in composite samples. Distribution of the inter-granular networks as revealed in SEM is random in all samples [16]. The granularity in the pure YBCO remains almost unchanged even after the increase in x. Even though insulating BTO particles with the maximum size of $\sim$ 100 nm have been mixed with the same bulk YBCO powder, no significant detection of insulating BTO particles has been possible in SEM most probably because of low density and insulating nature [17].

In **Figure 6.3.2**, we have shown the variation of the resistivity, ρ as a function of T. With the increase in x, ρ (300.0 K) increases with respect to ρ (300.0 K) of the pure YBCO. However, the maximum ρ (300.0 K) = 9.8 mΩ-cm is observed for x = 16.0. Therefore, insulating BTO nanoparticles added in the inter-granular region are not effective enough to transform the same into an insulator in nature. The inter-granular region of YBCO with BTO nanoparticles contributes a resistivity $\sim$ 2 to 8 mΩ-cm depending on x and

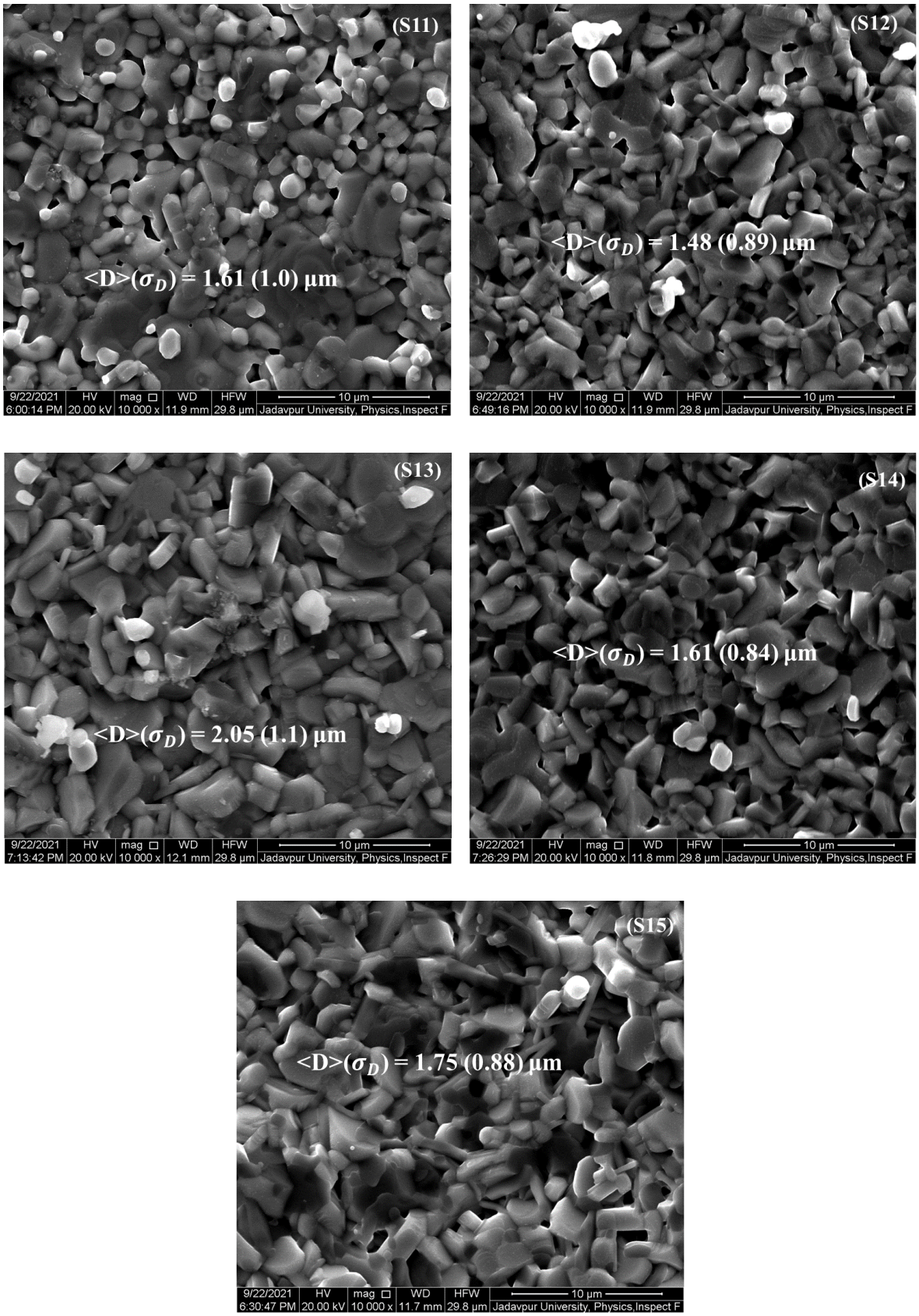

Figure 6.3.1: Scanning electron micrographs (SEM) of the pure YBCO (**S11**) and four composite systems consisting of YBCO and BTO (**S12**, **S13**, **S14** and **S15**). Inside each panel, the average grain size and respective standard deviation are given.

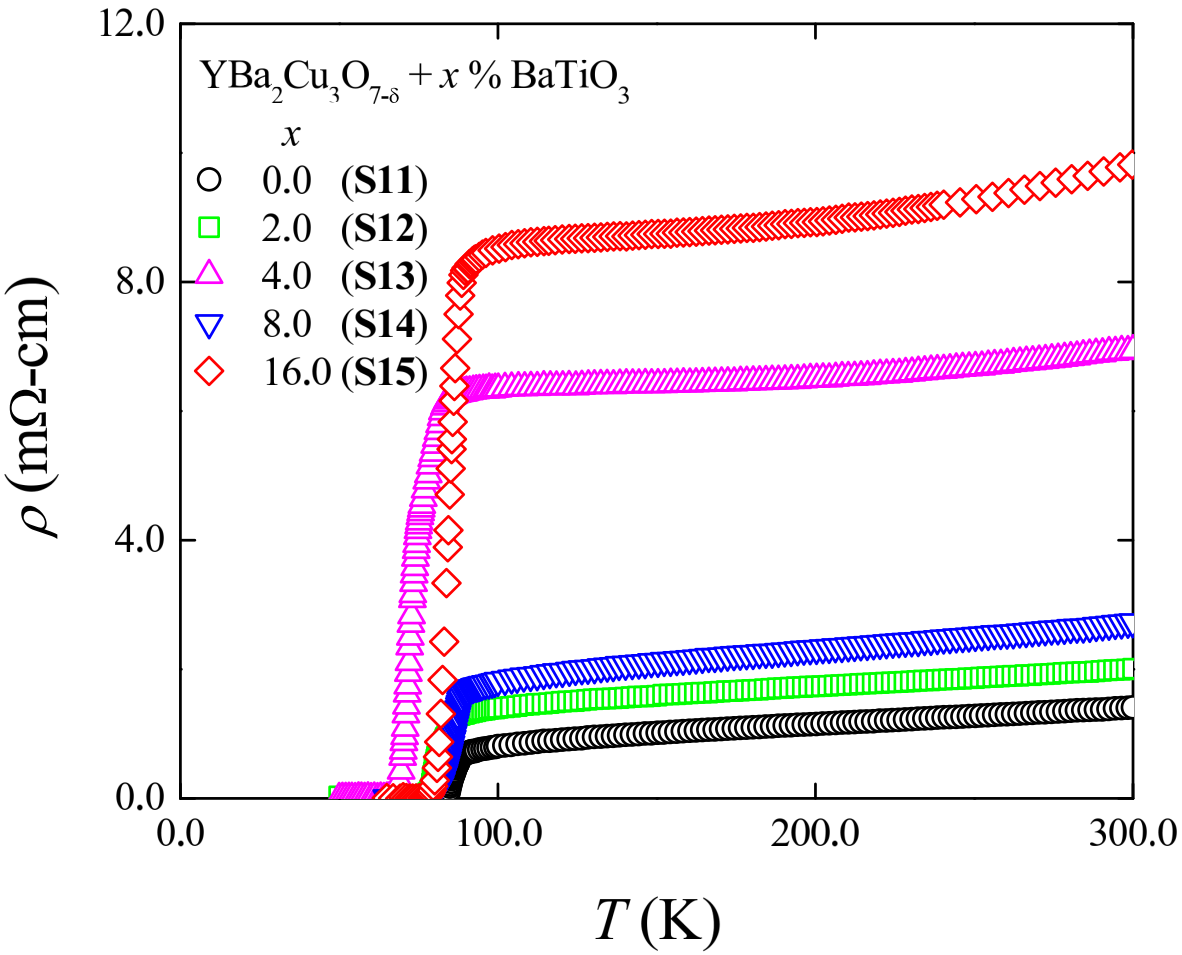

Figure 6.3.2: Resistivity as a function of T for the pure YBCO (**S11**) and four composite systems consisting of YBCO and BTO (**S12**, **S13**, **S14** and **S15**)

the normal state becomes a transformed metallic state with higher resistivity. A non-monotonic increase in the resistivity with the addition of iron-based oxide nanoparticles is also observed in several other hybrid systems **[18, 19]**.

In **Figure 6.3.3**, we have shown $d\rho/dT$ as a function of T corresponding to x = 0.0, 2.0, 4.0, 8.0 and 16.0, respectively. The onset critical temperatures (T_c) are found to be 90.0 K, 89.0 K, 87.0 K, 91.5 K and 90.0 K corresponding to x = 0.0, 2.0, 4.0, 8.0 and 16.0, respectively. The peak $d\rho/dT$ (T) is found to be relatively broadened in BTO mixed YBCO composites (**S12** - **S15**) in comparison with that of the pure sample (**S11**). Multiple peaks have been observed for **S12** and **S13** composite samples. Widths of phase transitions [T_c

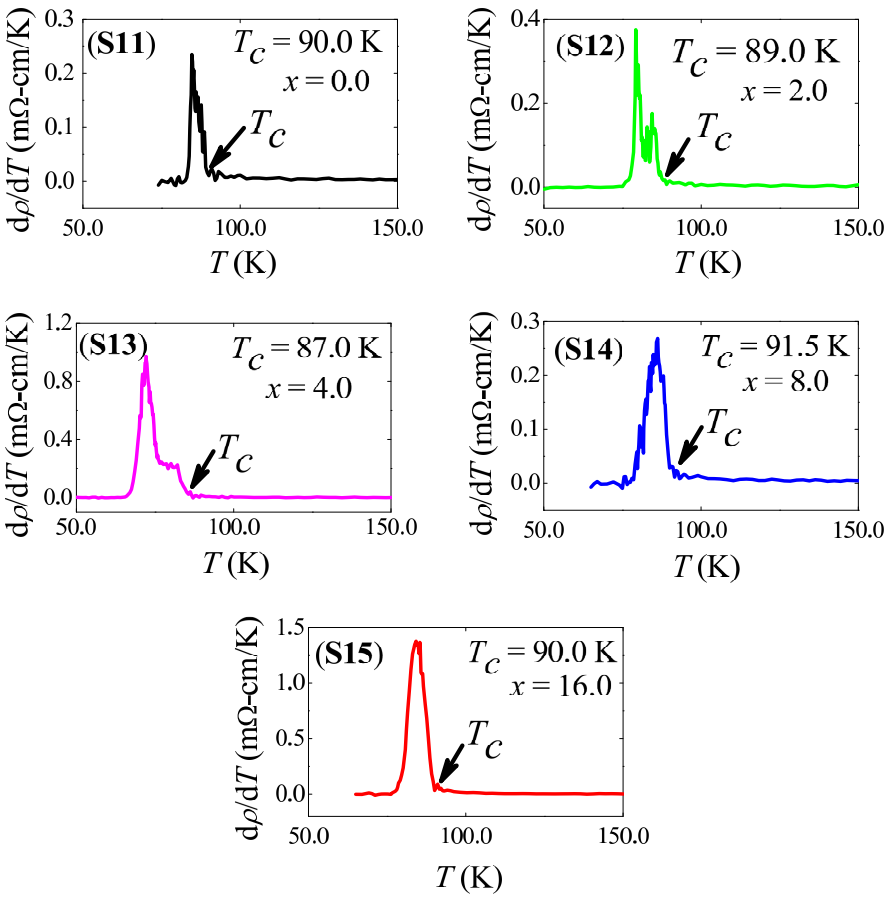

Figure 6.3.3: Plots of $d\rho/dT$ versus T for **S11** - **S15**. Onset critical temperatures (T_c) are shown by an arrow in each panel.

- T_c ($\rho \sim 0$)] are found to be 7.6 K, 14.0 K, 22.0 K, 14.0 K and 13.7 K for **S11**, **S12**, **S13**, **S14** and **S15**, respectively. Here, T_c is onset of superconducting transition and T_c ($\rho \sim 0$) is the temperature at which a superconducting state with $\rho \sim 0$ is attained. It reveals how the phase transition region gets strongly affected in composite samples. Inter-granular BTO affects the tunnelling of Cooper pairs between grains and hence associated changes are reflected in the broadening. A weak change in the onset T_c and broadened peak indicate that BTO nanoparticles reside in the inter-granular region without affecting the onset of the superconducting pair formation strongly even for the highest x **[20]**.

Current-voltage (IV) characteristics within a range of $T_c > T > T_c$ (~ 0)

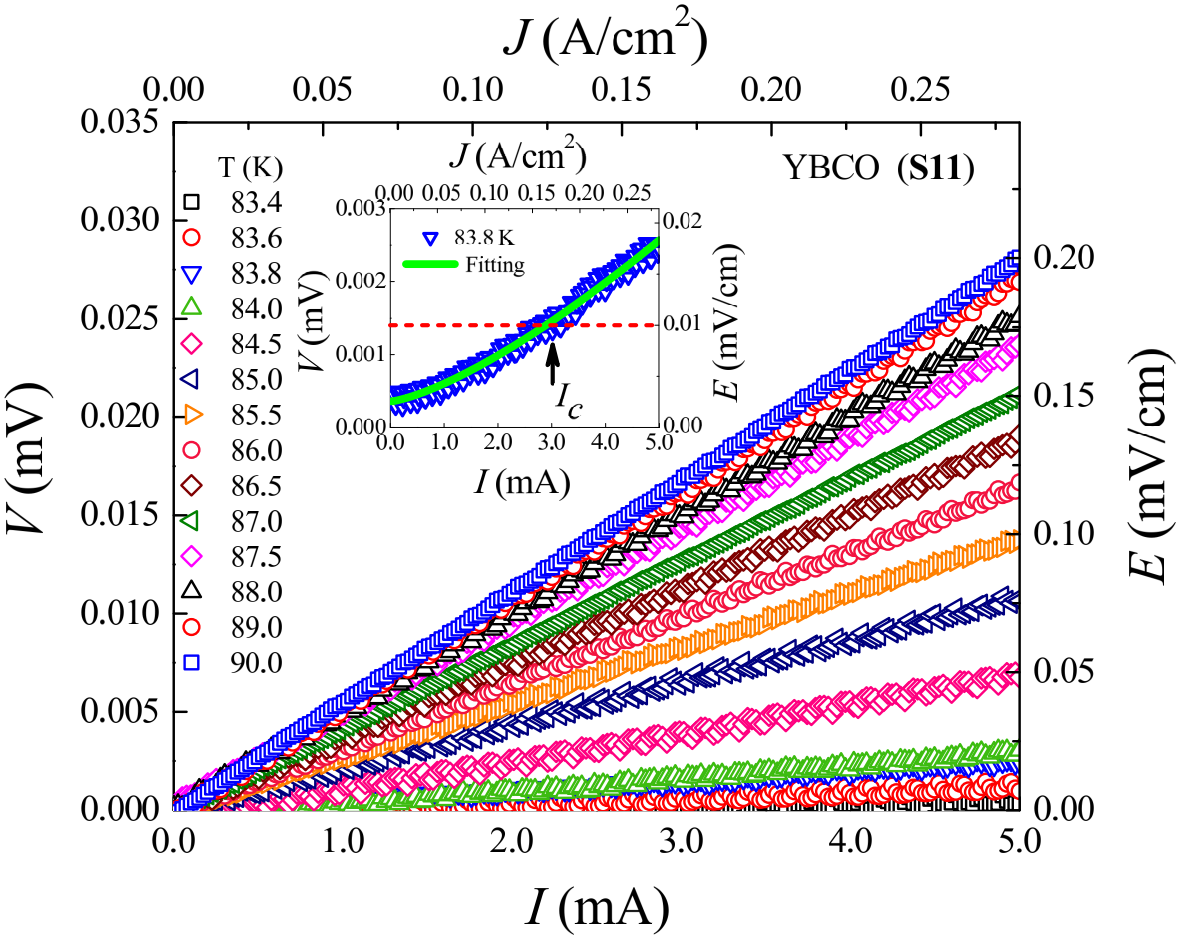

Figure 6.3.4: Current–voltage (IV) characteristics below critical temperature at zero magnetic field. In the inset, we have shown a typical IV curve and extraction procedure of I_c, critical current

for all the samples are shown in **Figure 6.3.4 - 6.3.8**. We have shown IV characteristics of the pure YBCO ($x = 0$) below T_c in **Figure 6.3.4**. Even at the lowest temperature of $T = 83.4$ K as shown in the inset of **Figure 6.3.4**, IV is found to be linear. In **Figure 6.3.5**, we have shown IV characteristics of **S12** with $x = 2.0$ in the range of $T = 77.6$ - 90.0 K. In **Figure 6.3.6**, we have shown IV characteristics of **S13** within the range of $T = 65.0$ K through 87.0 K. IV curves of **S14** with $x = 8.0$ are plotted in **Figure 6.3.7** in the range of 79.0 K through 90.0 K. The sample with the highest BTO concentration of $x = 16.0$ exhibits a linear behavior of IV in the range of 79.0 K through 90.0 K, as shown in **Figure 6.3.8**. Using the criterion $E =$

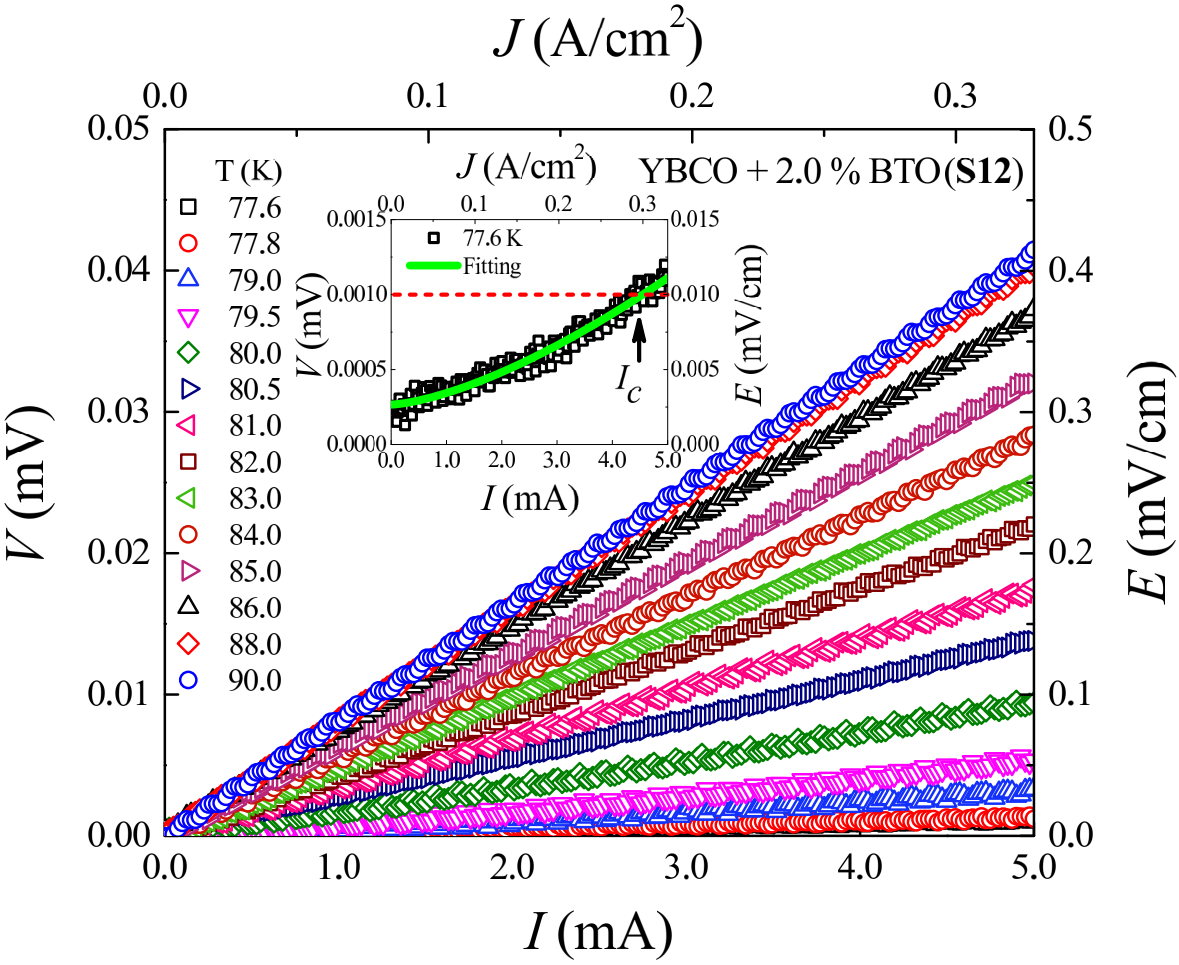

Figure 6.3.5: Current–voltage (IV) characteristics below critical temperature at zero magnetic field. In the inset, we have shown a typical IV curve and extraction procedure of I_c, critical current

0.01 mV/cm, we have extracted the transport critical current (I_c) as a function of T near T_c for all samples [21, 22]. Using an average area of an individual grain we have extracted granular critical current density, J_{cG}, and the total current density, J_c, has been obtained using the area of cross section of the sample. The granular critical current densities as a function of T are shown in **Figure 6.3.9**. In the inset $J_c(T)$s are also shown. Impact of BTO particles are observed in both J_c and J_{cG}, even though BTO nanoparticles are present in the inter-granular networks. Transport critical current density near T_c is, therefore, changed because of the change of the superfluid density as revealed

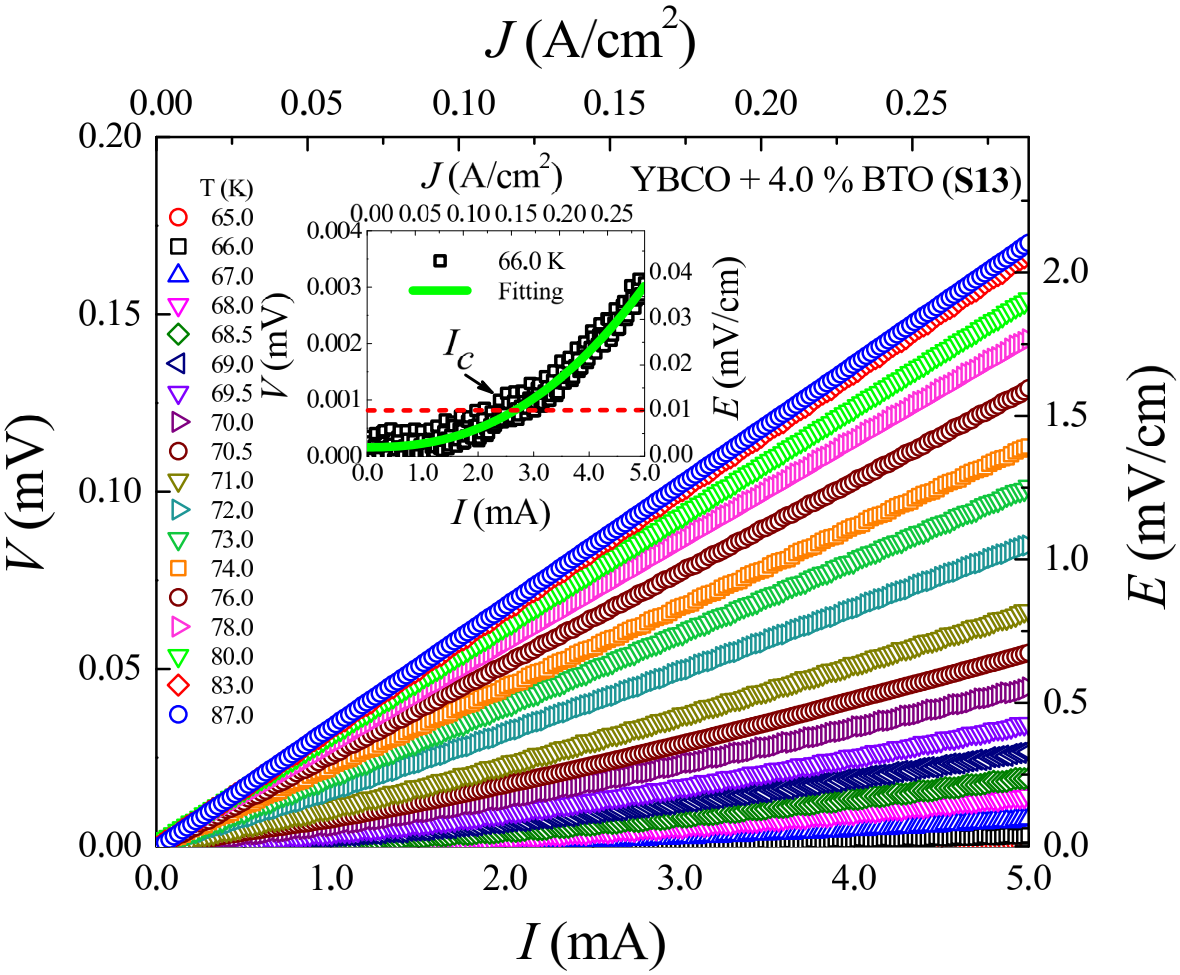

Figure 6.3.6: Current–voltage (IV) characteristics below critical temperature at zero magnetic field. In the inset, we have shown a typical IV curve and extraction procedure of I_c, critical current

by the nonlinear nature of the IV [23, 24].

We have selected (i) pure YBCO and (ii) a composite system consisting of YBCO and 4.0% BTO as a representative to make a rigorous study on the effect of inclusion of BTO in the intergranular region of the pure YBCO. In **Figure 6.3.10**, we have shown magnetization (M) as a function of the applied magnetic field (H) at several temperatures, T = 2.0 K, 4.2 K, 7.5 K, 10.0 K, 20.0 K, 30.0 K, 40.0 K, 50.0 K, 60.0 K, 65.0 K, 70.0 K, 80.0 K and 85.0 K for the pure YBCO. In the inset of **Figure 6.3.10**, magnified $M(H)$ for 60.0 K, 65.0 K, 70.0 K, 80.0 K and 85.0 K have also been shown.

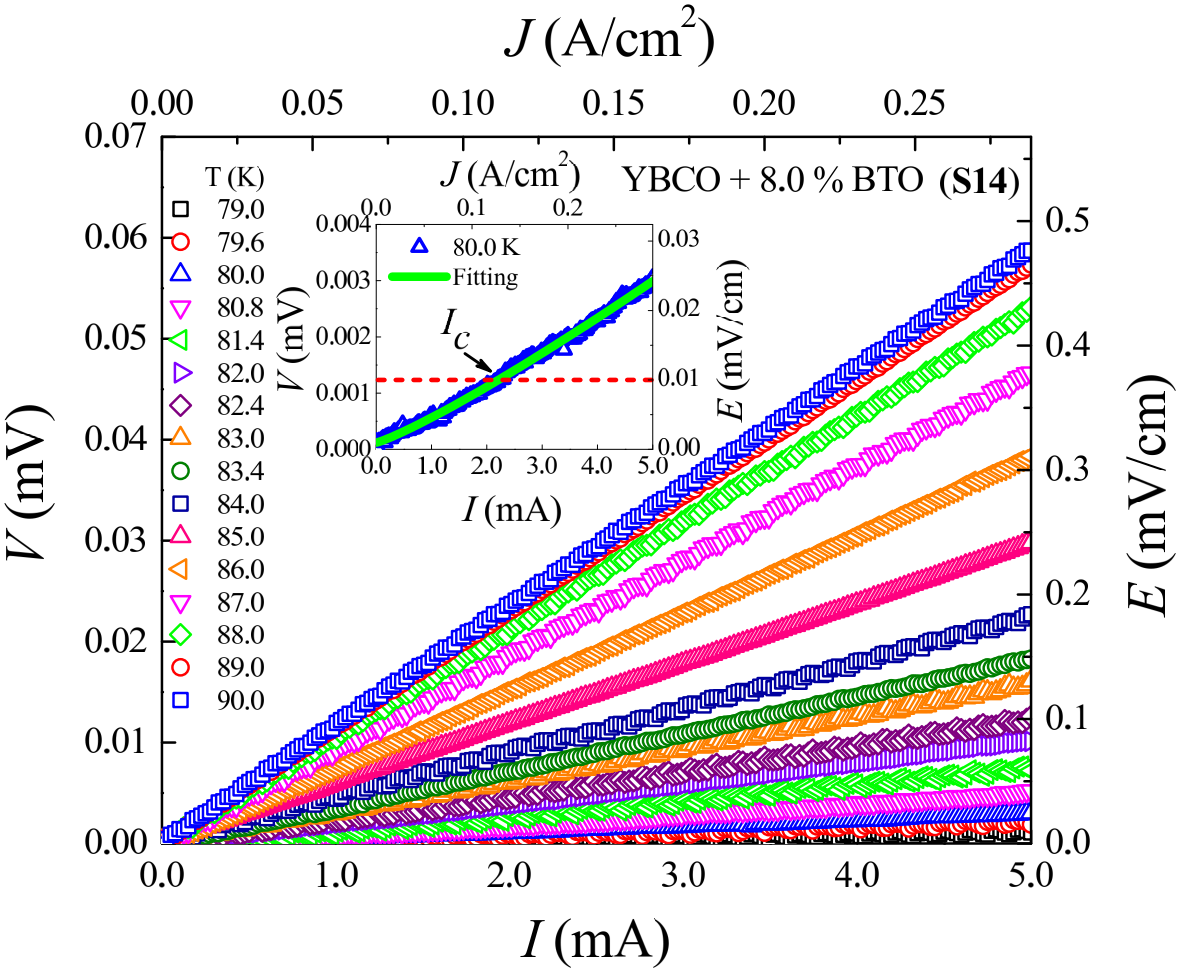

Figure 6.3.7: Current–voltage (IV) characteristics below critical temperature at zero magnetic field. In the inset, we have shown a typical IV curve and extraction procedure of I_c, critical current

$M(H)$ curves are shown up to a maximum magnetic field of 7.0 T and two different branches represent $M+$ and $M-$ corresponding to the increasing field 0 to +7.0 T and +7.0 T to 0, respectively. In **Figure 6.3.11**, we have shown irreversible magnetization, $\Delta M = M- - M+$ as a function of H for the same set of T **[25]**. Magnetic critical current density, J_{cm}, has been extracted using ΔM (H) with the help of the lateral dimension of bar-shaped YBCO sample **[26]**. We have shown J_{cm} (H) of YBCO in **Figure 6.3.12** using the log-log scale. The highest J_{cm} is 1.9× 10^5 A/cm^2 at T = 2.0 K and H = 0.158 T. With the increase in H the decrease in J_{cm} varies widely at different

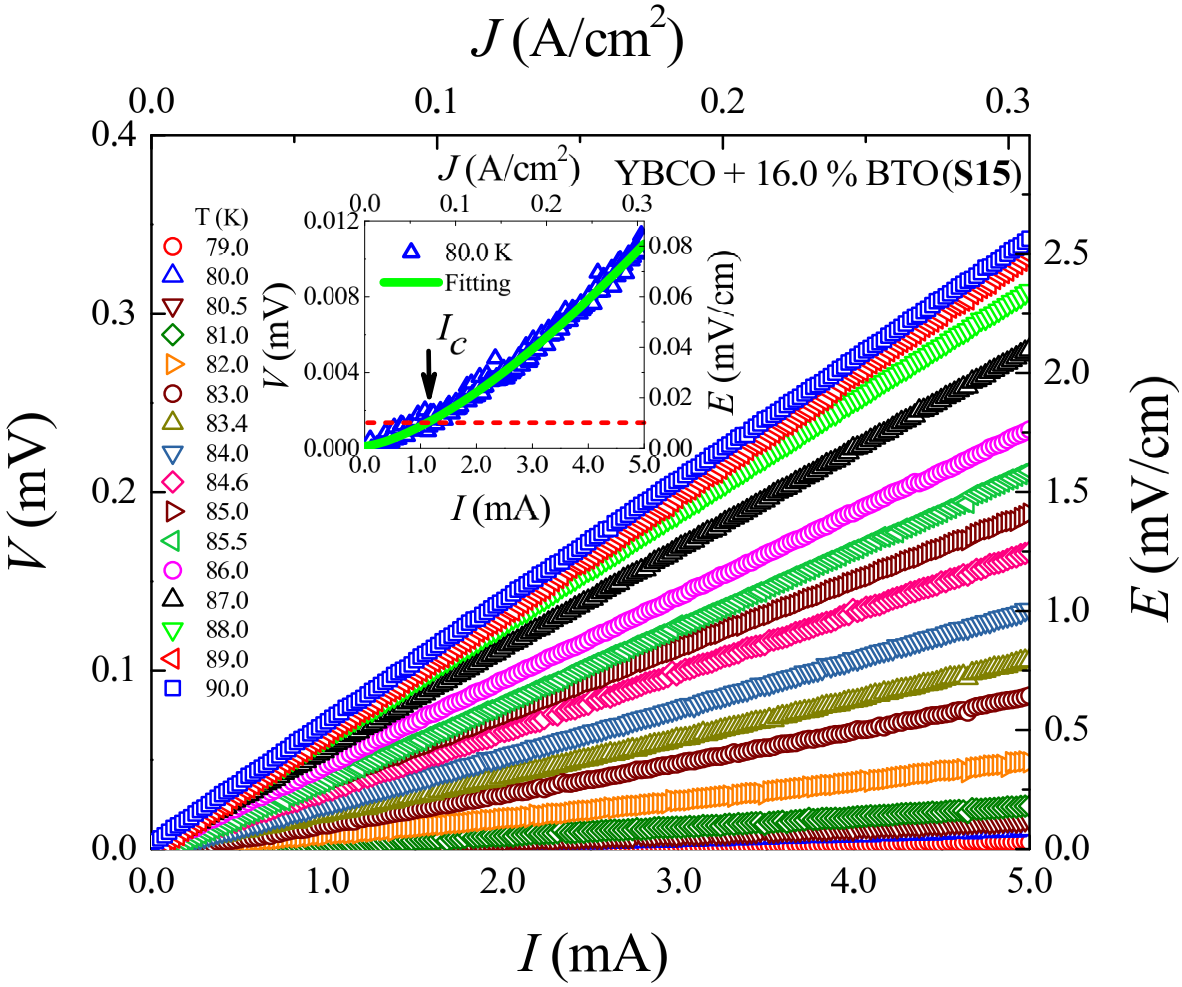

Figure 6.3.8: Current–voltage (IV) characteristics below critical temperature at zero magnetic field. In the inset, we have shown a typical IV curve and extraction procedure of I_c, critical current

ranges of T [27].

In **Figure 6.3.13**, we have shown $M(H)$ of composite consisting of 4.0% BTO and YBCO at several temperatures. The maximum M at 2.0 K is found to be highly reduced to ~ 20.98 emu/cm^3 in comparison with that of the pure YBCO which is ~ 41.74 emu/cm^3. Random orientations of moments of BTO nanoparticles are responsible for huge reduction of the M in **S13** sample. It will be interesting to mention that an increase in M is observed in iron-based oxide mixed YBCO superconductors at low-T regime [28]. Following a similar approach we have extracted ΔM (H), as shown in **Figure 6.3.14**

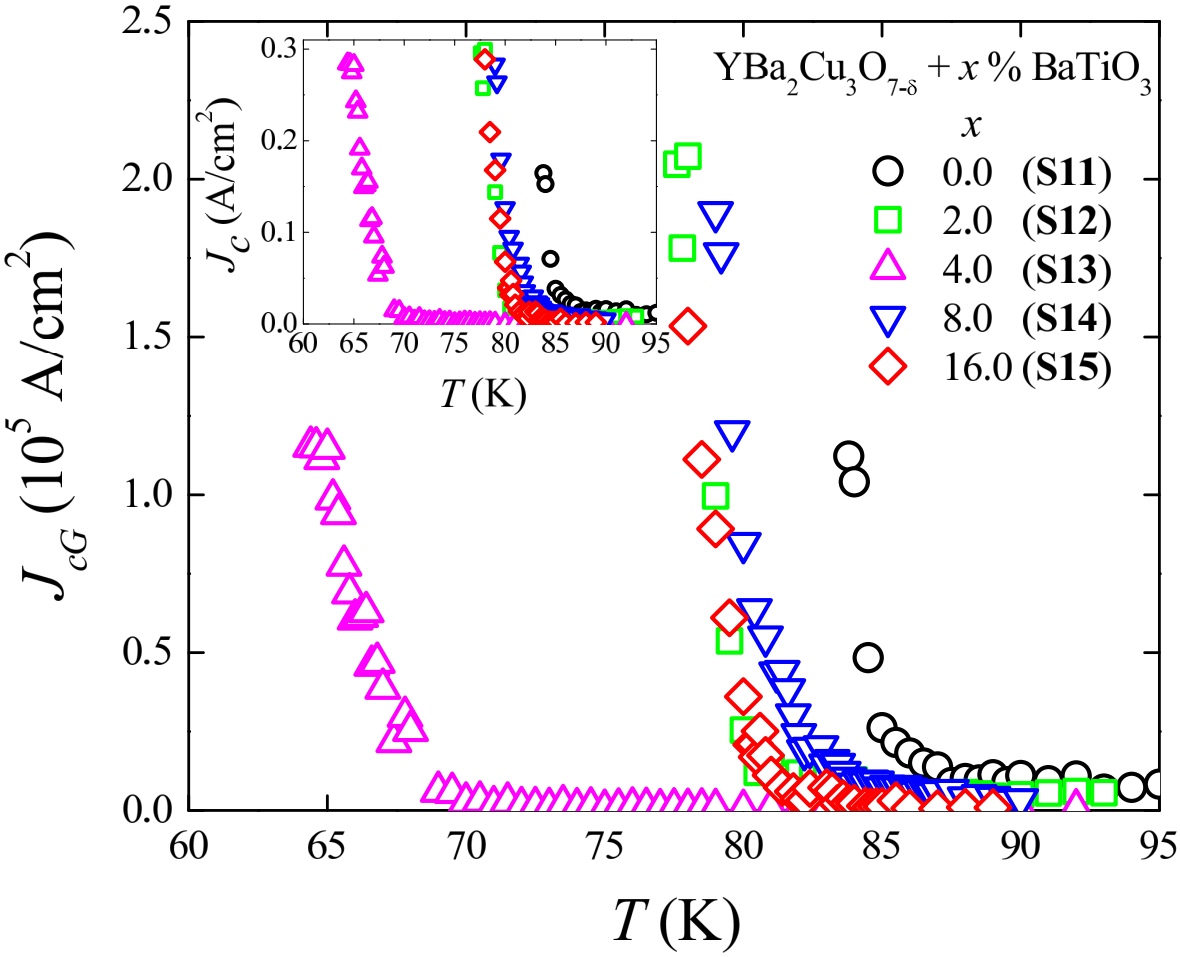

Figure 6.3.9: Variations of J_{cG} as a function of T. In the inset, $J_c(T)$ of all samples are shown.

which reveals suppression in ΔM at all T as a result of the addition of BTO in YBCO. In **Figure 6.3.15**, we have shown J_{cm} (H) of the composite of 4.0% BTO and YBCO in the log-log scale. We observed that a maximum J_{cm} (T = 2.0 K, H = 0.138 T) = 0.96× 10^5 A/cm^2. Clearly, J_{cm} has decreased strongly at 2.0 K and all other higher temperatures. Insulating nanoparticles of BTO are, therefore, not strong pinning centers in YBCO. Rather inter-granular insulating particles of size $\leq$ 100 nm may even weaken efficient pinning in several composite systems **[6, 29, 30]**.

We have extracted the irreversibility field, H_{irr}, obtained using a criterion of the lowest field at which, $\Delta M \sim 0$ emu/cm^3 **[31]**. In **Figure 6.3.16**, we have

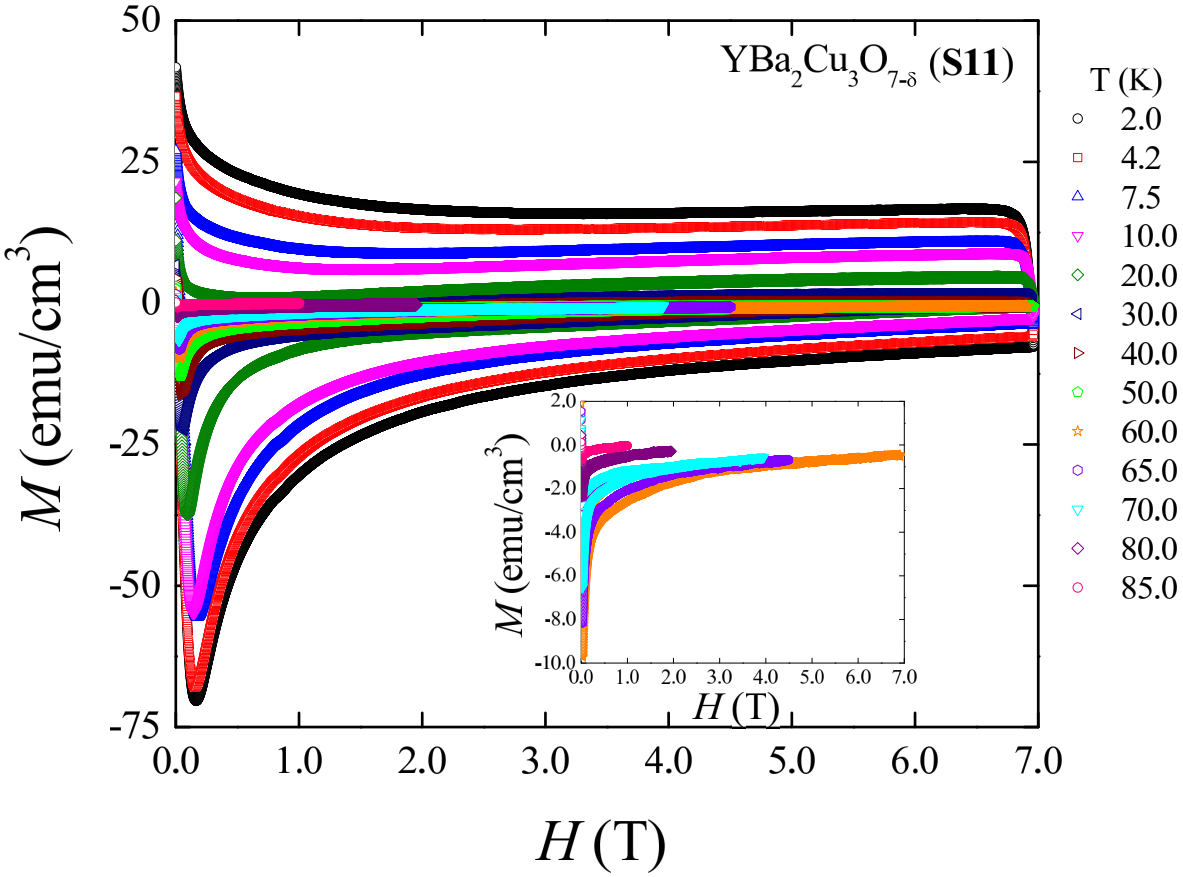

Figure 6.3.10: Magnetization (M) as a function of H of the pure YBCO (**S11**) at several temperatures. Inset shows few magnified $M(H)$ for 60.0 K, 65.0 K, 70.0 K, 80.0 K and 85.0 K.

shown nonlinear H_{irr} (T) phase diagrams for both samples **S11** and **S13**. At T = 60.0 K, we have observed that H_{irr} = 5.33 T and 2.28 T corresponding to **S11** and **S13**, respectively. It reveals that H_{irr} is strongly reduced by the addition of the BTO nanoparticles. Therefore, additional pinning centers induced by insulating nanoparticles in the inter-granular network of YBCO are opposing the expansion of the applicability of YBCO strongly. Optimizing the action of the pinning landscape associated with the added nanoparticles by distribution in higher T is also very important in addition to the size of the individual pinning particles. At a combination of intermediate T and intermediate H, a larger density of nanoparticles is known to be optimized for

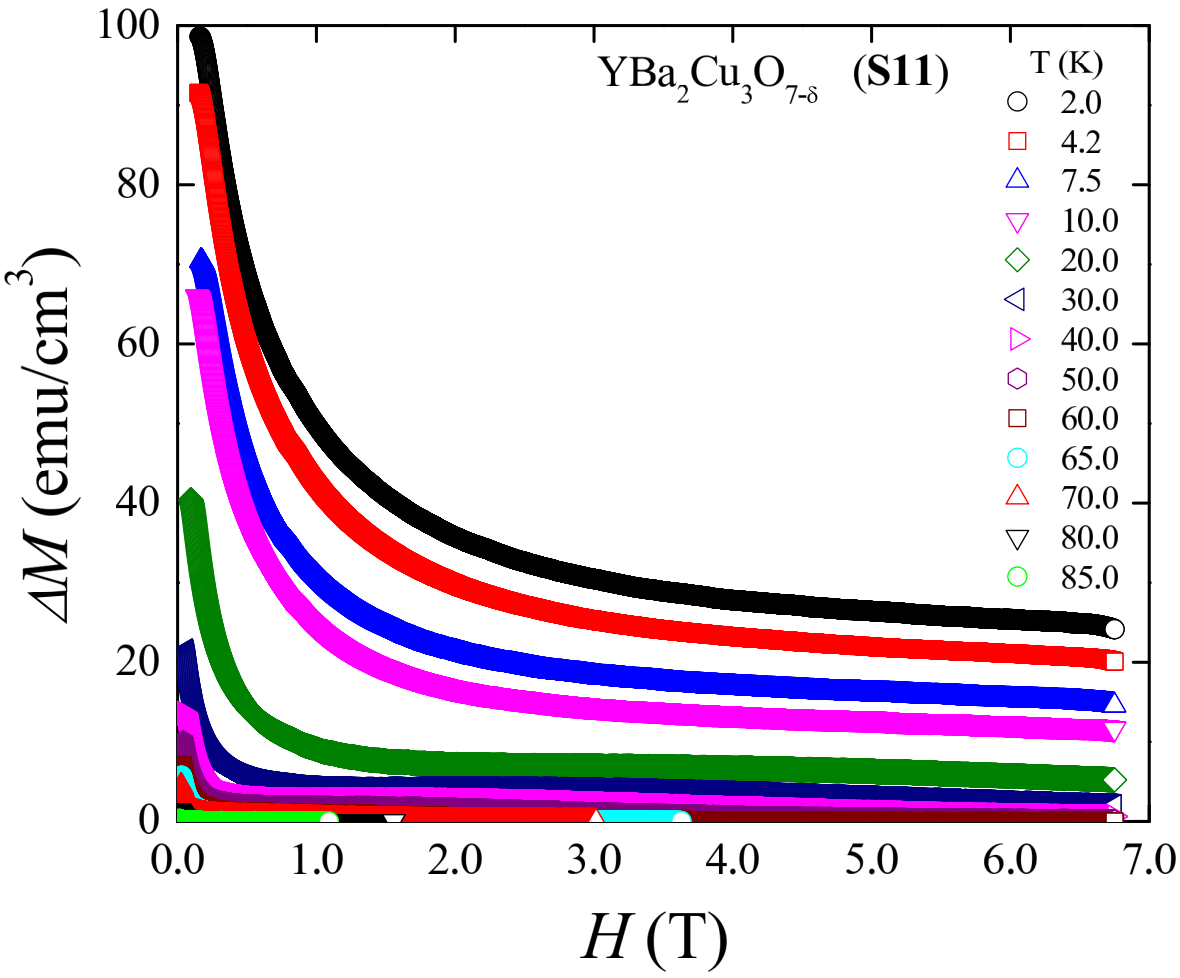

Figure 6.3.11: Irreversible magnetizations, ΔM, as a function of H for several T of **S11**.

getting enhanced pinning in YBCO [32].

The pinning force density, $F_p = |J_{cm}H|$ of both **S11** and **S13** samples are plotted in **Figure 6.3.17 - 6.3.18**, respectively. With the increase in H, F_p increases nonlinearly at all T. The growth of F_p with H is highly affected by the inclusions of BTO. Interestingly, even though the number of inter-granular pinning centers increases by the inclusion of BTO nanoparticles, the pinning force density decreases by an order of magnitude. The highest pinning force densities have been observed to be (i) F_p (2.0 K, 6.6 T) $\sim 3.16\times10^9$ N/m^3 and 1.45×10^9 N/m^3 for the pure and composite systems, respectively [33]. It will be interesting to mention that in YBCO thin film the maximum

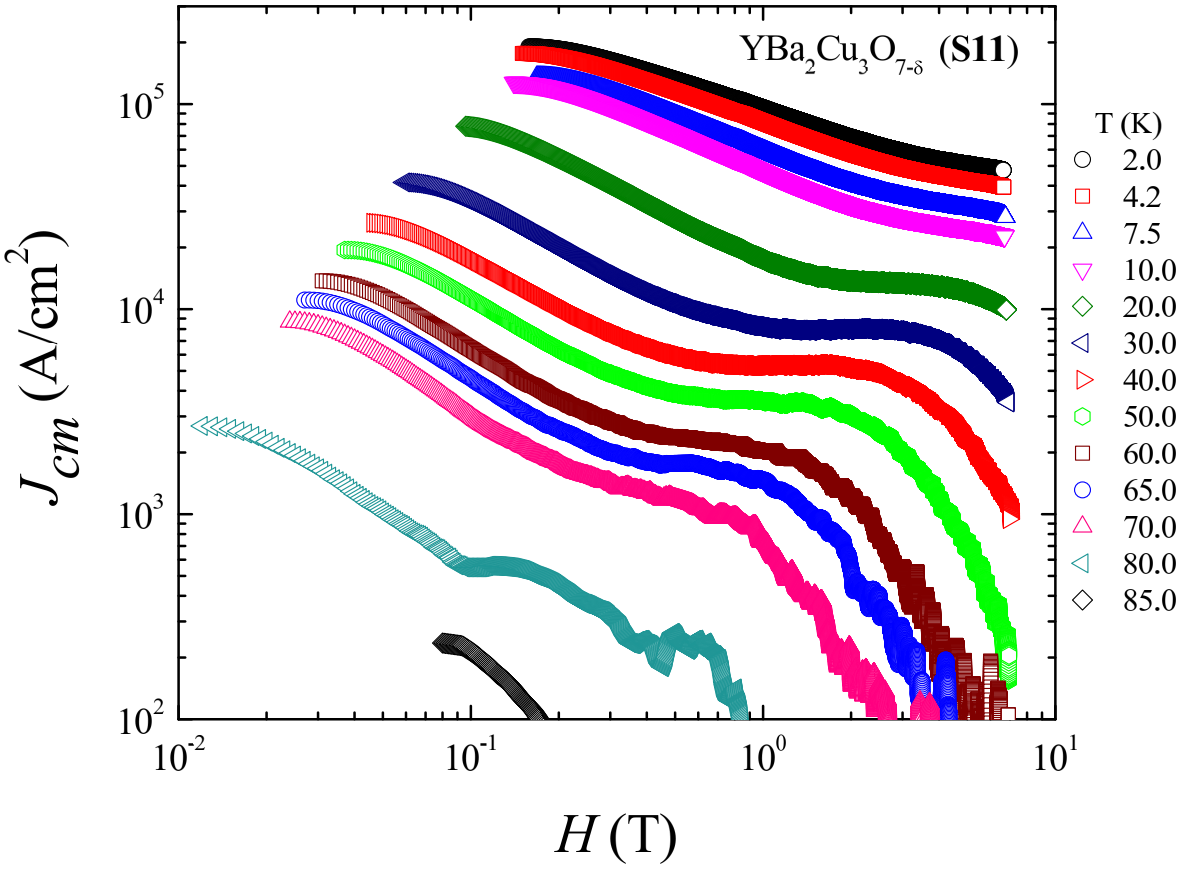

Figure 6.3.12: Magnetic critical current density, J_{cm}, as a function of H in the log-log scale of **S11** at several T as shown in the figure.

observed F_p (77.0 K, 2.0 T) is $\sim$ 21.0$\times$ 10^9 N/m^3 [34].

In **Figure 6.3.19**, we have shown J_{cm} as a function of $H^{-1/2}$ for T = 2.0 K, 4.2 K, 7.5 K and 10.0 K for both the (i) pure YBCO and (ii) BTO added YBCO [35]. In the intermediate range of field linear behavior of J_{cm} ($H^{-1/2}$) has been observed for both samples. A linear behavior in J_{cm} ($H^{-1/2}$) reveals how inter-vortex separation affects vortex pinning at a particular T. However, as shown by an arrow in J_{cm} ($H^{-1/2}$) there is a deviation from the linearity and saturation becomes visible at the lower range of H. As the field is increased the change in slope in J_{cm} ($H^{-1/2}$) is also visible. Therefore, a particular mechanism of pinning scenario in the intermediate field range persists even in the sample with BTO nanoparticles. The insulating BTO nanoparticles

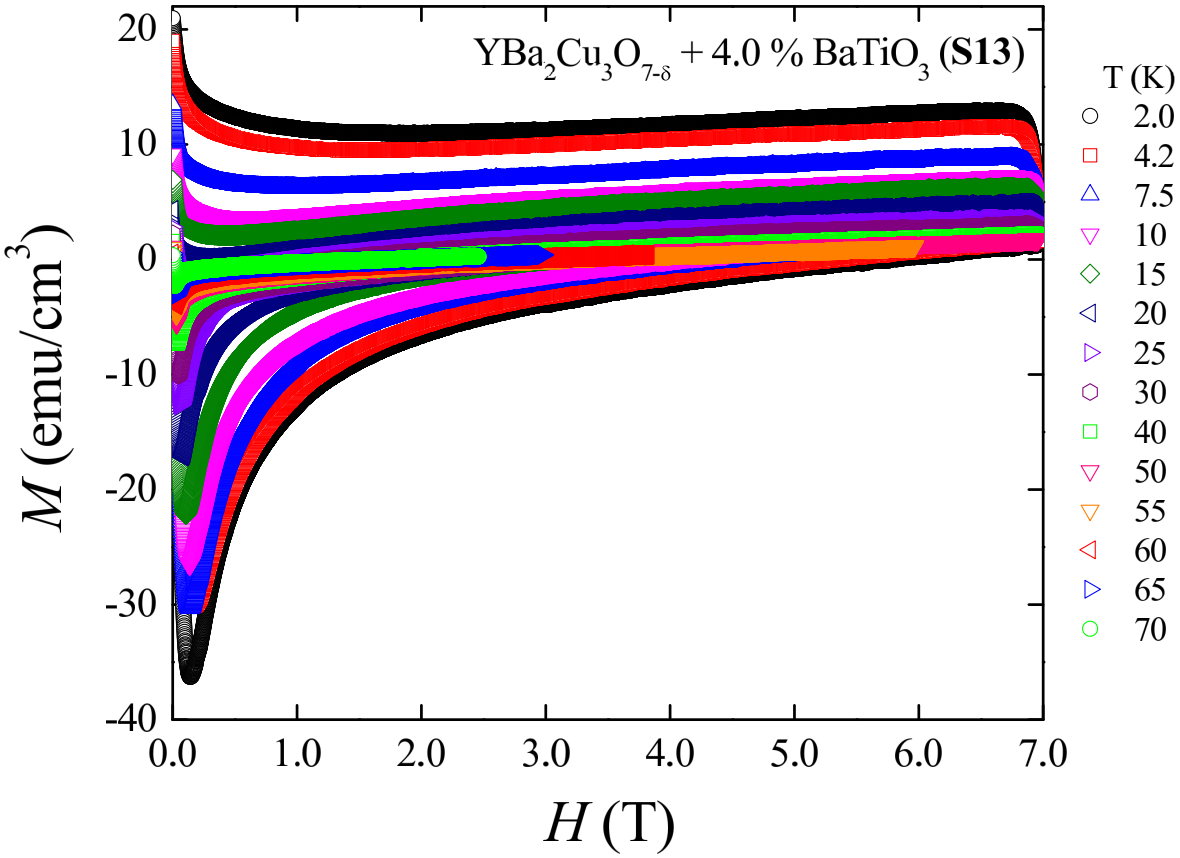

Figure 6.3.13: Magnetization (M) as a function of H of the composite sample **S13** at several temperatures.

affect collective pinning strength in such a way that J_{cm} decreases.

Almost a constant J_{cm} with $H^{-1/2}$ becomes more prominent in the BTO added YBCO sample. In **Figure 6.3.20**, we have also shown J_{cm} ($H^{-1/2}$) at 50.0 K, 60.0 K, 65.0 K and 70.0 K for both samples. A crossover between two different pinning regimes is found to be induced by the insulating BTO nanoparticles. Irradiation induced pinning centers are known to be effective in crossover between collective to single vortex pinning in cuprate superconductors [36]. In the pure YBCO single crystal, crossovers between different collective pinning regions have been observed [37]. Inter-vortex separation in such crossovers plays a crucial role. In the inset of **Figure 6.3.16**, we have shown possible crossover fields, H_{cr}, as a function of T for both samples. We

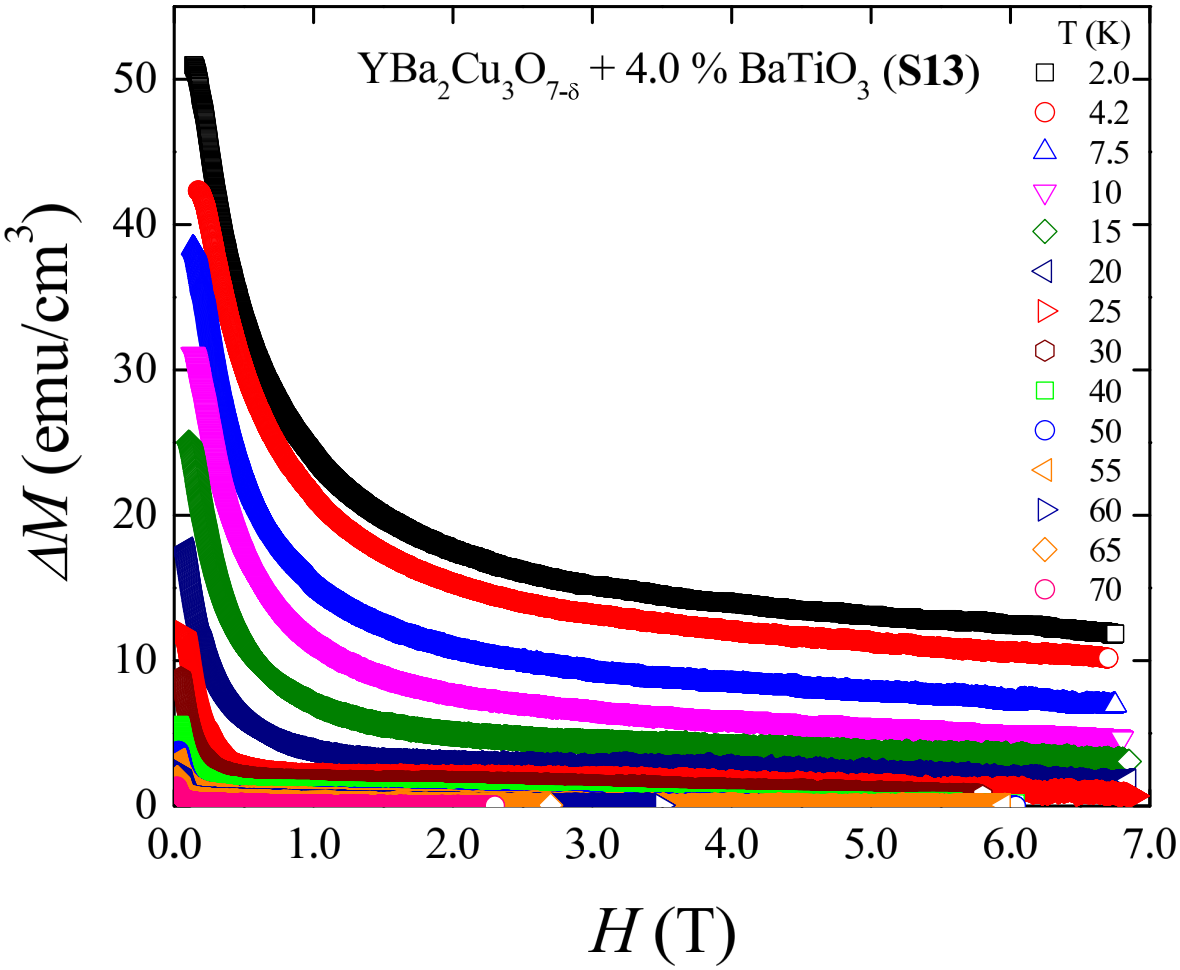

Figure 6.3.14: Irreversible magnetizations, ΔM, as a function of H for several T of **S13**.

found that there is a lower H at which inter-vortex spacing, $a_0 \propto H^{-1/2}$ induced change in the pinning mechanism is possible in presence of other constant factors controlling vortex dissipation. A nearly constant J_{cm} at lower H and all T may reflect that single vortex pinning regime is narrow in the pure YBCO. In presence of higher thermal fluctuations, crossover in vortex pinning also becomes more prominent in presence of the BTO nanoparticles. In addition, additional insulating BTO nanoparticles may extend lower field pinning mechanisms [32]. However, since inter-vortex separation is one of the crucial factors in analyzing any crossover between pinning mechanisms, we need to understand the exact nature of the pinning in a particular combination

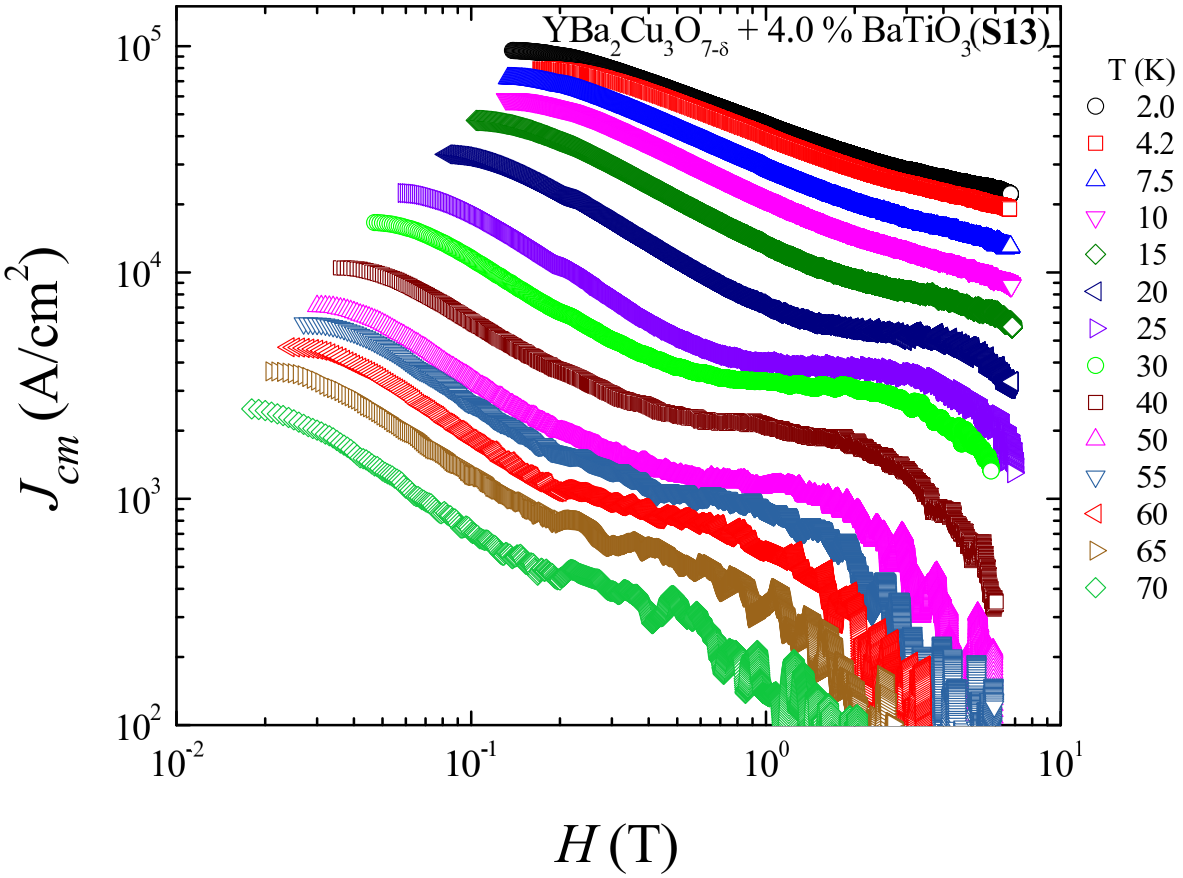

Figure 6.3.15: Magnetic critical current density, J_{cm}, as a function of H in the log-log scale at several T of **S13**.

of T, H and pinning landscapes.

We have made an attempt to understand how pinning scenarios as a result of the presence of randomly distributed BTO nanoparticles in YBCO may act. Within the framework of one of the collective pinning regimes, J_{cm} = A exp[-$(m/n_p)H^{1.5}$], where A and m are two constants [38]. n_p is the density of pinning centers. In **Figure 6.3.21 - 6.3.22**, we have plotted ln(J_{cm}) as a function of $H^{3/2}$. There are at least two regions (in H) in which a linear fitting can be used to extract the slope of the variation m/n_p at different temperatures. At T = 2.0 K, a linear variation in ln(J_{cm}) versus $H^{3/2}$ plot is observed up to $\sim$ 1.2 T and the range is sensitive to T. The slope of the linear variation is roughly related to the density pinning centers, n_p. In **Figure 6.3.23**, we

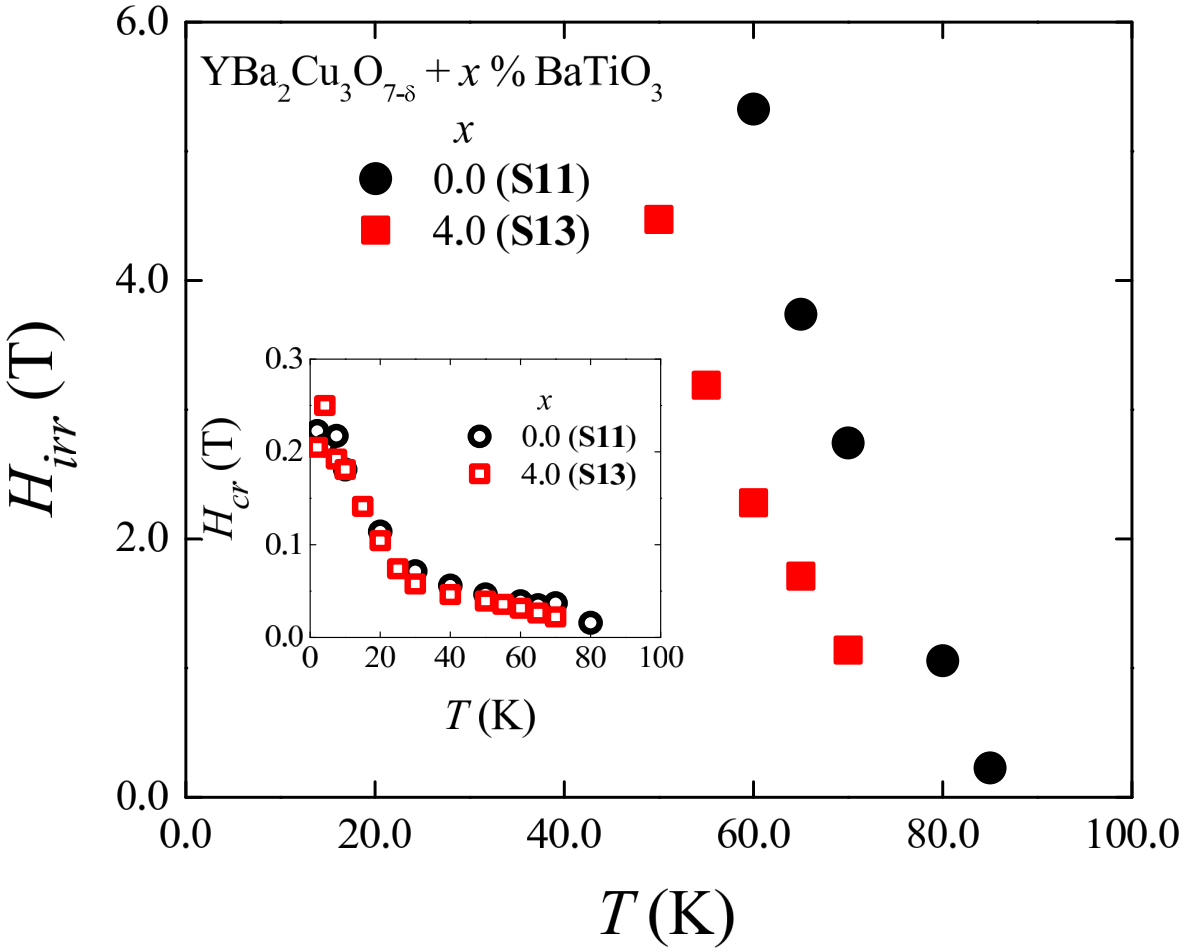

Figure 6.3.16: Irreversibility field-temperature, $H_{irr}(T)$, phase diagram of **S11** and **S13**. In the inset, possible crossover fields, H_{cr} (T), based on J_{cm} versus $H^{-1/2}$ plots for **S11** and **S13** samples

have shown m/n_p with T for **S11** and **S13**. With the increase in T decrease in n_p is observed assuming m is independent of T for both samples. However, above $T \sim 30.0$ K, the densities of pinning centers are found to be very different. Therefore, in a limited intermediate range of H, pinning centers induced by BTO nanoparticles affect collective pinning strongly. However, with the increase in T a noticeable change in the collective pinning mechanism has been observed in both (**S11** and **S13**) samples. In addition, it will be interesting to mention that following a crossover as revealed by the variation of intervortex separation (J_{cm} versus $H^{-1/2}$ plots) does not match with

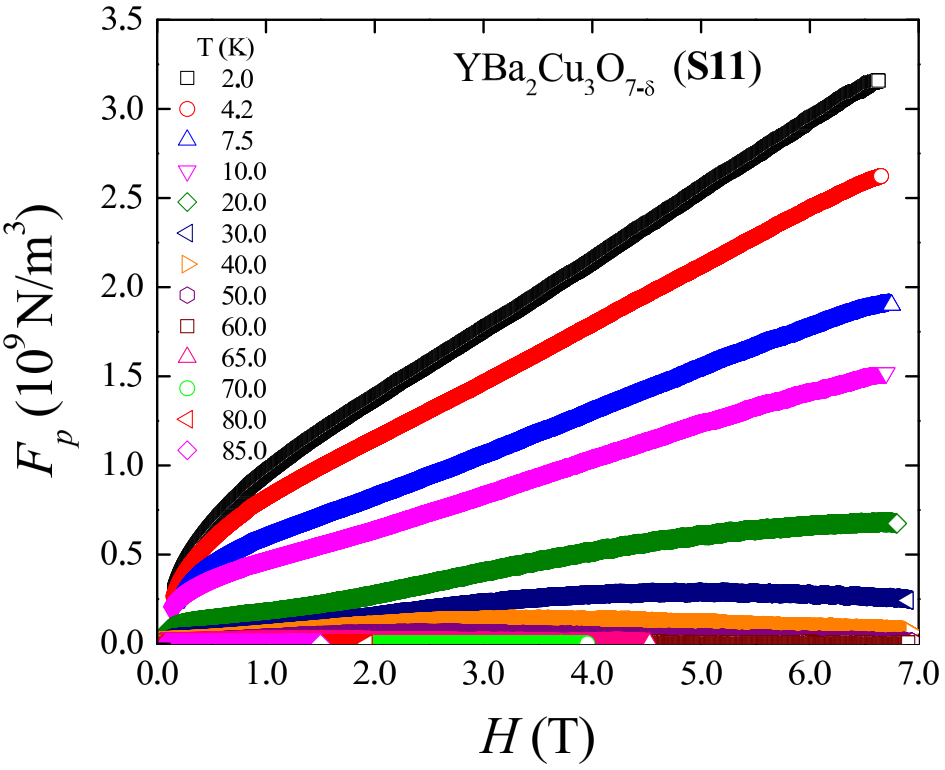

Figure 6.3.17: Pinning force density (F_p) as a function of H of **S11** in the range of 2.0 - 85.0 K

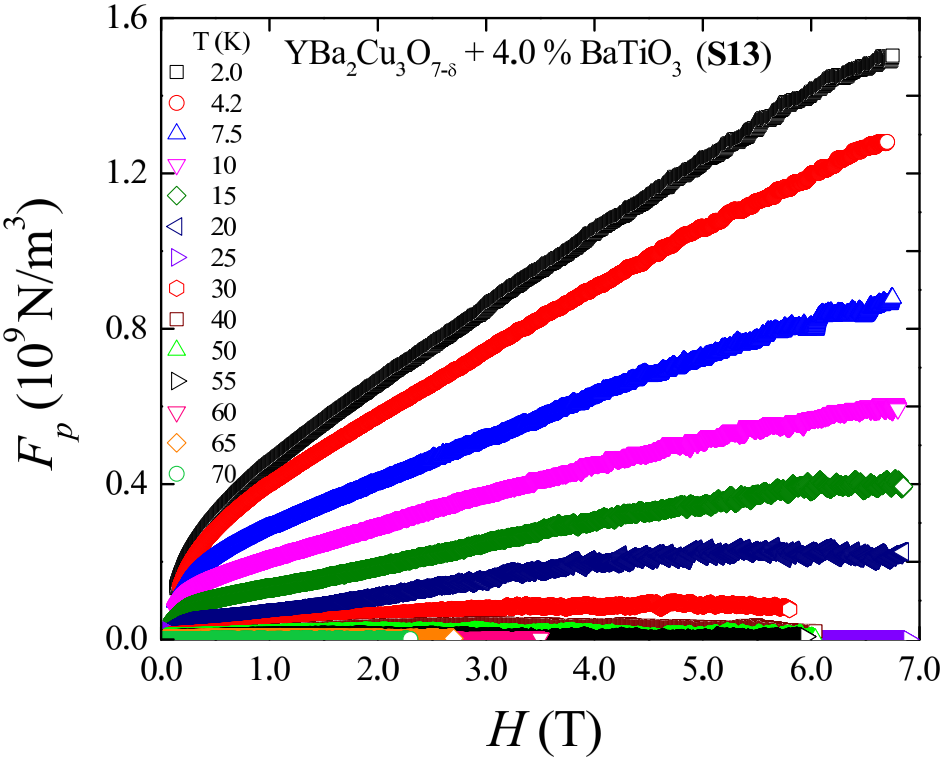

Figure 6.3.18: Pinning force density (F_p) as a function of H of **S13** in the range of 2.0 - 70.0 K.

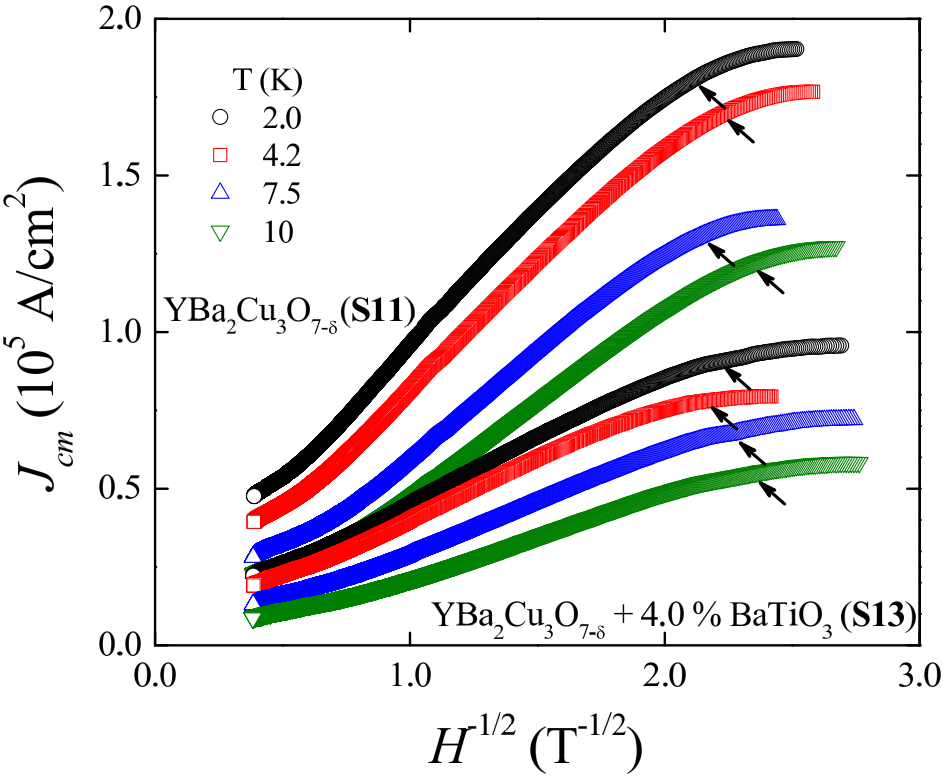

Figure 6.3.19: Magnetic critical current density, J_{cm}, as a function of $H^{-1/2}$ for **S11** and **S13** for lower temperatures. Arrows are shown to show possible crossover field, H_{cr}.

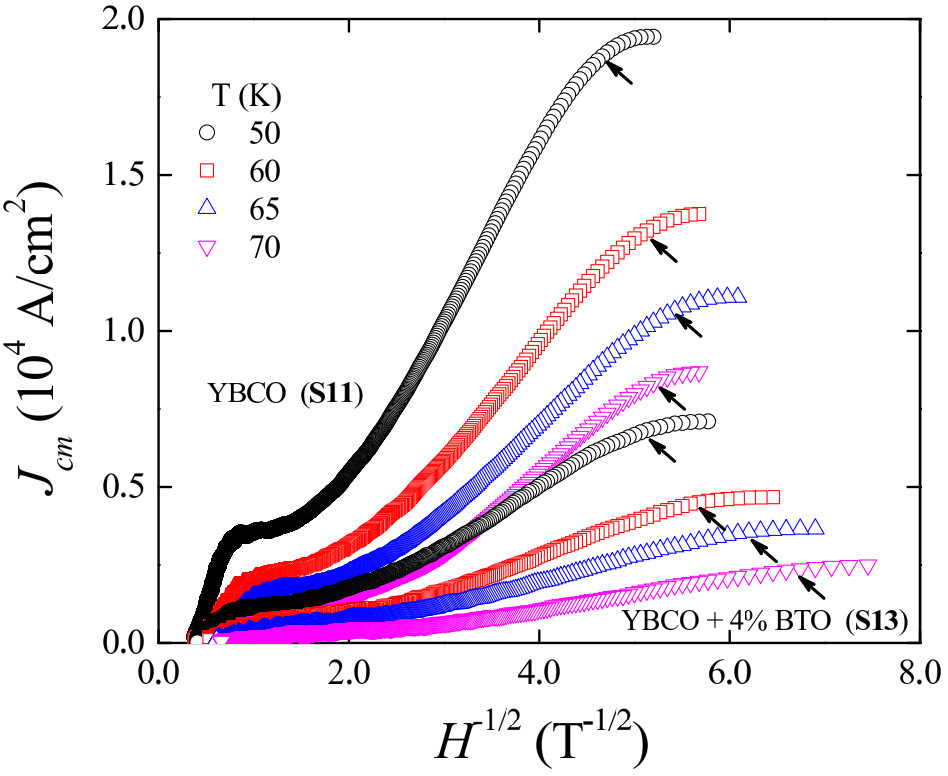

Figure 6.3.20: Magnetic critical current density, J_{cm}, as a function of $H^{-1/2}$ for **S11** and **S13** for higher temperatures. Arrows show possible crossover fields, H_{cr}

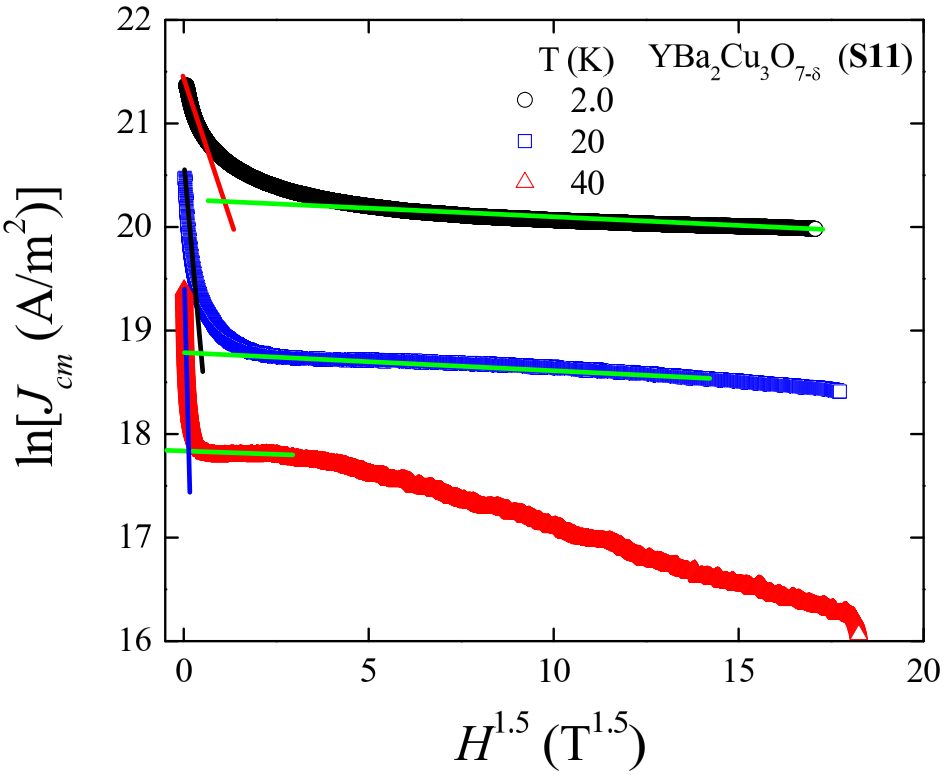

Figure 6.3.21: ln(J_{cm}) as a function of $T^{3/2}$ for **S11** at three representative T = 2.0 K, 20.0 K and 40.0 K.

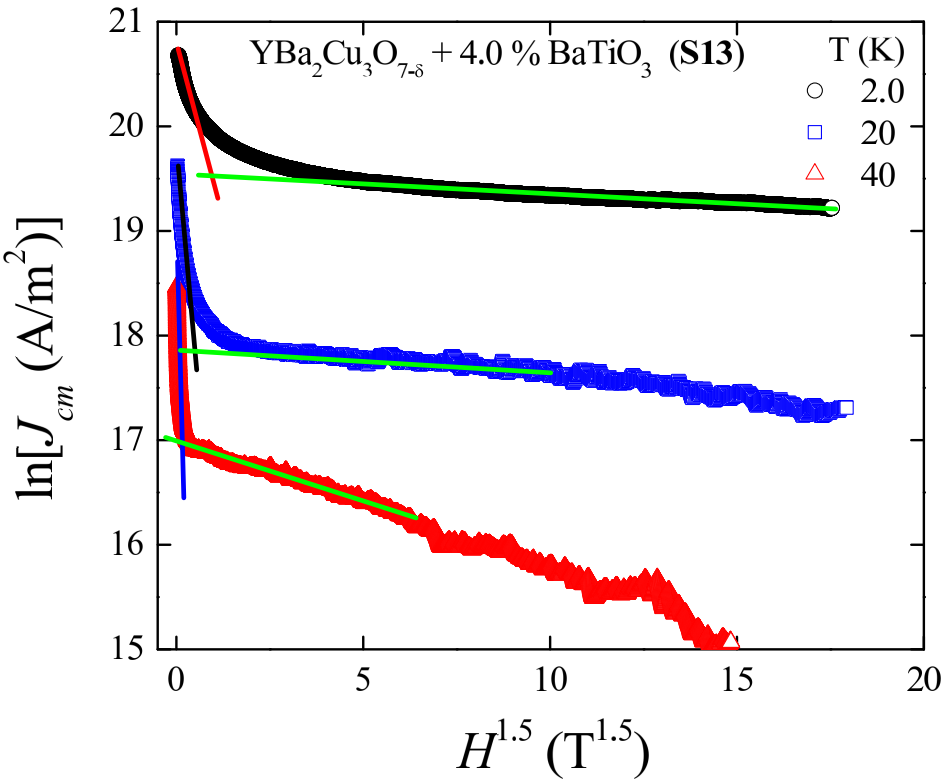

Figure 6.3.22: ln(J_{cm}) as a function of $T^{3/2}$ for **S13** at three representative T = 2.0 K, 20.0 K and 40.0 K.

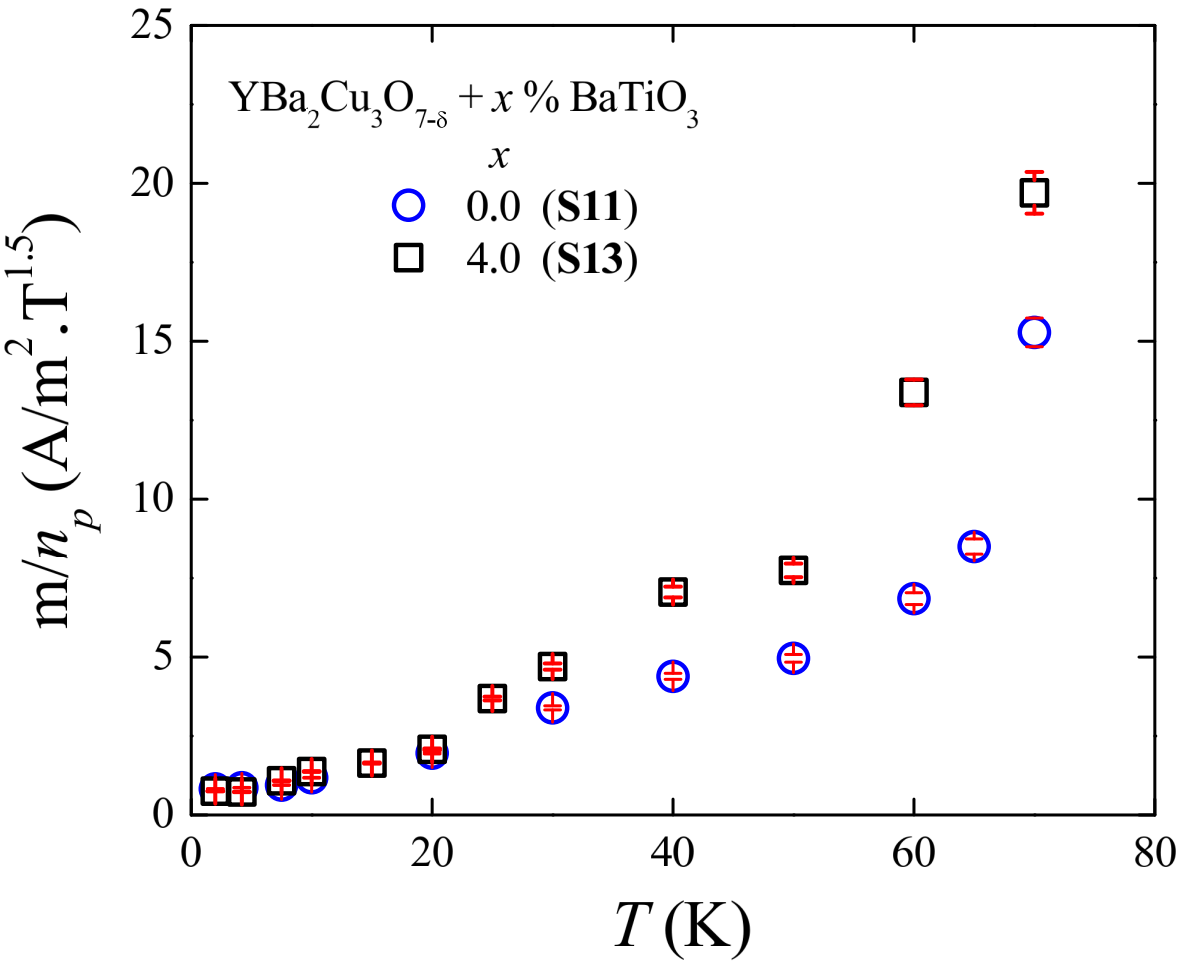

Figure 6.3.23: m/n_p as a function of T for both samples (**S11** and **S13**)

the crossover suggested in variation of $\ln(J_{cm})$ versus $H^{3/2}$. At 2.0 K, H_{cr} = 0.22 T whereas crossover from the limited collective pinning occurs at $\sim$ 1.20 T. With increase in T the crossover is found to be sensitive, as revealed in **Figure 6.3.21 - 6.3.22**. Therefore, a continuous change in the collective pinning mechanism with the selection of the range of the field is visible in both samples **[39]**.

Possibility of the crossover between collective pinning and strong pinning has been investigated by assuming a relation, $J_{cm} \propto H^{-\alpha}$ **[8, 40]**. In **Figure 6.3.24 - 6.3.25**, we have plotted $\ln(J_{cm})$ as a function of $\ln(H)$ at several T for both **S11** and **S13**, respectively. Assuming $\ln(J_{cm})$ versus $\ln(H)$ in an inter-

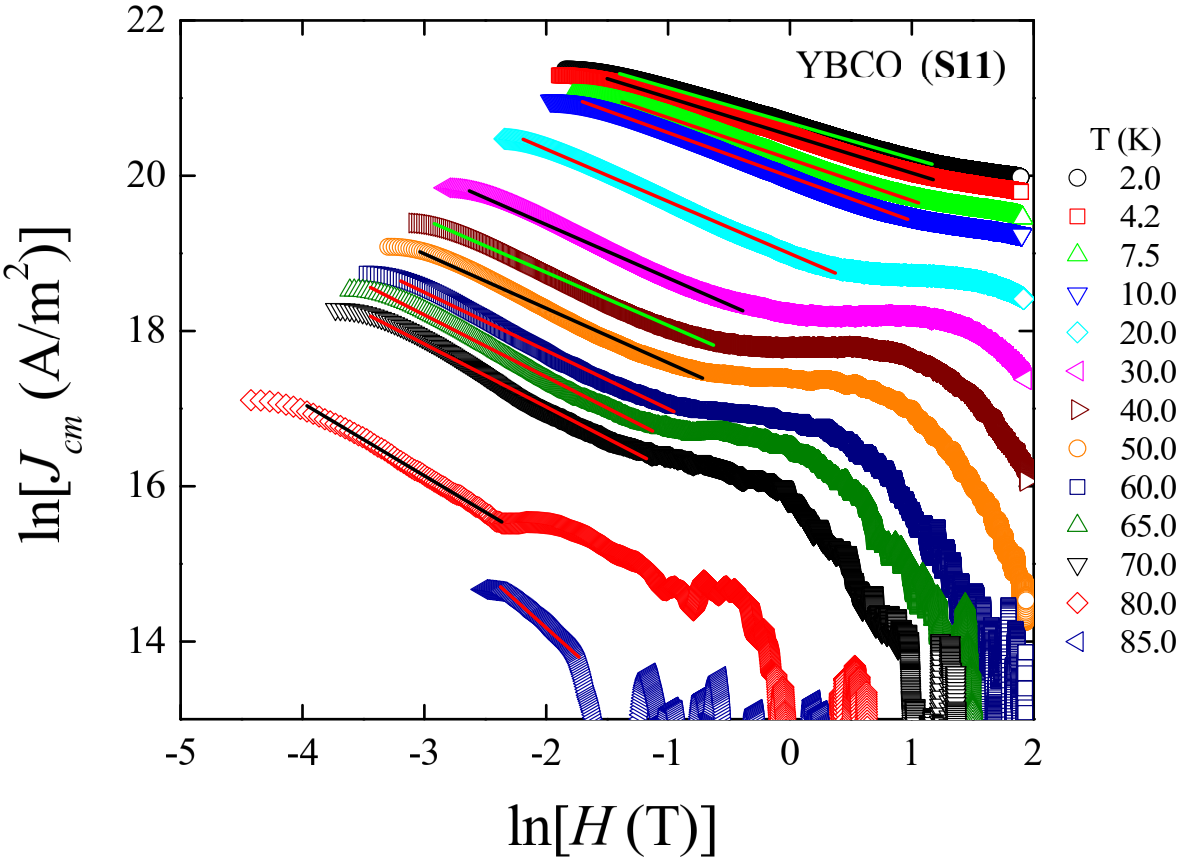

Figure 6.3.24: ln(J_{cm}) versus ln(H) with a linear fitting in the intermediate range of magnetic field at several temperatures for sample **S11**. The solid lines are fitting having the slope α.

mediate range of H as linear we have extracted an exponent α as a function of T. In **Figure 6.3.26**, we have shown α (T) for both samples. Clearly global variation of α (T) is almost similar in both samples. However, we observed that α = 5/8 in the range of 20.0 - 60.0 K [8]. A variation of exponent reveals that crossover to strong pinning is observed in both samples [41]. Even though change in the density of pinning centers (n_p) in BTO nanoparticle added YBCO has been observed, it may not be sufficiently effective in affecting the crossover from the limited collective pinning to a strong pinning regime. Moreover, a higher exponent of $\sim$ 1.2 has also been observed reflecting another regime of strong pinning [42]. We have already attempted to find out a region in which collective pinning may be a possible scenario. It

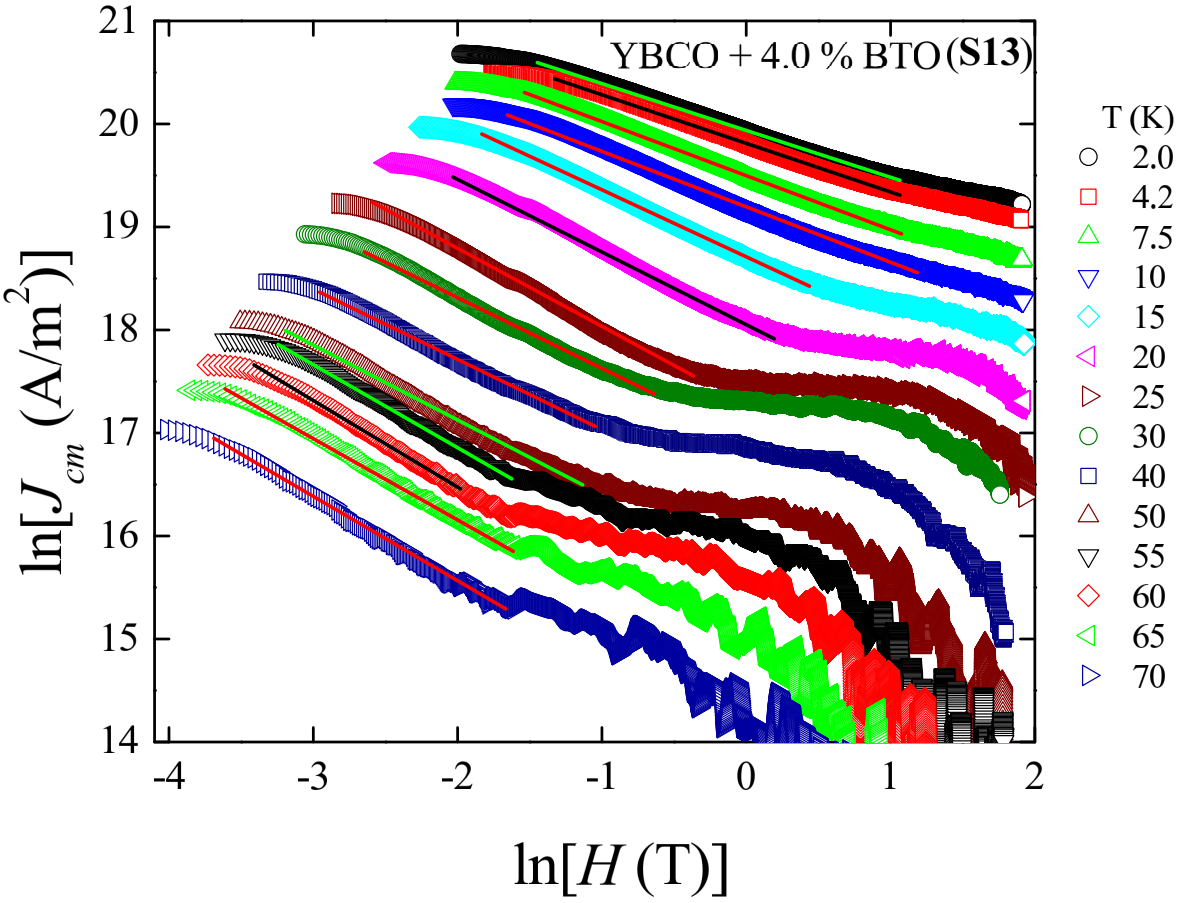

Figure 6.3.25: ln(J_{cm}) versus ln(H) with a linear fitting in the intermediate range of magnetic field at several temperatures for sample **S13**. The solid lines are fitting having the slope α.

will also be important to understand the applicability of the LO theory of collective pinning in both **S11** and **S13** samples with higher number of pinning centers [5]. Actually, we have not observed any complete peak effect (near the upper critical field, H_{c2}) except a broadened J_{cm} (H) at few intermediate temperatures. Following the dependence of J_{cm} on the magnetic field, we have observed that there is a signature of a broadened peak below the upper critical field at 20.0 K and few other intermediate temperatures for both **S11** and **S13**. It reveals that our results are comparable with the LO theory for collective pinning in the intermediate temperatures. For the lower temperature (for T = 2.0 K) the upper critical field is higher than the highest applied

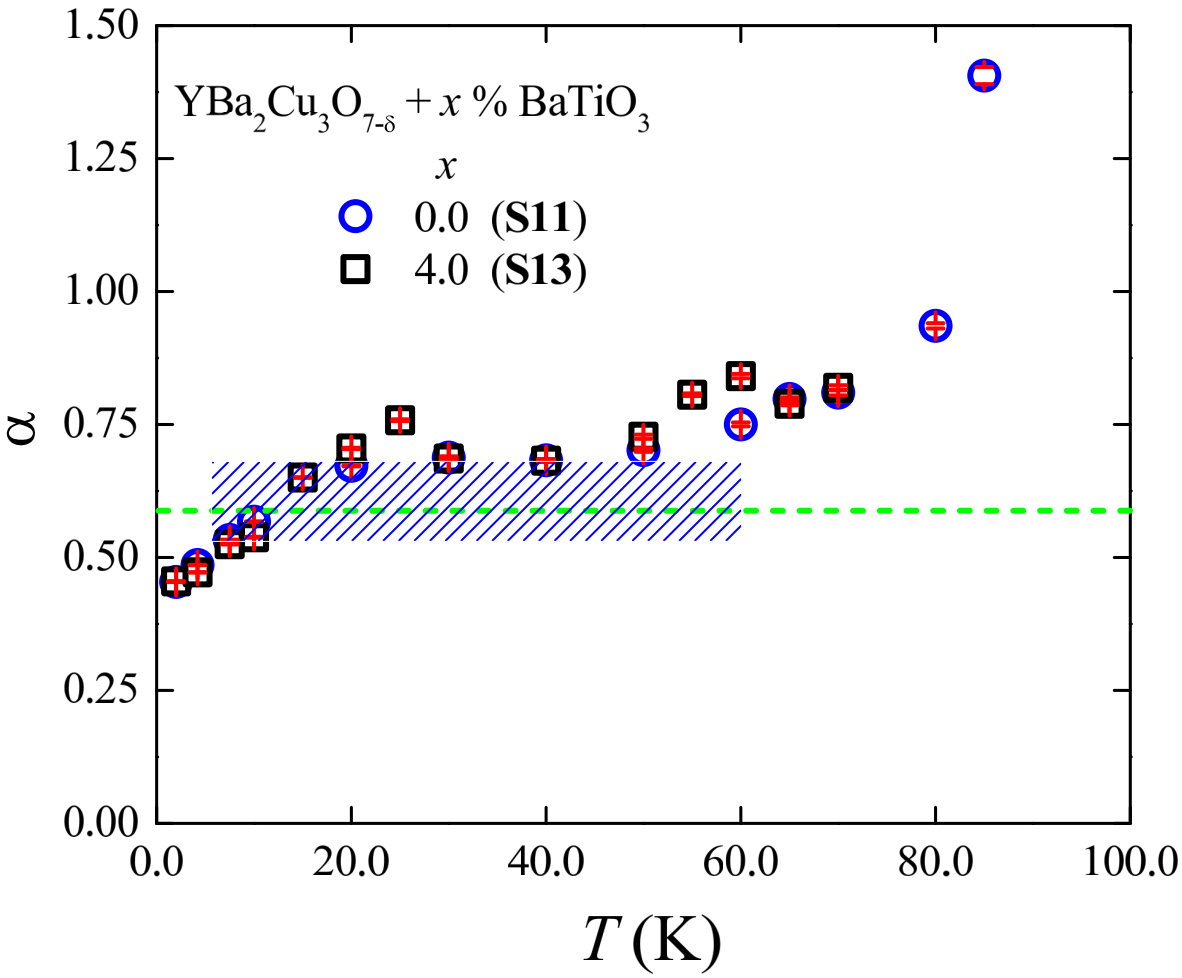

Figure 6.3.26: Variation of $\alpha(T)$ for both samples (**S11** and **S13**). The shaded region is related to the strong pinning region with slope of -5/8

magnetic field of measurements, 7.0 T. In addition, following the dependence of pinning force, F_p, on H we have also observed a dome-shaped dependence in the intermediate range of H at around 20.0 K for both **S11** and **S13**. The broadened nature peak (dome) of $F_p(H)$ reconfirms that the LO theory of the collective pinning is applicable for both the pure and composite samples with enhanced number of pinning centers.

6.4 Summary

BTO nanoparticles affect transport and magnetic critical current density in YBCO strongly. Insulating BTO reduces magnetic critical current density in order of magnitude. Following the LO collective pinning theory, field dependence of the J_{cm} reveals that density of BTO nanoparticles are more effective at lower T. A crossover from the LO collective pinning to strong pinning has been observed in both the pure YBCO and BTO included YBCO samples revealed by similar dependence of the exponent α with T. Even though nanoparticles of insulating BTO suppress both irreversibility line and critical current density, a fraction of the pinning centers becomes effective as a result of which crossover from collective pinning to strong pinning regimes becomes visible.

6.5 References

1. A. Molodyk, S. Samoilenkov, A. Markelov, P. Degtyarenko, S. Lee, V. Petrykin, M. Gaifullin, A. Mankevich, A. Vavilov, B. Sorbom, J. Cheng, S. Garberg, L. Kesler, Z. Hartwig, S. Gavrilkin, A. Tsvetkov, T. Okada, S. Awaji, D. Abraimov, A. Francis, G. Bradford, D. Larbalestier, C. Senatore, M. Bonura, A. E. Pantoja, S. C. Wimbush, N. M. Strickland, A. Vasiliev, Sci. Rep. **11** (2021) 2084.

2. A. Llordés, A. Palau, J. Gázquez, M. Coll, R. Vlad, A. Pomar, J. Arbiol, R. Guzmán, S. Ye, V. Rouco, F. Sandiumenge, S. Ricart, T. Puig, M. Varela, D. Chateigner, J. Vanacken, J. Gutiérrez, V. Moshchalkov, G. Deutscher, C. Magen, X. Obradors, Nat. Mater. **11** (2012) 329.

3. T. Haugan, P.N. Barnes, R. Wheeler, F. Meisenkothen, M. Sumption, Nature **430** (2004) 867.

4. H. Wang, A. Serquis, B. Maiorov, L. Civale, Q. X. Jia, P. N. Arendt, S. R. Foltyn, J. L. MacManus-Driscoll, X. Zhang, J. Appl. Phys. **100** (2006) 053904.

5. A. I. Larkin, Yu. N. Ovchinnikov, J. Low Temp. Phys. **34** (1979) 409.

6. M. Miura, B. Maiorov, M. Sato, M. Kanai, T. Kato, T. Kato, T. Izumi, S. Awaji, P. Mele, M. Kiuchi, T. Matsushita, NPG Asia Mater. **9** (2017) e447.

7. A. E. Koshelev, A. B. Kolton, Phys. Rev. B **84** (2011) 104528.

8. W. K. Kwok, U. Welp, A. Glatz, A. E. Koshelev, K. J. Kihlstrom, G. W. Crabtree, Rep. Prog. Phys. **79** (2016) 116501.

9. E. Mezzetti, R. Gerbaldo, G. Ghigo, L. Gozzelino, B. Minetti, C. Camerlingo, A. Monaco, G. Cuttone, A. Rovelli, Phys. Rev. B **60** (1999) 7623.

10. A. E. Koshelev, I. A. Sadovskyy, C. L. Phillips, A. Glatz, Phys. Rev. B **93** (2016) 060508(R).

11. P. Mandal, D. Rakshit, T. Sk, A. K. Ghosh, J. Supercond. Nov. Magn. **35** (2022) 1079.

12. D. Rakshit, P. Mandal, T. Sk, A. K. Ghosh, J. Supercond. Nov. Magn. **35** (2022) 1421.

13. P. Mandal, D. Rakshit, I. Mukherjee, T. Sk, A. K. Ghosh, Phys. Lett. A **436** (2022) 128072.

14. T. Sk, A. K. Ghosh, AIP Adv. **10** (2020) 065117.

15. D. Rakshit, T. Sk, P. Das, S. Haldar, A. K. Ghosh, Phys. C **588** (2021) 1353909.

16. A. Pomar, J. Gutiérrez, A. Palau, T. Puig, X. Obradors, Phys. Rev. B **73** (2006) 214522.

17. R. Guzman, J. Gazquez, B. Mundet, M. Coll, X. Obradors, T. Puig, Phys. Rev. Mater. **1** (2017) 024801.

18. S. C. Wimbush, J. H. Durrell, C. F. Tsai, H. Wang, Q. X. Jia, M. G. Blamire, J. L. MacManus-Driscoll, Supercond. Sci. Technol. **23** (2010) 045019.

19. J. Huang, H. Wang, Supercond. Sci. Technol. **30** (2017) 114004.

20. T. Sk, A. K. Ghosh, J. Low Temp. Phys. **198** (2020) 224.

21. G. Wang, M. J. Raine, D. P. Hampshire, Supercond. Sci. Technol. **30** (2017) 104001.

22. A. I. Blair, D. P. Hampshire, Phys. Rev. Res. **4** (2022) 023123.

23. I. Božović, X. He, J. Wu, A. T. Bollinger, Nature **536** (2016) 309.

24. S. Steers, T.R. Lemberger, J. Draskovic, Phys. Rev. B **94** (2016) 094525.

25. Y. Yeshurun, A. P. Malozemof, A. Shaulov, Rev. Mod. Phys. **68** (1996) 911.

26. C. P. Bean, Magnetization of high-field superconductors. Rev. Mod. Phys. **36** (1964) 31.

27. R. Hiergeist, R. Hergt, Phys. Rev. B **55** (1997) 3258.

28. X. Dong, P. An, J. Zhang, H. Zhang, Y. Li, H. Liu, X. Ge, Q. Li, J. Supercond. Nov. Magn. **27** (2014) 693.

29. Z. Li, M. Coll, B. Mundet, N. Chamorro, F. Vallès, A. Palau, J. Gazquez, S. Ricart, T. Puig, X. Obradors, Sci Rep **9** (2019) 5828.

30. M. A. P. Sebastian, J. N. Reichart, M. M. Ratclif, T. J. Bullard, J. L. Burke, C. R. Ebbing, G. Y. Panasyuk, C. Tsai, W. Zhang, J. Huang, H. Wang, J. Wu, T. J. Haugan, IEEE Trans. Appl. Supercond. **27** (2017) 1.

31. T. Nishizaki, T. Naito, N. Kobayashi, Phys. Rev. B **58** (1998) 11169.

32. F. Vallès, A. Palau, D. Abraimov, J. Jaroszynski, A. M. Constantinescu, B. Mundet, X. Obradors, D. Larbalestier, T. Puig, Commun. Mater. **3** (2022) 45.

33. Th. Schuster, M. R. Koblischka, H. Kuhn, H. Kronmüller, M. Leghissa, W. Gerhäuser, G. Saemann-Ischenko, H. W. Neumüller, S. Klaumünzer, Phys. Rev. B **46** (1992) 8496.

34. J. Gutiérrez, A. Llordés, J. Gázquez, M. Gibert, N. Romà, S. Ricart, A. Pomar, F. Sandiumenge, N. Mestres, T. Puig, X. Obradors, Nat. Mater **6** (2007) 367.

35. J. P. Rodriguez, M. P. Maley, Phys. Rev. B **73** (2006) 094502.

36. A. Ruyter, D. Plessis, Ch. Simon, A. Wahl, L. Ammor, Phys. Rev. B **77** (2008) 212507.

37. R. Hiergeist, R. Hergt, Phys. Rev. B **55** (1997) 3258.

38. G. Blatter, V. B. Geshkenbein, J. A. G. Koopmann, Phys. Rev. Lett. **92** (2004) 067009.

39. N. Haberkorn, M. Miura, J. Baca, B. Maiorov, I. Usov, P. Dowden, S. R. Foltyn, T. G. Holesinger, J. O. Willis, K. R. Marken, T. Izumi, Y. Shiohara, L. Civale, Phys. Rev. B **85** (2012) 174504.

40. Yu. N. Ovchinnikov, B. I. Ivlev, Phys. Rev. B **43** (1991) 8024.

41. C. J. van der Beek, M. Konczykowski, M. V. Indenbom, S. Barbanera, Phys. Rev. B **66** (2002) 024523.

42. F. C. Klaassen, G. Doornbos, J. M. Huijbregtse, R. C. F. van der Geest, B. Dam, R. Griessen, Phys. Rev. B **64** (2001) 184523.

Chapter 7

Transport critical current density in composite system of $NdBa_2Cu_3O_{7-\delta}$ and Sn nanoparticles

7.1 Introduction

Enhancing the pinning of vortices in high temperature superconductors (HTS) is possible by inclusion of artificial pinning centers (APC) [1, 2]. Inclusion of nanoparticles in the intergranular region of polycrystalline HTS has shown substantial change in the flux pinning mechanisms. Generally vortex pinning becomes the most effective while the size of these nanoparticles matches with the size of the coherence length. No universal size and concentrations of the added nanoparticles is known which may help in optimizing the critical current density (J_c) in a particular HTS. Even though the pinning strength is sufficiently high in HTS, it varies widely depending on the effective pinning strengths. As a result of the inclusion of nanoparticles both increase and decrease in J_c have been observed in several forms of HTS [3 -

7]. Moreover, both the size and concentration of the pinning centers affects the nature of the vortex pinning [8]. $NdBa_2Cu_3O_{7-\delta}$ (NBCO) is such a HTS in which the critical current density is high due to the intrinsic point pinning centers [9]. It is not clear how the addition of the nanoparticles in such a HTS will affect the pinning properties and hence transport J_c.

We report transport properties of (i) the pure $NdBa_2Cu_3O_{7-\delta}$ (NBCO) and (ii) several composite systems consisting of Sn nanoparticles and NBCO. Four different concentrations (x) of Sn nanoparticles have been used. We have studied nonlinear nature of IV by an exponent $\eta(T)$. IV characteristics have also been used to extract transport critical current density (J_c). An electric field (E) based criterion has been used to extract J_c. An exponential form of the $J_c(T)$ applicable for the weak pinning limit has been compared with our experimental $J_c(T)$. The impact of the nanoparticles on bulk NBCO has been studied. Usefulness of the intergranular Sn nanoparticles to change the J_c in NBCO has also been discussed.

7.2 Experimental

We have synthesized bulk $NdBa_2Cu_3O_{7-\delta}$ (NBCO) superconductors by using the solid state reaction method [10, 11]. The sintering temperature remains in the range between 925 to 950 °C. The Sn nanopowder has been mixed to the pure NBCO (**S16**) before the last sintering to obtain NBCO-Sn composite superconductors. We have used x = 0.5% (**S17**),1.0% (**S18**), 1.5% (**S19**) and 2.0% (**S20**) of Sn as weight % of pure NBCO. Annealing of the pure and mixed samples is carried out at 450 °C using uniform oxy-

gen flow rate for a longer time of 50 hours. Characterization of samples has been performed by using X-ray diffraction (XRD) and scanning electron micrographs (SEM). XRD patterns have been obtained by using a Bruker D8 X-ray Diffractometer with CuK_α (λ = 1.5418 Å) source. We have cut bar-shaped samples for all the transport measurements. Typical dimensions of the samples are 5.9 mm×2.6 mm×0.6 mm. Resistivity (ρ) as a function of T has been measured by using the standard four-probe method with the help of a cryogenerator (Janis, USA). At several constant T, IV measurements have been carried out below T_c. The range of the current used for IV measurements is 100.0 nA through 5.0 mA **[12 - 14]**.

7.3 Results and Discussions

Five representative micrographs of the pure and Sn-mixed NBCO have been shown in **Figure 7.3.1**. Using the ImageJ software program we have extracted the average size of grains (D) and variance (σ_D). A weak decreasing trend of the average size of grains has been observed with the increasing x. As x is increased the intergranular regions become affected as revealed in micrographs. XRD patterns have been shown in **Figure 7.3.2**. In the figure, *hkl* corresponding to the NBCO (**S16**) are identified. In **S17** - **S20** composite samples we have not observed any peak corresponding to the tin oxides. For the **S20** sample, an extra peak corresponding to the $\beta - Sn$ are marked as $+$ sign **[15]**. However, there may be some oxide of Sn even if the density of the Sn nanoparticles used are very low and the excess oxygen content of NBCO may have higher exposure to diffused oxygen (during the sintering process)

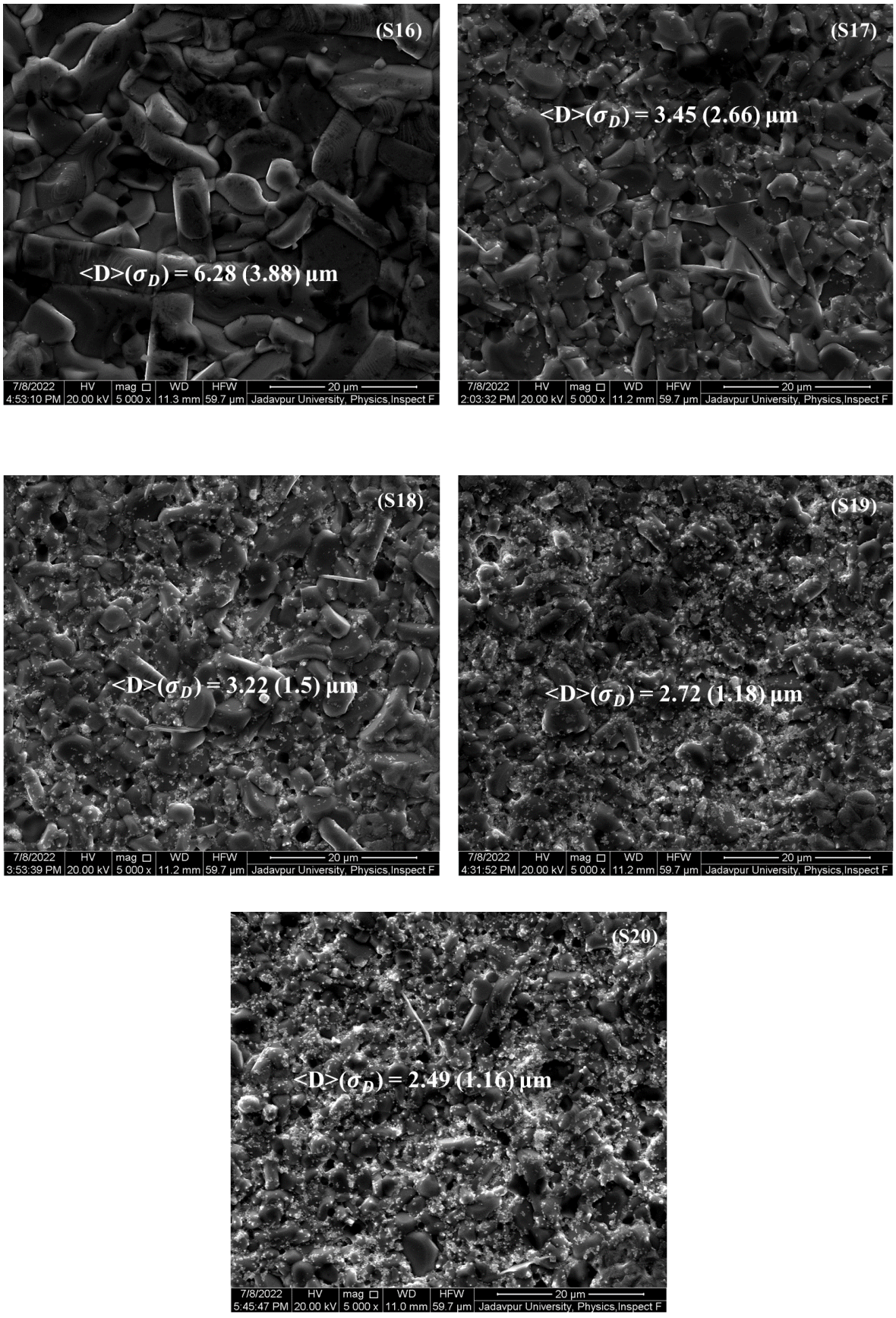

Figure 7.3.1: Representative scanning electron micrographs (SEMs) of the samples with x = 0.0, 0.5, 1.0, 1.5 and 2.0.

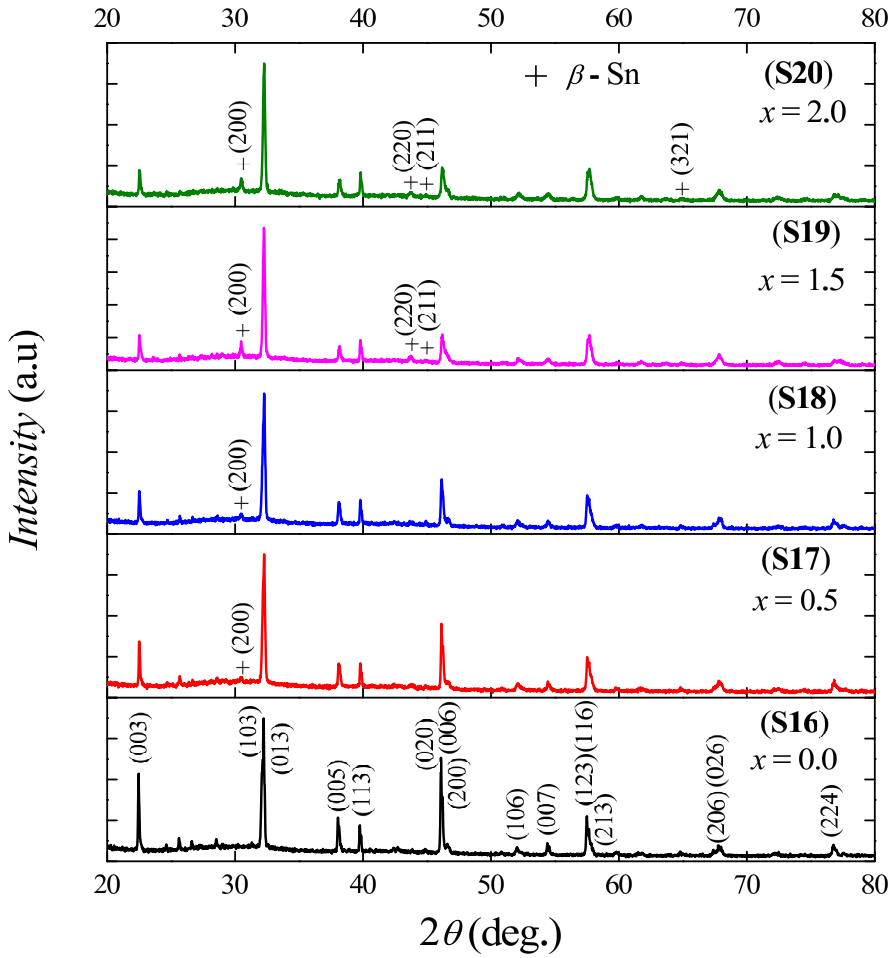

Figure 7.3.2: X-ray diffraction (XRD) pattern of the samples with x = 0.0, 0.5, 1.0, 1.5 and 2.0. Peak corresponding to the $\beta - Sn$ are marked as + sign.

in the intergranular regions. Following the XRD patterns, it is reasonable to assert that the intergranular regions of composite (**S17** - **S20**) are having mostly Sn nanoparticles.

In **Figure 7.3.3**, we have shown the resistivity (ρ) as a function of temperature (T). In the normal state, the ρ (T) of the pure NBCO exhibits a downward curvature followed by an upturn with the decreasing T. It indicates an electron-electron scattering and the presence of the variable range hopping (VRH) conduction mechanism prior to the superconducting state **[16]**. The sample **S19** (x = 1.5) shows the highest ρ (300.0 K) whereas the lowest ρ (300.0 K) is observed in **S17** (x = 0.5). With the increase in x, the re-

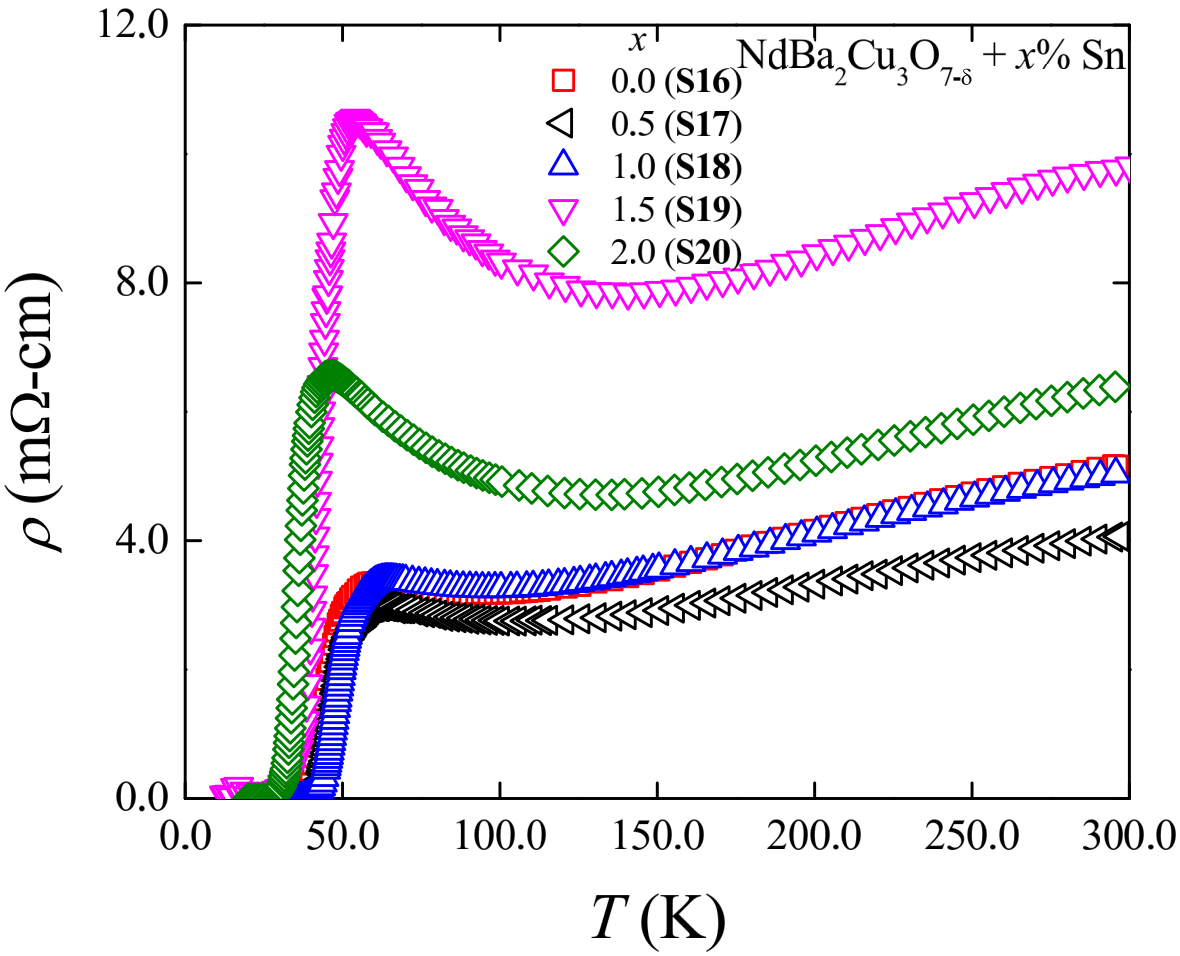

Figure 7.3.3: Resistivity (ρ) as a function of the temperature T of pure (x = 0.0) NBCO superconductor and Sn-mixed NBCO with x = 0.5, 1.0, 1.5 and 2.0.

sistivity mostly increases in the normal state for the highest concentration of Sn. In addition, the upturn becomes more prominent in the sample with the highest concentration. However, in all composite samples superconducting transitions are very prominent.

In **Figure 7.3.4**, we have shown $d\rho/dT$ as a function of T for all the samples. The onset of superconducting transition temperature, T_c has been shown in **Figure 7.3.4**. T_c of the pure (x = 0.0) NBCO (**S16**) is found to be 59.8 K. For **S17** (x = 0.5) and **S18** (x = 1.0) samples T_c's are 61.0 K and 64.1 K respectively which are slightly higher compared to the pure one.

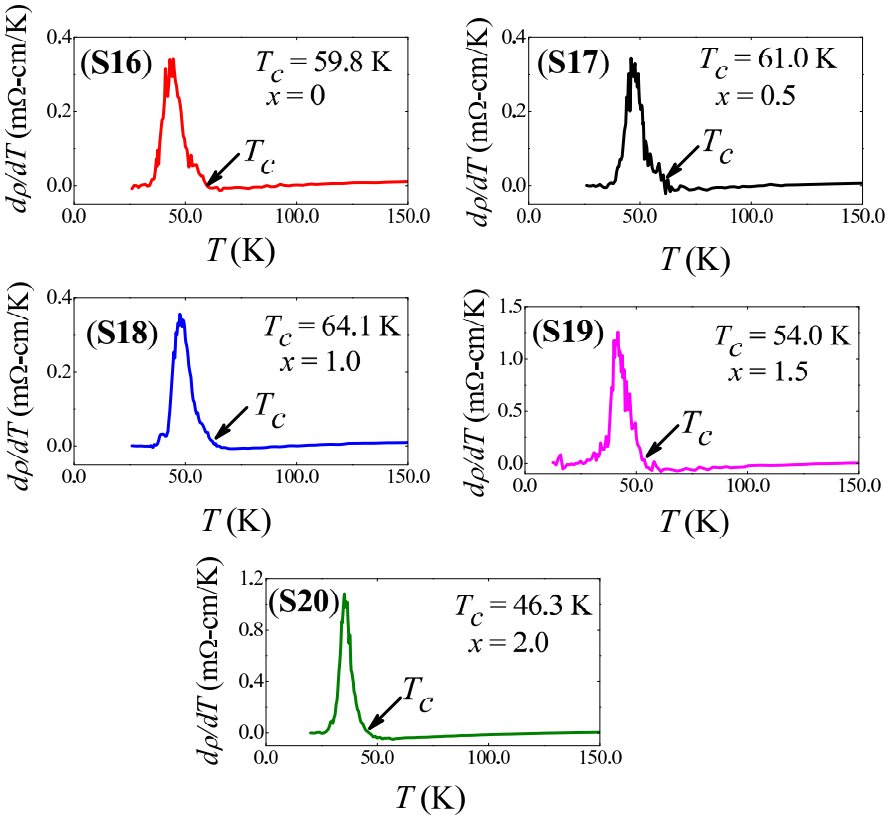

Figure 7.3.4: Variations of $d\rho/dT$ as a function of T of NBCO with x = 0.0, 0.5, 1.0, 1.5 and 2.0. T_c have been shown by an arrow.

For **S19** (x = 1.5) and **S20** (x = 2.0) samples, T_cs are found to be 54.0 K and 46.3 K respectively. T_c (ρ = 0) are found to be 33.8 K, 35.6 K, 35.6 K, 26.9 K and 26.3 K corresponding to x = 0.0, 0.5, 1.0, 1.5 and 2.0 respectively. Clearly the phase transition region gets strongly affected by Sn nanoparticles. Even though the origin of the superconducting pairs are within the grains of NBCO, inter-granular Sn particles strongly affect the tunnelling of Cooper pairs between neighbouring grains.

Current-voltage (IV) characteristics at several T below T_c have been shown in the **Figure 7.3.5 - 7.3.9** for all five samples. Electric field (E) and current density (J) corresponding to voltage drop, V and applied current I respectively are also shown for each sample. In **Figure 7.3.5**, we have shown IV in the range of T = 54.0 K through 36.0 K for NBCO (x = 0.0). In the

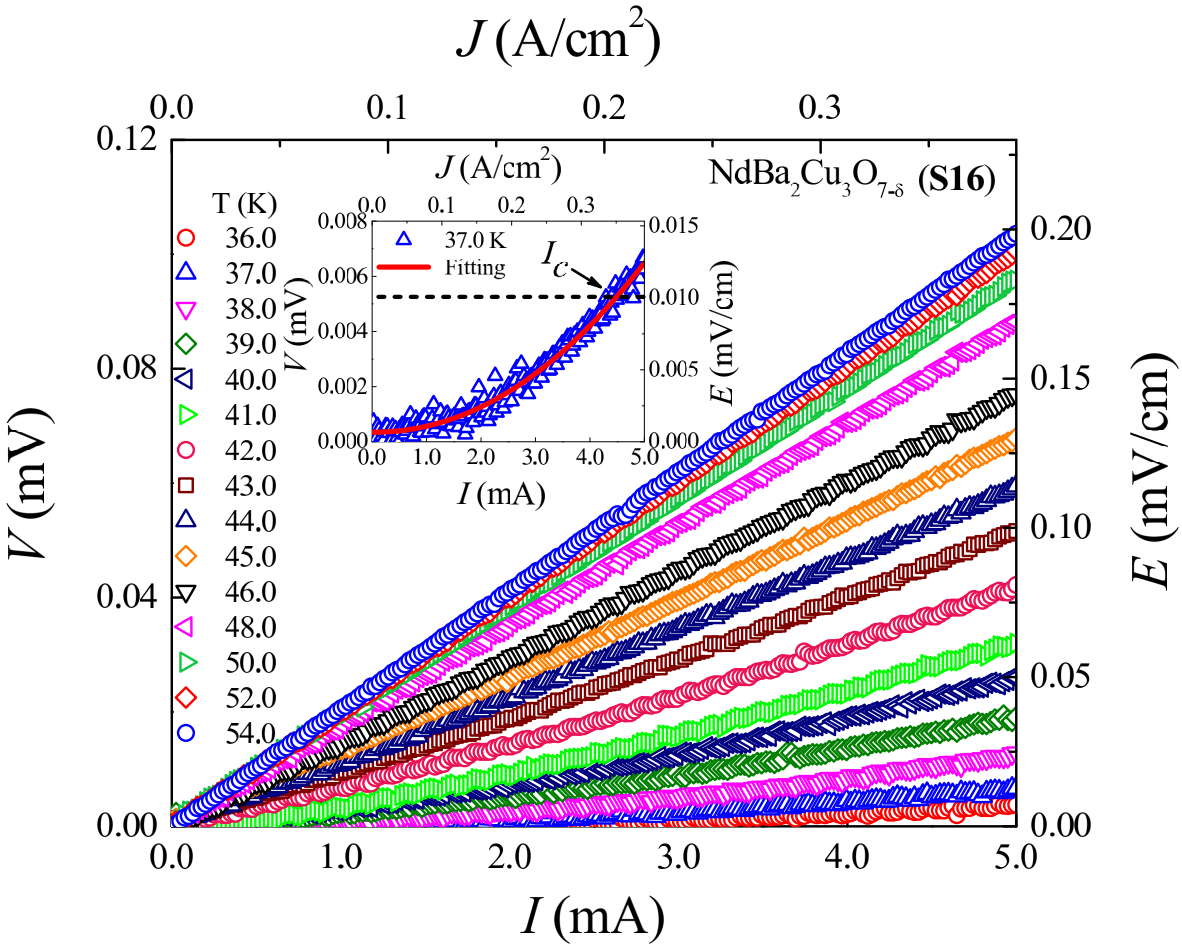

Figure 7.3.5: Current-voltage characteristics (*IV*) of the sample with x = 0.0 at several temperatures below critical temperature. In the inset we have shown a representative lowest temperature *IV* together with the extraction criterion

inset of **Figure 7.3.5** a representative *IV* measured at T = 37.0 K is shown to understand the nature of nonlinearity. As the T increases nonlinear curvature is reduced and at 46.0 K it becomes linear. In **Figure 7.3.6**, *IV* characteristics in the range of 61.0 K to 41.0 K corresponding to the sample with x = 0.5 are shown. In the inset of **Figure 7.3.6**, a nonlinear *IV* curve at T = 43.0 K is shown. In **Figure 7.3.7**, we have shown *IV* curves of the sample with x = 1.0 in the range of 63.0 K to 38.0 K. Inset shows *IV* at 38.0 K. *IV* plot for the sample with x = 1.5 have been shown in the temperature range of 52.0 K - 32.0 K in **Figure 7.3.8** and inset shows the *IV* curve at 32.0 K.

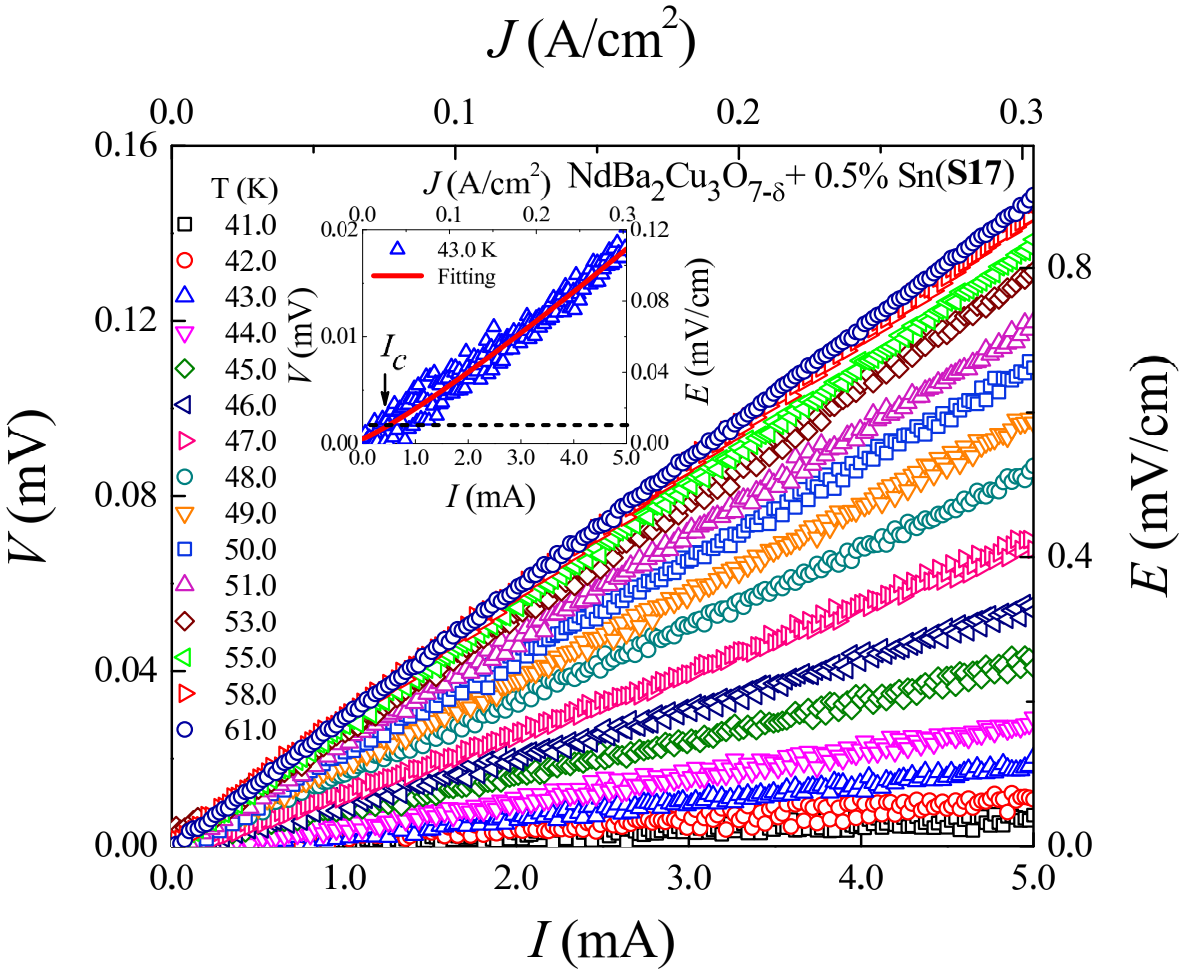

Figure 7.3.6: Current-voltage characteristics (IV) of the sample with x = 0.5 at several temperatures below critical temperature. In the inset we have shown a representative lowest temperature IV together with the extraction criterion

For the sample having the highest concentration of Sn, x = 2.0, we have also shown IV characteristics in **Figure 7.3.9** in the range 45.0 K through 29.0 K. Inset shows the IV for T = 29.0 K. The nonlinear nature observed in NBCO is highly affected by the inclusion of the Sn nanoparticles. Different ranges of T have been found in which the nonlinear character of IV exists. No nonlinear nature of IV has been observed as a result of the granularity because we have no nonlinear IV above T_c. Nonlinear features are observed earlier in several single crystals of YBCO [17], thin films [18] and bulk polycrystalline HTS [19, 20]. The nonlinear nature arises because of the presence of

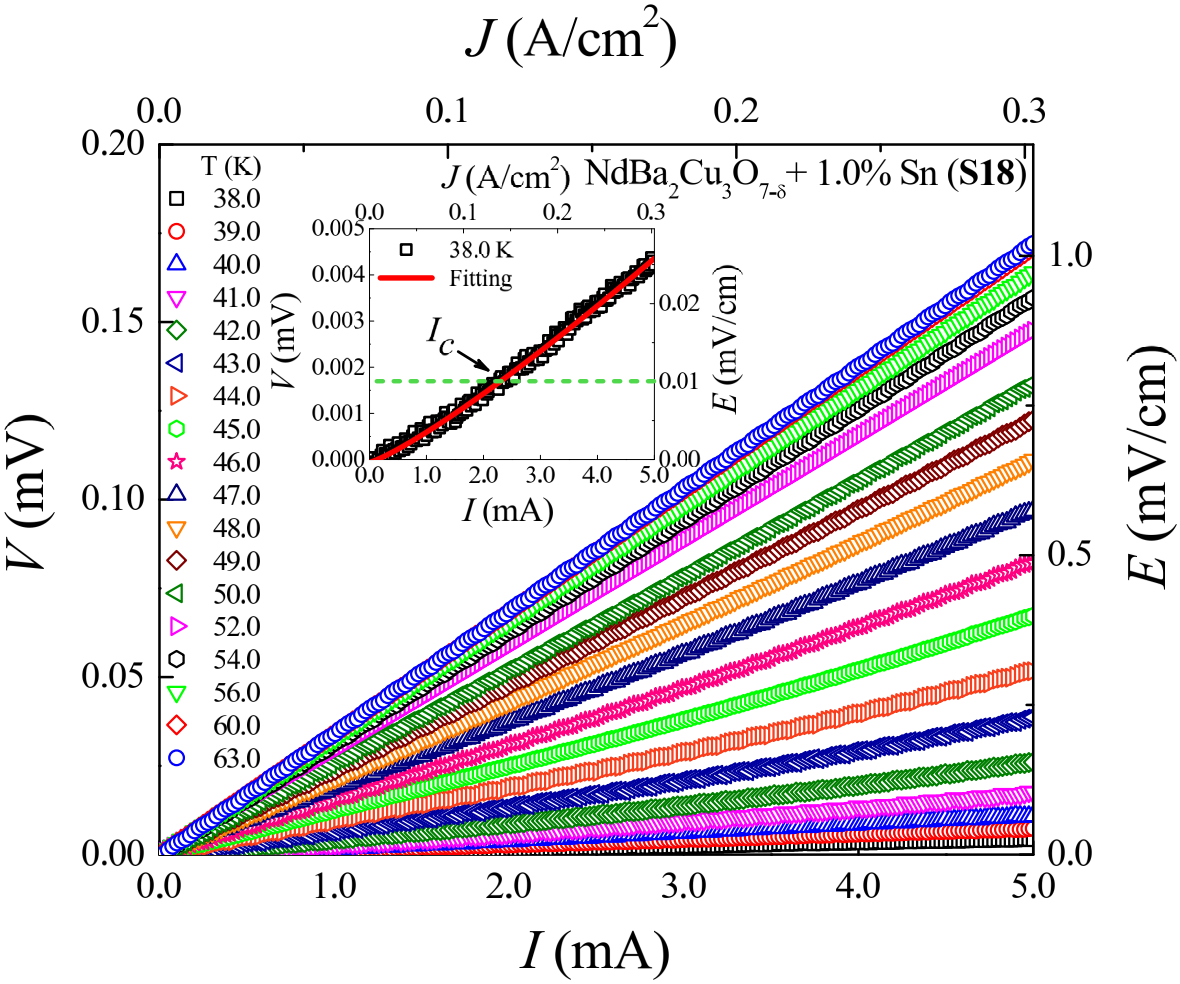

Figure 7.3.7: Current-voltage characteristics (IV) of the sample with x = 1.0 at several temperatures below critical temperature. In the inset we have shown a representative lowest temperature IV together with the extraction criterion

the bound pairs of vortex-antivortex as described within the framework of the BKT phase transition **[21 - 23]**.

The nonlinear behaviour of IV characteristics for the pure and composite samples has been studied using an equation in the form $V = aI^{\eta}$ **[24, 25]**. Here η is an exponent related to nonlinear behaviour of IV in the framework of the BKT phase transition. At several T around the phase transition, we have extracted η **[26]**. In **Figure 7.3.10**, we have shown the variation of η as a function of T for all the samples. η increases with the decrease in T

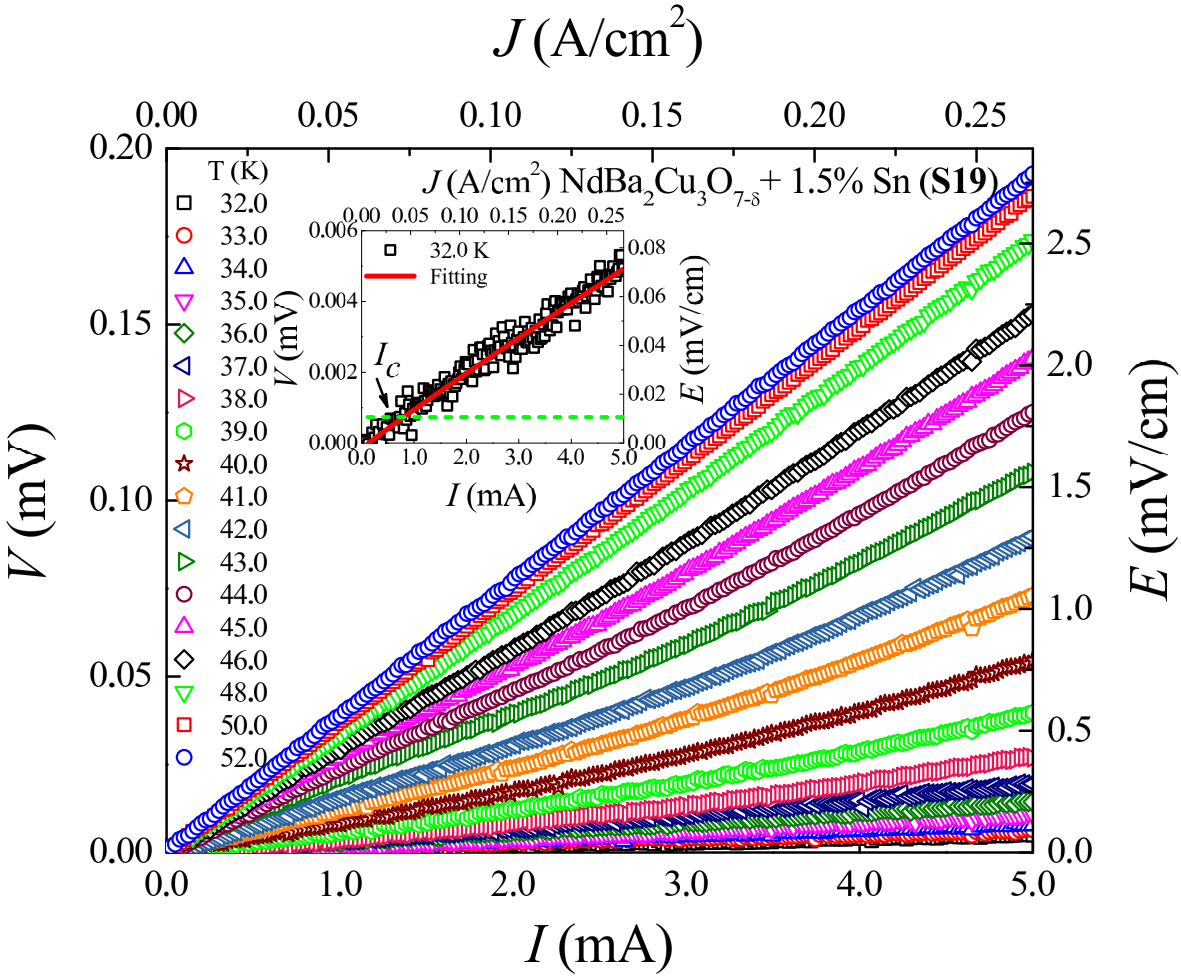

Figure 7.3.8: Current-voltage characteristics (IV) of the sample with x = 1.5 at several temperatures below critical temperature. In the inset we have shown a representative lowest temperature IV together with the extraction criterion

below 45.0 K in NBCO. The highest value of $\eta = 2.5$ has been observed in a pure sample. The BKT phase transition corresponds to a change in the η = 1 to 3 [18]. Therefore, we have observed an incomplete and broadened BKT phase transition in NBCO [27]. In the composite sample **S17**, the η (T) shows almost similar trend as is observed in **S16**. However, the maximum η (T = 43.7 K) is found to be 1.3. For x = 1.0 (**S18**), we have observed that η (T) exhibits a peak at 42.0 K followed by a minor dip at T = 40.0 K. This feature clearly arises due to the impact of Sn nanoparticles on the

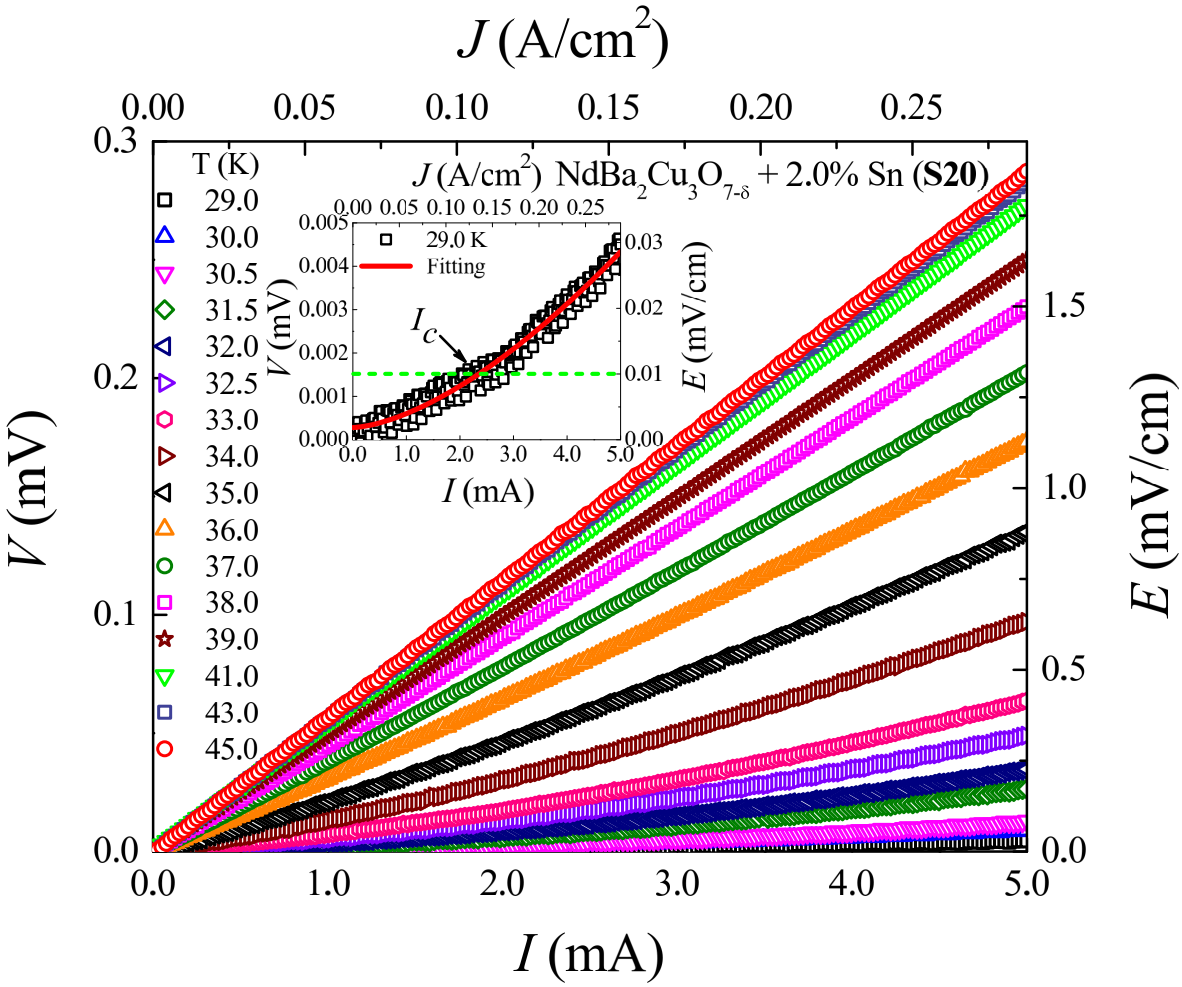

Figure 7.3.9: Current-voltage characteristics (IV) of the samples with x = 2.0 at several temperatures below critical temperature. In the inset we have shown a representative lowest temperature IV together with the extraction criterion

vortex-antivortex bound states. In another composite sample **S19** a peak in η (T) is also observed at 39.0 K. For the highest x = 2.0 (**S20**), an oscillating nature in η (T) is observed. Absence of monotonic increase in η (T) with the decrease in T in composite samples is first time observed in presence of Sn nanoparticles in NBCO. It indicates that intergranular nanoparticles affect the nonlinear exponent randomly as a result of the random distribution of the particles in the intergranular regions of NBCO.

We have extracted the transport critical current density, J_c, as a function

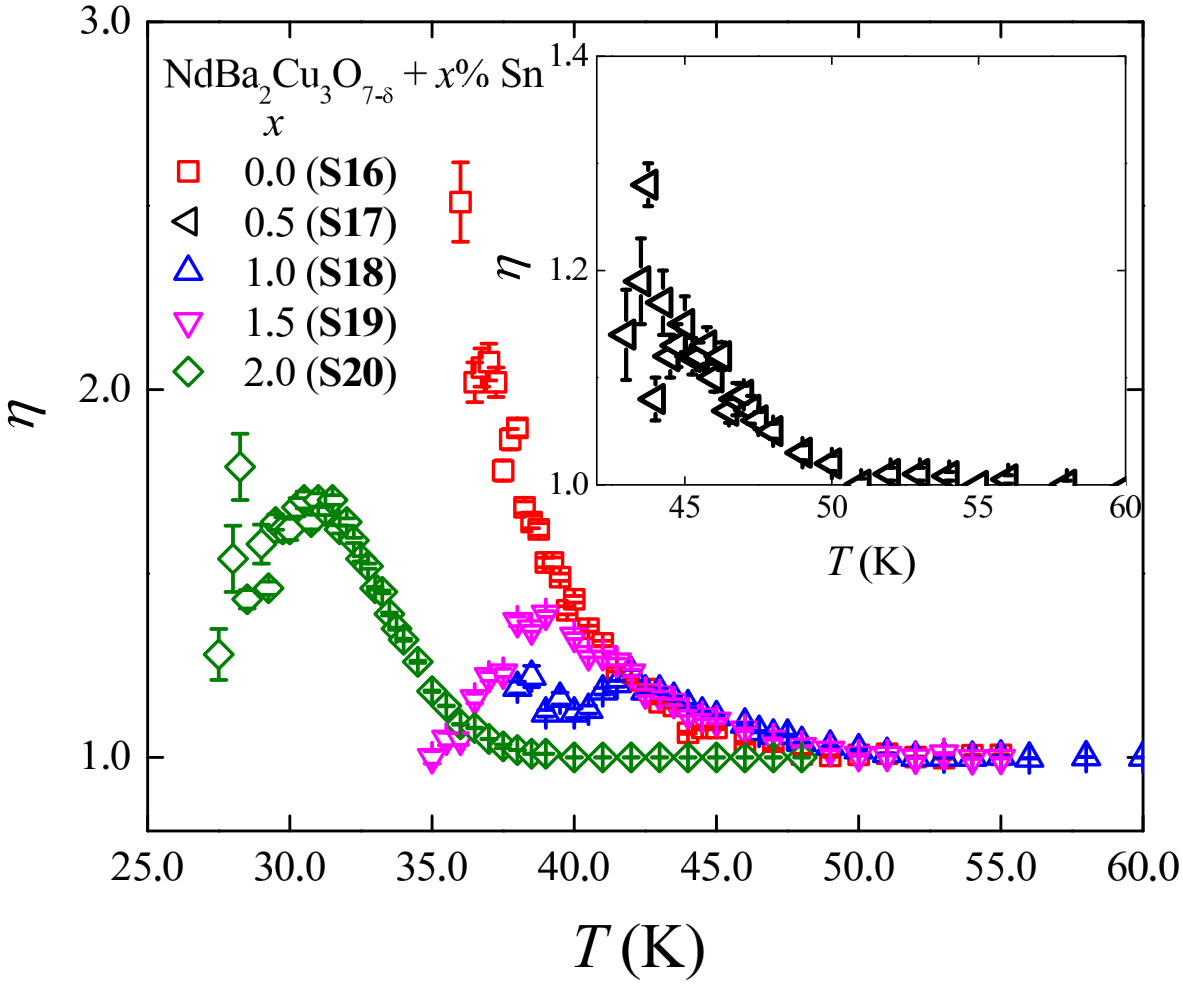

Figure 7.3.10: Variations of exponent η with the temperature of the samples with $x = 0.0$, 0.5 (in the inset), 1.0, 1.5 and 2.0.

of T by using the criterion $E = 0.01$ mV/cm below T_c. Variations of $J_c(T)$ have been shown in **Figure 7.3.11**. The maximum J_c is found to be 0.23 A/cm^2 at 36.3 K in NBCO. Inclusion of Sn nanoparticles does not change the maximum $J_c(T)$ in comparison to the pure NBCO. However, the composite samples exhibit maximum J_c at lower T. For example J_c is maximum at 28.0 K for the composite sample with the highest $x = 2.0$. However, no systematic increase in J_c as a result of the inclusion of nanoparticles of Sn has been observed. Addition of Sn nanoparticles in the intergranular site may act as artificial pinning centers **[28, 29]**. Depending on the inclusion of additional pinning centers changes the pinning nature **[30]**. Because we observe a

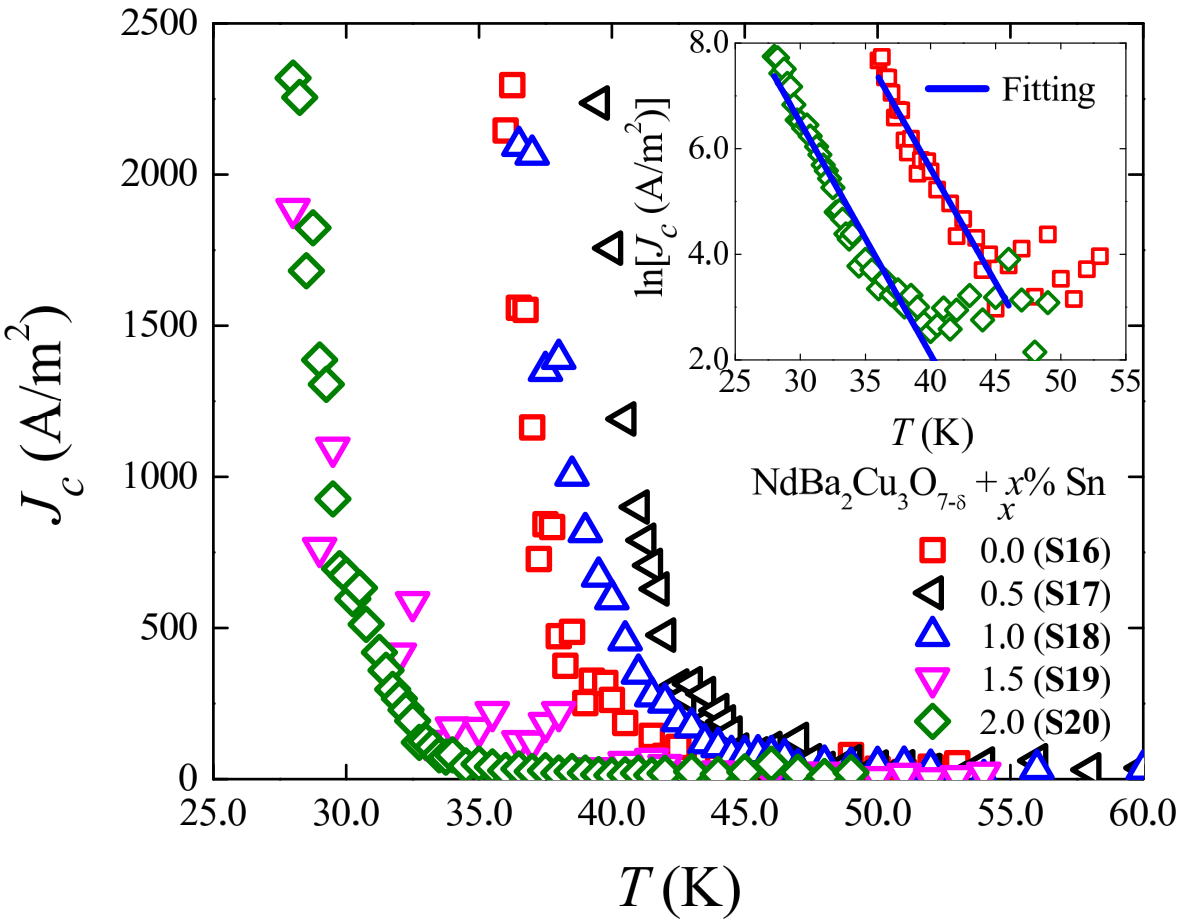

Figure 7.3.11: Transport critical current density (J_c) as a function of T for all samples with x = 0, 0.5, 1.0, 1.5 and 2.0. In the inset, we have shown ln(J_c) as a function of T together with weak pinning fitting scenario by solid line.

relatively lower $J_c(T)$ in the pure NBCO, we have made an attempt to check whether the weak pinning nature changes as a result of the addition of Sn. We have analyzed experimental $J_c(T)$ data using an exponential equation of the form of $J_c^{wk}(T) = J_c^{wk}(0)exp(-\frac{T}{T_0})$. We have shown two typical fittings in the inset of **Figure 7.3.11**. The co-efficient $J_c^{wk}(0)$ and a characteristic temperature, T_0 has been extracted and shown in **Figure 7.3.12** [31]. $J_c^{wk}(0)$ shows no increasing trend beyond x = 0.5 indicating that addition of Sn may not be strong enough to overcome the intrinsic pinning strength of NBCO. However, T_0 exhibits an increasing trend up to x = 1.5. Therefore, even though the pinning energy scale (T_0) increases with x, the effectiveness of the pinning

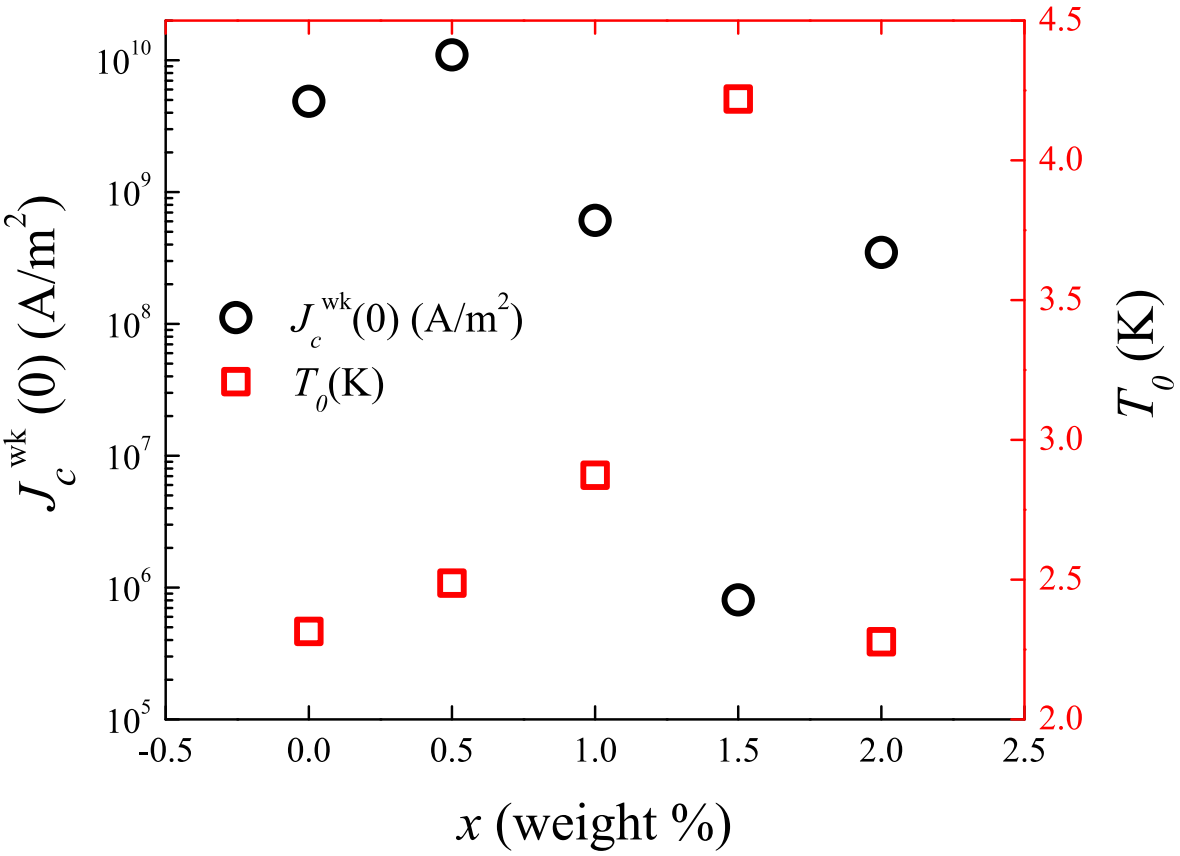

Figure 7.3.12: Variation of $J_c^{wk}(0)$ and T_0 for all samples with x = 0.0, 0.5, 1.0, 1.5 and 2.0.

centers are not sufficient enough beyond $x = 0.5$. It is attributed to the limited scope of the enhancement of transport J_c by Sn nanoparticles. We also suggest that reduction of size of the particles will be necessary to understand the effectiveness of nanoparticles in enhancing J_c in NBCO.

7.4 Summary and future directions

Polycrystalline NBCO superconductors exhibit nonlinear *IV* characteristics below T_c. Even though inclusion of Sn nanoparticles changes normal state resistivity strongly changes in T_c remains very weak. The nature of variation of the nonlinear exponent with T exhibits new features in composite samples. Transport critical current density extracted from *IV* curves reveals that

the pinning mechanism is very sensitive to the inclusion of nanoparticles of Sn. However, the maximum J_c remains almost unchanged in the composite system except for $x = 0.5$. Inclusions of nanoparticles change the weak pinning nature of the bulk NBCO. Moreover a characteristic temperature (T_0) increases with x upto $x = 1.5$.

Since the discovery of HTS an open question remains whether these superconducting materials can be used to achieve a higher critical current density. Because of the very high intrinsic pinning in HTS, the critical current density in pure HTS samples including YBCO is known to be very high [$\sim$90 MA/cm^2 at 5.0 K]. Cuprate HTS systems exhibit the highest J_c in YBCO thin film. It is also known that in the bulk HTS, J_c is highly reduced even in presence of vortex pinning by grain boundaries. Moreover, most of the technological applications demand an extended version of the superconducting samples. For technological applications of HTS researchers are mostly looking for reaching to an optimum condition by adjusting number density and distribution of several types of pinning centers in HTS. We have adopted our current results on critical current density in this context throughout the present investigation. Systems we have studied are having different pinning conditions which can be classified in two groups. The first group of samples [**S1** - **S4**, **S6**, **S11** and **S16**] are related to controlling pinning from the lattice sites whereas the second category of systems [**S5**, **S7** - **S10**, **S12** - **S15** and **S17** - **S20**] are directed towards controlling pinning from the intergranular networks. Overall in both cases we observed pinning centers may be effective strongly. However, it is required to optimize the strength of pinning in both cases. A reduction in J_c in several cases even after attempting to optimize

concentrations and distributions of added pinning centers will be an important direction to understand how to improve effective pinning of line vortices. Nevertheless, it will be important to mention that even though in bulk pure and hybrid HTS systems, the total J_c is much lower than that of the thin film and single crystal of YBCO, the absolute value is really high and some of these hybrid materials will be important for technological applications such as generating high magnetic fields because of higher order of magnitude of the characteristic magnetic fields including the upper critical field. However, it will be necessary to tune the exact amount of inclusions in YBCO or other cuprates for achieving the highest critical current density. More research in this direction will be necessary in coming future years. Many other inclusions having different pinning strengths are to be considered for HTS to pinpoint the best possible combinations for technological applications.

7.5 References

1. K. Matsumoto, P. Mele, Supercond. Sci. Technol. **23** (2010) 014001.

2. T. J. Haugan, T. Puig, K. Matsumoto, J. Wu, Supercond. Sci. Technol. **33** (2020) 040301.

3. S. H. Wee, A. Goyal, J. Li, Y. L. Zuev, S. Cook, J. Appl. Phys. **102** (2007) 063906.

4. S. H. Wee, A. Goyal, J. Li, Y. L. Zuev, S. Cook, L. Heatherly, Supercond. Sci. Technol. **20** (2007) 789.

5. A. P. Menushenkov, A. A. Ivanov, O. V. Chernysheva, I. A. Rudnev, M. A. Osipov, A. R. Kaul, V. N. Chepikov, O. Mathon, V. Monteseguro, F. d'Acapito, A. Puri, Supercond. Sci. Technol. **35** (2022) 065006.

6. M. Gürsul, Tr. J. Nature Sci. **12** (2023) 44.

7. S. Zhang, C. Li, Q. Hao, J. Feng, T. Lu, P. Zhang, J. Supercond. Nov. Magn. **28** (2015) 1729.

8. W. K. Kwok, U, Welp, A. Glatz, A. E. Koshelev, K. J. Kihlstrom, G. W. Crabtree, Rep. Prog. Phys. **79** (2016) 116501.

9. M. Murakami, N. Sakai, T. Higuchi, S. I. Yoo, Supercond. Sci. Technol. **9** (1996) 1015.

10. P. Mandal, D. Rakshit, T. Sk., A. K. Ghosh, J. Supercond. Nov. Magn. **35** (2022) 1079.

11. D. Rakshit, T. Sk., P. Das, S. Haldar, A. K. Ghosh, Physica C **588** (2021) 1353909.

12. P. Mandal, D. Rakshit, I. Mukherjee, T. Sk., A. K. Ghosh, Phys. Lett. A **436** (2022) 128072.

13. T. Sk., A. K. Ghosh, AIP advances **10** (2020) 065117.

14. T. Sk., A. K. Ghosh, J. Low Temp. Phys. **198** (2020) 224.

15. W. H. Li, C. W. Wang, C. Y. Li, C. K. Hsu, C. C. Yang, C. M. Wu, Phys. Rev. B **77** (2008) 094508.

16. B. Oh, Y. H. Choi, S. H. Moon, H. T. Kim, B. C. Min, Appl. Phys. Lett. **69** (1996) 2288.

17. V. I. Nizhankovskiy, K. Rogacki, Phys. Rev. B **100** (2019) 104510.

18. B. I. Halperin, D. R. Nelson, J. Low Temp. Phys. **36** (1979) 599.

19. H. J. Jensen, P. Minnhagen, Phys. rev. Lett. **66** (1991) 1630.

20. M. A. Dubson, S. T. Herbert, J. J. Calabrese, D. C. Harris, B. R. Patton, J. C. Garland, Phys. Rev. Lett. **60** (1988) 1061.

21. V. L. Berezinskii, Zh. Eksp. Teor. Fiz. **59** (1971) 907 [Sov. Phys. JETP **32** (1971) 493].

22. V. L. Berezinskii, Zh. Eksp. Teor. Fiz. **61** (1971) 1144 [Sov. Phys. JETP **34** (1972) 610].

23. J. M. Kosterlitz, D. J. Thouless, J. Phys. C **6** (1973) 1181.

24. V. Ambegaokar, H. Halperin, D. Nelson, E. Siggia, Phys. Rev. Lett. **40** (1978) 783.

25. V. Ambegaokar, H. Halperin, D. Nelson, E. Siggia, Phys. Rev. B **21** (1980) 1806.

26. P. Das, A. K. Ghosh, Physica C **548** (2018) 27.

27. L. Benfatto, C. Castellani, T. Giamarchi, Phys. Rev. B **80** (2009) 214506.

28. N. Strickland, N. Long, E. Talantsev, P. Hoefakker, J. Xia, M. Rupich, W. Zhang, X. Li, T. Kodenkandath, Y. Huang, Curr. Appl. Phys. **8** (2008) 372.

29. K. Osamura, N. Matsukura, Y. Kusumoto, S. Ochiai, B. Ni, T. Matsushita, Jpn. J. Appl. Phys. **29** (1990) L1621.

30. A. O. Ijaduola, S. H. Wee, A. Goyal, P. M. Martin, J. Li, J. R. Thompson, D. K. Christen, Supercond. Sci. Technol. **25** (2012) 045013.

31. J. Gutiérrez, A. Llordés, J. Gázquez, M. Gibert, N. Romà, S. Ricart, A. Pomar, F. Sandiumenge, N. Mestres, T. Puig, X. Obradors, Nat. Mater. **6** (2007) 367.